Miniaturizing Frequency Domain Near-Infrared Spectroscopy Technology

A dissertation submitted by

Alper Kılıç

in partial fulfillment of the requirements of

Doctor of Philosophy

in

Electrical and Computer Engineering

at

TUFTS UNIVERSITY

February 2026

Adviser: Valencia Joyner Koomson

Miniaturizing Frequency Domain Near-Infrared Spectroscopy Technology

Abstract

> And the Lord spake, saying, First shalt thou take out the Holy Pin.
>
> Cleric, Monty Python and the Holy Grail

FD-NIRS is a powerful technique for noninvasive quantification of tissue optical properties and hemodynamics. It enables the measurement of oxygenation, blood volume, and other physiological parameters with high temporal resolution, providing a valuable tool for neuroscience, critical care, and personalized health monitoring. Traditional FD-NIRS systems rely on bulky benchtop instruments, including signal generators and data acquisition units, which limit portability, clinical accessibility, and the potential for continuous or wearable monitoring. This thesis presents a systematic effort to address these limitations through the progressive miniaturization and integration of FD-NIRS technology, culminating in the design of a next-generation, highly integrated FD-NIRS ASIC. The work builds on the Generation 1 instrument, developed by a previous student, Yun Miao, who provided the initial platform for FD-NIRS measurements based on the Generation FD-NIRS ASIC that he had designed but relied on benchtop hardware for signal generation and readout. Therefore, the instruments described in this thesis begin with Generation 2, each iteration improving hardware integration, portability, and measurement stability while aiming to preserve the quantitative fidelity of laboratory-grade systems.

The Generation 2 instrument eliminated the need for external signal generators by integrating direct digital synthesizer and an improved laser driver on-board. This architecture reduced hardware complexity and enabled a fully self-contained system while achieving performance comparable to commercial ISS Imagent systems, with less than 15 % error in absorption and 20 % in scattering coefficient recovery. Physiological validation during *in-vivo* vascular occlusion experiments demonstrated the instrument's sensitivity to hemodynamic changes, including characteristic dynamics of oxy- and deoxyhemoglobin, confirming its capability for tissue monitoring in a compact format.

The Generation 3 instrument advanced miniaturization further by integrating amplitude and phase measurement functionality via analog demodulation circuits and adopting a Dual-Slope/Self-Calibrating (DS/SC) probe geometry. This approach enabled absolute and calibration-free recovery of optical properties and provided enhanced sensitivity to deeper tissue layers. Solid phantom experiments achieved absorption and scattering errors below 12 % while demonstrating resilience to external perturbations. Despite these improvements, limitations in the analog demodulator stage constrained the signal-to-noise ratio and measurement stability, motivating the development of a fully digital readout scheme in the next generation.

The Generation 4 instrument replaced analog demodulation with deterministic digital sampling using an STM32 microcontroller, ensuring precise measurement timing and improved phase and amplitude recovery. This design achieved phase noise of 0.08° standard deviation and intensity variation of 0.11 % standard deviation over mean across 30 minutes, matching or exceeding commercial systems. Combined with DS/SC analysis, the instrument enabled *in-vivo* measurements on human tissue and confirmed the feasibility of a fully portable FD-NIRS system suitable for research, clinical and field applications. However, the dynamic range of the instrument was insufficient for tracking dramatic changes in tissue oxygenation and this was traced to the FD-NIRS ASIC using the deintegrated instrument explained in the Appendix.

Building on insights from these prototypes, the final stage of this work focused on the design of a next-generation FD-NIRS ASIC, consolidating critical functionalities, including the analog front-end, amplitude and phase detectors, and laser driver, into a single chip. The ASIC was designed and verified with simulation to operate with 147 MHz bandwidth with 8 pF input load, 30 $\mathrm{nA_{rms}}$ input-referred noise, and 41 dB dynamic range, surpassing the noise floor of the photodetector. The phase detector provides 0.02° resolution with 14-bit digital output, while the amplitude detector maintains 1 % nonlinearity across 95 % of the supply range. The laser driver incorporates closed-loop compensation for diode aging and temperature fluctuations for stable optical output. These design features enable the construction of an extremely compact, low-power FD-NIRS system comprising only the ASIC, DDS, microcontroller, and probe optics, establishing a viable pathway toward wearable deployment.

Together, the developments presented in this thesis demonstrate that FD-NIRS technology can be successfully miniaturized without sacrificing quantitative accuracy. The progression from Generation 2 through Generation 4 instruments defines key architectural, electronic, and measurement benchmarks, informing future efforts to realize fully wearable FD-NIRS devices. This work not only advances the technical feasibility of portable FD-NIRS systems but also lays the foundation for broader applications in noninvasive continuous monitoring of tissue physiology, neuroscience research and personalized healthcare.

Acknowledgments

I would like to express my deepest gratitude to

Dr. Valencia Koomson,

for unwavering support and thoughtful mentorship throughout my doctoral studies.

My thesis committee,

Dr. Sergio Fantini, Dr. Khaled ElMaghoub, Dr. Chirag Sthalekar

for their advice and feedback.

My lab mates, Dr. Joel Dungan and Dr. Ravi Durbha,

whose collaboration and camaraderie made the research manageable and meaningful.

My wife, my annoyment center, Dr. Begüm Kabagöz,

whose love, patience and steadfast belief in me carried me through even the most challenging moments of this journey.

My parents and my grandparents,

whose sacrifices, unconditional support and unwavering faith in my abilities laid the foundation upon which all of my achievements rest.

List of Acronyms

ADC analog-to-digital converter.

AFE analog front-end.

APD avalanche photodiode.

ASIC application specific integrated circuit.

BJT bipolar junction transistor.

BTE Boltzmann transfer equation.

CMFB common-mode feedback.

CW-NIRS Continuous Wave Near-Infrared Spectroscopy.

DAC digital-to-analog converter.

DAQ data acquisition card.

DDS direct digital synthesizer.

DE diffusion equation.

DMA direct memory access.

DNL differential non-linearity.

DPF differential path-length factor.

DS dual-slope.

DS/SC Dual-Slope/Self Calibrating.

DSF differential-slope factor.

FD-NIRS Frequency Domain Near-Infrared Spectroscopy.

FFT fast Fourier transform.

FPGA field programmable gate array.

GPIO general-purpose input/output.

GUI graphical user interface.

HbO_2 oxygenated hemoglobin.

HbR deoxygenated hemoglobin.

HBT total hemoglobin.

HS IRB Health Sciences Internal Review Board.

IC integrated circuit.

IF intermediate frequency.

LED light-emitting diode.

LiDAR ligth detectrion and ranging.

LO local oscillator.

MUX multiplexer.

NA numerical aperture.

NI National Instruments.

NIRS Near-Infrared Spectroscopy.

OP-AMP operational amplifier.

OTA operational transconductance amplifier.

PCB printed circuit board.

RF radio frequency.

ROM read-only memory.

SC self-calibrating.

SD single-distance.

SNR signal-to-noise ratio.

SS single-slope.

StO_2 tissue oxygen saturation.

TD-NIRS Time Domain Near-Infrared Spectroscopy.

TEC thermoelectric.

TIA transimpedance amplifier.

TOI tissue oxygenation index.

VCO voltage controlled oscillator.

VNA vector network analyzer.

Contents

List of Figures

List of Tables

Chapter 1

Introduction

> Then, shalt thou count to three, no more, no less.
>
> Cleric, Monty Python and the Holy Grail

1.1 Motivation

Proper regulation of tissue blood flow and oxygenation is a fundamental prerequisite to maintaining normal physiological function, and a wide range of therapeutic and diagnostic approaches aim to monitor or improve it [2, 3]. Consequently, there is a growing demand in both clinical and research settings for reliable and non-invasive methods to quantify oxygenated hemoglobin (HbO_2) and deoxygenated hemoglobin (HbR) concentrations in tissue [4].

Near-Infrared Spectroscopy (NIRS) has emerged as a powerful modality for this purpose. In NIRS, near-infrared light, typically in the 650-900 nm wavelength range, is sent to the tissue at some location and collected back at a known distance from the source. The further the source and detector are spaced, the deeper the light permeates. The mean penetration depth can be of the order of 5-10 mm for a source-detector separation of 30 mm [5]. In this 650-900 nm wavelength range, water absorption is minimal and light is mainly absorbed by oxyhemoglobin and deoxyhemoglobin.

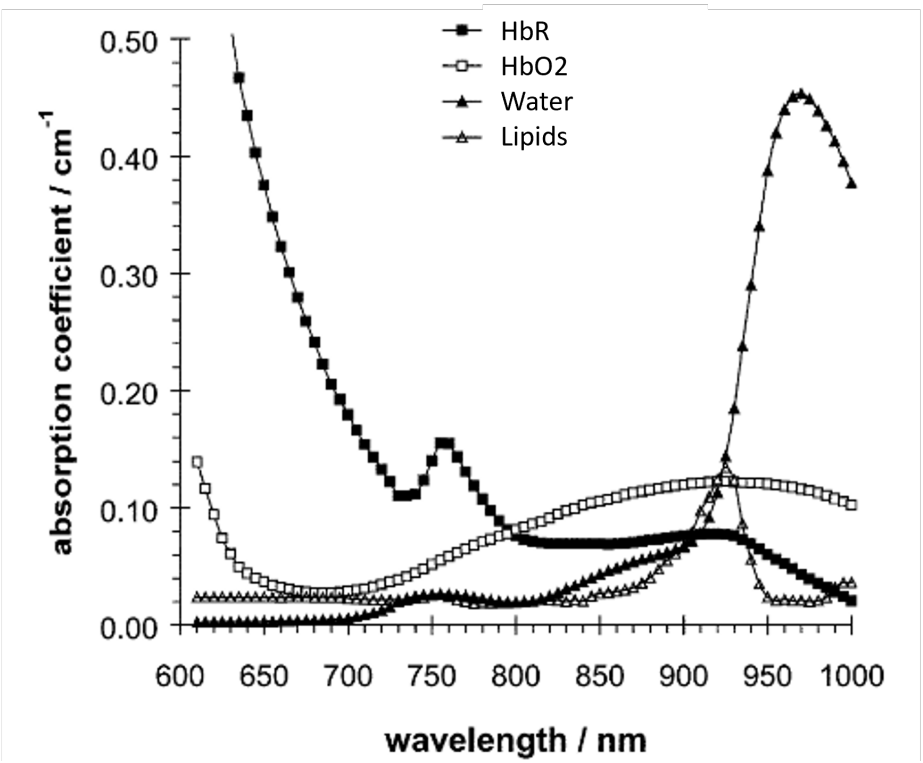

Figure 1-1: The absorption coefficients for water, HbO_2, HbR and lipids in the near-infrared spectrum [1].

For this reason, sometimes this spectrum is also called the "Optical window" or "Therapeutic window".

In this wavelength range, many chromophores, such as water, lipids, melanin, and bilirubin, interact with light, but oxyhemoglobin and deoxyhemoglobin dominate the absorption. The absorption spectra for water, lipids, HbO_2, and HbR in this spectrum can be seen in Figure 1-1. The relationship between incident and detected light, affected by the absorption and scattering properties of tissue, allows the determination of the concentrations of HbO_2 and HbR. This optical approach enables continuous and non-invasive monitoring of tissue oxygenation and hemodynamics. From these absolute values of these chromophores, additional biomarkers such as total hemoglobin (HBT) concentration, tissue oxygenation index (TOI), and a range of other hemoglobin-derived parameters can be calculated directly. The versatility of NIRS has led to its adoption in a wide array of applications. Clinically, it has been used in many areas, such as cancer detection [6–8], wound healing assessment [9], ischemia [10],

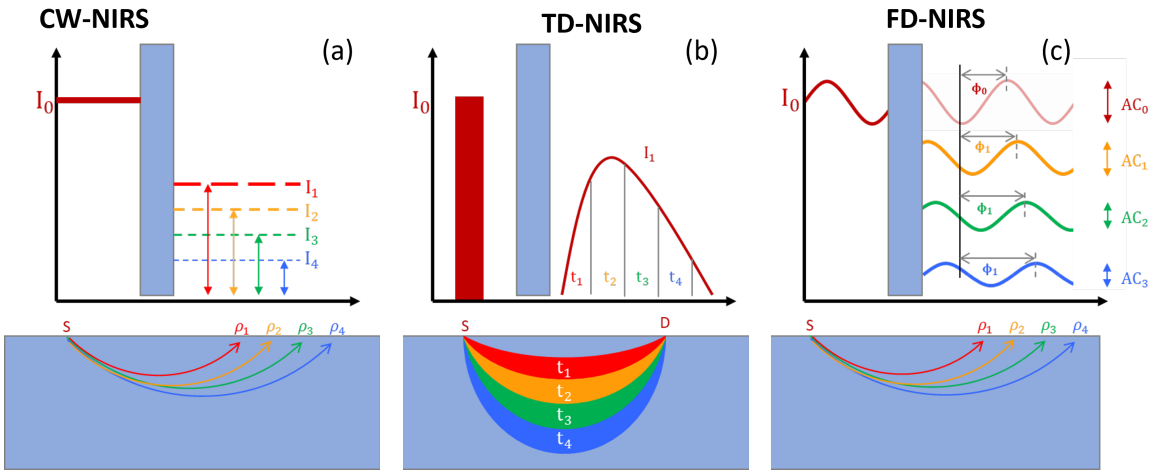

Figure 1-2: Three different popular NIRS modalities. (a): CW-NIRS where the light is not modulated, (b): TD-NIRS where the light is modulated as a very short pulse and (c): FD-NIRS where the light intensity is modulated as a sine wave.

peripheral arterial disease [11], and neonatal diagnosis [12–14]. In neuroscience, it facilitates functional brain studies [15, 16], brain–computer interfaces [17], and the diagnosis of neurological disorders [7]. In addition, the development of compact, low-cost, and portable NIRS instruments has expanded the opportunities for point of care monitoring, enabling a broader implementation in both research and clinical environments.

NIRS can be implemented in three principal modalities: continuous-wave (CW-NIRS) [18], time-domain (TD-NIRS) [19], and frequency-domain (FD-NIRS) [16]. The fundamental distinction among these approaches lies in whether and in what manner the light source is modulated.

CW-NIRS represents the simplest implementation, as the light source is not modulated. In this approach, the tissue is illuminated with a constant intensity beam and the system records temporal variations in the detected intensity. These variations can be analyzed to estimate the relative changes in absorption due to tissue hemodynamics or other physiological processes ($\Delta\mu_a$). However, because the method does not provide independent information about photon scattering, absolute values of the absorption coefficient (μ_a) and the reduced scattering coefficient (μ_s') must be assumed.

TD-NIRS and FD-NIRS overcome this limitation by incorporating light source modulation. In TD-NIRS, the source is pulsed with durations on the order of picoseconds, allowing the measurement of photon time-of-flight distributions. In FD-NIRS, by contrast, the light intensity is sinusoidally modulated at radio frequencies, typically between 50 and 1000 MHz. In both cases, the temporal characteristics of the detected light provide additional information that, when combined with proper calibration, enable the recovery of absolute values of μ_a and μ_s'. For TD-NIRS, these temporal characteristics are expressed in the distribution of the amount of light that reaches the detector at different times, such as t_1 and t_4 in Figure 1-2. But in FD-NIRS, the information is encoded in how much the AC amplitude of recovered light is attenuated (AC_0, AC_1, etc.) and the phase difference between different source-detector separations (ρ_1, ρ_2, etc.). In other words, if the sinusoidally modulated signals can be recovered at various source-detector distances, the μ_a and $\mu_s\prime$ of the tissue can be measured and from these optical properties the absolute HbO_2 and HbR can be computed. As a result, TD-NIRS and FD-NIRS can determine absolute concentrations of HbO_2 and HbR, whereas CW-NIRS can only track relative concentration changes over time under assumed optical properties.

However, the ability to recover absolute chromophore concentrations comes with added system complexity. TD-NIRS generally requires bulky and costly picosecond laser sources, along with high-speed photodetectors capable of resolving ultrashort photon pulses. FD-NIRS, in comparison, has less demanding hardware requirements. Its implementation can be relying on readily available laser diodes and conventional photodetectors, making it a more practical option for many research and clinical applications. Therefore, FD-NIRS provides an advantageous balance between quantitative accuracy and system complexity, establishing it as a particularly suitable modality for the development of compact, cost-effective instruments such as those explored in this thesis.

1.2 Prior Art

Although numerous CW-NIRS systems are commercially available, including those incorporated into wearable devices such as smart watches, the only frequency-domain instruments currently offered on the market are produced by ISS (Urbana-Champaign, USA) [20, 21]. Despite this, a wide range of academic research groups have developed their own FD-NIRS devices. These designs vary considerably in terms of signal acquisition strategies. For example, some rely on commercial vector network analyzer (VNA)s to obtain phase and intensity information [22–25], while others adopt a direct sampling strategy in which high-speed analog-to-digital converter (ADC) interface directly with radio-frequency signals [26–29].

Alternative approaches have also been explored to bypass the challenges of processing high-frequency signals. In the homodyne method, the detected signals are mixed with a local oscillator (LO) operating at the same frequency, and in-phase/quadrature (I-Q) demodulation is subsequently used to extract both phase and intensity information [30–34]. A related strategy is the heterodyne approach [25, 35–42], in which the recovered signals are mixed with an LO operating at a slightly offset frequency. This technique preserves the intensity and phase-shift information, but down-converts the radio-frequency signal to a lower intermediate frequency (IF), where sampling and processing are more easily achieved.

Although all of these methods have been successfully demonstrated, not all are well suited for portable or cost-effective instrumentation. For example, VNAs are bulky benchtop instruments with prohibitive cost, while direct sampling requires high-speed ADCs that consume substantial power and often require field programmable gate array (FPGA) based control, further increasing system complexity and energy demands. More recent integrated solutions have shown greater potential for portable and wearable applications [43–46]. Motivated by these considerations, the work presented here adopts the heterodyne approach within an integrated platform, combining the robustness of frequency-domain techniques with the feasibility of compact, low-power hardware implementation.

The instrument presented in [47] will act as the starting point for the rest of the work presented in this thesis and should be considered as the Generation 1 Instrument, featuring the Generation 1 FD-NIRS ASIC. The Generation 1 Instrument consisted of a 3-stack of printed circuit board (PCB)s of $16 \times 1.15 \times 5$ cm^3 volume, two separate benchtop signal generators with three output channels in total, a custom-made probe, and another benchtop National Instruments (NI) data acquisition card (DAQ). Additionally, this instrument featured a custom-designed Generation 1 FD-NIRS ASIC to interface with the photodetector. The modulation signal was generated by one of the signal generators, then the light sources were modulated with this signal by an on-board laser driver circuit. This amplitude-modulated light was sent to the medium, and then picked up again with the probe. An avalanche photodiode (APD) picked up the light that attenuated and scattered through the medium. Generation 1 FD-NIRS ASIC amplified the photodetector output with its low-noise analog front-end, then did a down-conversion heterodyned with a mixer. Finally, NI DAQ sampled the output of the ASIC. Then, after the experiment was done, the phase and amplitude extraction and the final optical property calculations were performed on a laptop.

1.3 Thesis Organization

Chapter 2 first presents the physical and mathematical background of FD-NIRS, then introduces the two main methods that are used in this thesis. In Chapter 3, the Generation 2 Instrument is described in detail, along with its verification using tissue-mimicking solid phantoms and an *in-vivo* occlusion experiment. This generation also demonstrates the first major integration step, in which the benchtop equipment is replaced and integrated into the instrument.

Chapter 4 introduces the Generation 3 Instrument. This instrument is validated on tissue-mimicking solid phantoms and demonstrates a further step in integration, where channel readout schemes are implemented through demodulator circuits.

Chapter 5 introduces a new readout scheme that improves upon the Generation 3 Instrument and is validated with tissue-mimicking solid phantoms, followed by *in-vivo*

occlusion experiments. The results of these experiments are analyzed using both the multi-distance method and the dual-slope method.

Chapter 6 contains a discussion of the requirements for a new generation of the FD-NIRS ASIC. In addition to the analog front-end, the laser driver and the phase and amplitude readout circuits are integrated. Following this discussion, the design and simulation results of the ASIC are presented. This new, Generation 2 FD-NIRS ASIC can be incorporated into an FD-NIRS instrument design in which the only main functionalities not yet integrated are the signal generation and the microcontroller.

Finally, in Chapter 7, the further development of the ASIC and additional directions for future work are discussed.

Chapter 2

Technical Background

> Four shalt thou not count, nor either count thou two, excepting that thou then proceed to three.
>
> Cleric, Monty Python and the Holy Grail

2.1 Photon Diffusion Theory and Frequency-Domain Near Infrared Spectroscopy

The foundation of the physics behind FD-NIRS lies in the Boltzmann transfer equation (BTE). The propagation of photons through turbid media such as human tissue can be modeled as a transport equation. Defining the number of photons per unit volume per unit solid angle traveling in $\hat{\mathbf{\Omega}}$ direction at position $\mathbf{r}$ and time t as $u(\mathbf{r}, \hat{\mathbf{\Omega}}, t)$, BTE can be written as;

$$\begin{aligned}\frac{\partial u(\mathbf{r}, \hat{\mathbf{\Omega}}, t)}{\partial t} = &-\hat{\mathbf{\Omega}} \cdot \nabla u(\mathbf{r}, \hat{\mathbf{\Omega}}, t) - \nu(\mu_a + \mu_s) u(\mathbf{r}, \hat{\mathbf{\Omega}}, t) \\ &+ \nu\mu_s \int_{4\pi} u(\mathbf{r}, \hat{\mathbf{\Omega}}', t) f(\hat{\mathbf{\Omega}}', \hat{\mathbf{\Omega}})\, d\hat{\mathbf{\Omega}}' + q(\mathbf{r}, \hat{\mathbf{\Omega}}, t),\end{aligned} \tag{2.1}$$

where μ_a is the absorption coefficient, μ_s is the scattering coefficient, ν is the speed of light in the medium, $f(\hat{\mathbf{\Omega}}', \hat{\mathbf{\Omega}})$ is the probability density that the photon travels in

the $\hat{\mathbf{\Omega}}'$ direction and $q(\mathbf{r}, \hat{\mathbf{\Omega}}, t)$ is the light source.

Equation 2.1 is a very generalized form of photons traveling through a turbid medium, and after some algebraic manipulations and certain assumptions the following relationship can be obtained,

$$\frac{\partial U(\mathbf{r}, t)}{\partial t} = D\nabla^2 U(\mathbf{r}, t) - v\mu_a U(\mathbf{r}, t) + S_0(\mathbf{r}, t) \tag{2.2}$$

where $U(\mathbf{r}, t)$ is the photon density, $S_0(\mathbf{r}, t)$ is the light source term, $D = v/[3(\mu_s' + \mu_a)]$ is the diffusion coefficient. The above mentioned assumptions are;

- The medium is highly scattering, such that $\mu_s' \gg \mu_a$. This condition generally holds for biological tissue, where scattering events dominate over absorption.
- The variations in $U(\mathbf{r}, t)$ and $S_0(\mathbf{r}, t)$ occur in a much longer time scale than the average time between collisions. In other words, the temporal variations of the photon density and the source occur on timescales much longer than the average time between scattering events.
- The source is isotropic, i.e. uniform in all directions.

Further details and steps between BTE and diffusion equation (DE) can be found in [48].

In order to examine this equation under the frequency-domain context, one can define the source $S_0(\mathbf{r}, t)$ as;

$$\begin{aligned} S_0(\mathbf{r}, t) &= S_{DC}(\mathbf{r}) + S_{AC}(\mathbf{r}, t) \\ S_{DC}(\mathbf{r}) &= g(\mathbf{r}) P_{DC} \\ S_{AC}(\mathbf{r}, t) &= g(\mathbf{r}) P_{AC}(\omega) e^{-i\omega t} \end{aligned} \tag{2.3}$$

where $g(\mathbf{r})$ is the spatially dependent source factor, P_{DC} is the DC part of the source and $P_{AC}(\omega)$ is the AC part of the source. Solving the diffusion equation, 2.2, with solely the AC part of the source, $S_{AC}(\mathbf{r}, \mathbf{t})$, one can get the following;

$$(\nabla^2 + k^2) U(\mathbf{r}, \omega) = -\frac{g(\mathbf{r}) P_{AC}(\omega)}{D}, \tag{2.4}$$

where $k^2 = (i\omega - \nu\mu_a)/D$. The solution to 2.4 for a point source in an infinite and homogeneous medium is;

$$U(\mathbf{r}, \omega) = \frac{P_{AC}(\omega) e^{ikr}}{4\pi r D} \tag{2.5}$$

where r is the distance from the point source. The amplitude of 2.5 $|U(r, \omega)|$ and phase $\Phi(r, \omega)$ can be written as;

$$\mathrm{AC} = \frac{P_{AC}(\omega)\, e^{-r(\nu\mu_a/2D)^{1/2}}}{4\pi D\, r} \left[\left(1 + \frac{\omega^2}{\nu^2 \mu_a^2} \right)^{1/2} + 1 \right]^{1/2} \tag{2.6}$$

$$\Phi(r, \omega) = r(\nu\mu_a/2D)^{1/2} \left[\left(1 + \frac{\omega^2}{\nu^2 \mu_a^2} \right)^{1/2} - 1 \right]^{1/2} + \Phi_s, \tag{2.7}$$

Looking at Equations 2.6 and 2.7, two variables, r and ω, lend themselves as candidates that can be easily controlled in an experimental setup. This realization gives way to two possible implementation options, namely the multi-distance method where r is varied but ω is kept constant, and the multi-frequency method where ω is varied but r is kept constant. Each method has advantages and disadvantages over the other in terms of implementation. The advantage of the multi-frequency method is that it only needs one detector and one source location. Therefore, debugging implementation issues such as the inherent differences between different optical components or the effects of the coupling between the optics and the medium are easier to deal with. On the other hand, this method requires that the modulation frequency be swept upward of 700 MHz for human tissue [48]. Building an instrument that can perform in such a wide band is quite a difficult task. On the other hand, the multi-distance method does not need the modulation frequency to be swept. However, there is a need for multiple source and detector locations, and as mentioned before, this brings other concerns such as the inherent differences between different optical components or the effects of the coupling between the optics and the medium. In the works presented here, all will be based on the multi-distance approach.

It is apparent from 2.7 that the phase $\Phi(r, \omega)$ has a linear dependency on the distance from the location of the point source, r. On the other hand, the dependency

of AC on r is more complex. However, it can be shown that a related variable exhibits a linear relationship.

$$\ln(rAC) = \ln\left(\frac{P_{AC}(\omega)}{4\pi D}\right) - r\left(\frac{\nu\mu_a}{2D}\right)^{1/2}\left[\left(\left(1+\frac{\omega^2}{\nu^2\mu_a^2}\right)^{1/2}+1\right)^{1/2}\right] \tag{2.8}$$

Thanks to these two linear relationships, an analytical solution to μ_a and $\mu_s\prime$ can be obtained for a highly scattering infinite medium that is illuminated by a point source with sinusoidally modulated intensity in the forms of

$$\mu_a = \frac{\omega}{2\nu}\left(\frac{S_\phi}{S_{ac}} - \frac{S_{ac}}{S_\phi}\right) \tag{2.9}$$

$$\mu_s' = \frac{S_{ac}^2 - S_\phi^2}{3\mu_a} - \mu_a \tag{2.10}$$

where $S\phi$ is the slope of 2.7 and S_{AC} is the slope of 2.8. Equations 2.9 and 2.10 are derived for infinite medium, however, they can still be used to a first degree approximation, for semi-infinite medium, such as human tissue, if the AC slope S_{AC} is computed from the quantity $ln(r^2AC)$. One advantage of deriving a relationship between μ_a and $\mu_s\prime$ and the slopes of $ln(r^2AC)$ and Φ instead of their absolute values such as 2.6 and 2.7 is that the absolute values of these quantities lose importance, but only how these values change between different source detector separations becomes valuable. Figure 2-1 illustrates this point, where panel (a) shows two phase measurements with some offset between them but equal slopes. Panel (b) shows a similar example for the amplitudes. This allows for adjustment of the absolute quantities of AC and Φ if needed to improve instrument performance. For example, a higher AC for possibly better signals, or phases around specific numbers where the phase detector scheme might work better.

Having developed a way to measure the optical properties of semi-infinite media with FD-NIRS, extraction of absolute quantities of HbO_2 and HbR can be performed

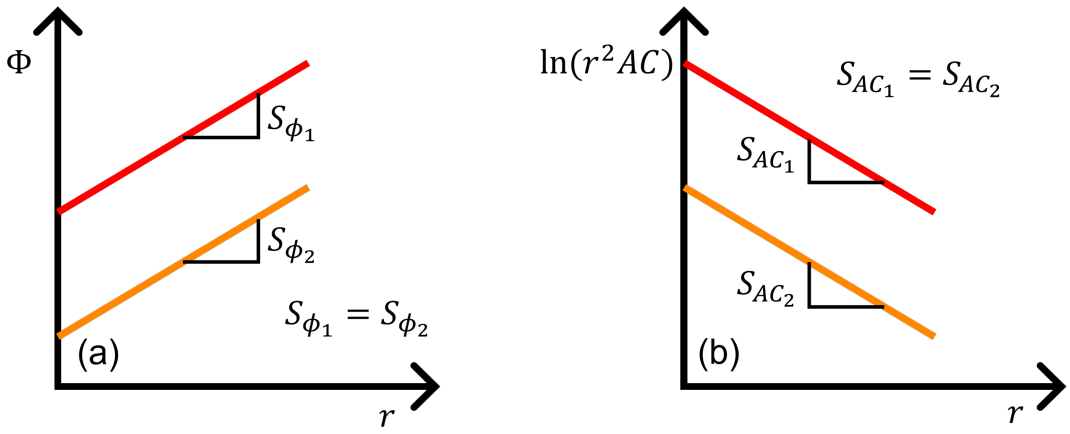

Figure 2-1: Example of why only the slopes are of importance and not the absolute values

by the following equations [20],

$$C_{HbO_2} = \frac{\mu_a^{\lambda_1}\varepsilon_{HbR}^{\lambda_2} - \mu_a^{\lambda_2}\varepsilon_{HbR}^{\lambda_1}}{\varepsilon_{HbR}^{\lambda_2}\varepsilon_{HbO_2}^{\lambda_1} - \varepsilon_{HbR}^{\lambda_1}\varepsilon_{HbO_2}^{\lambda_2}} \tag{2.11}$$

$$C_{HbR} = \frac{\mu_a^{\lambda_2}\varepsilon_{HbO_2}^{\lambda_1} - \mu_a^{\lambda_1}\varepsilon_{HbO_2}^{\lambda_2}}{\varepsilon_{HbO_2}^{\lambda_1}\varepsilon_{HbR}^{\lambda_2} - \varepsilon_{HbO_2}^{\lambda_2}\varepsilon_{HbR}^{\lambda_1}} \tag{2.12}$$

where ε are the extinction coefficients of HbO_2 and HbR at wavelengths λ_1 and λ_2. A very extensive and tabulated list of these extinction coefficients between 250 nm and 1000 nm can be found in [49].

Although the work presented in this thesis will be based on Equations 2.9 and 2.10, for the sake of completeness, it should be mentioned that the optical properties of the medium can also be computed using other combinations of data that FD-NIRS can provide [50]. Using S_{DC} and S_Φ;

$$\begin{aligned} \mu_a &= -\frac{\omega}{2v}\frac{S_{dc}}{S_\phi}\left(\frac{S_\phi^2}{S_{dc}^2} + 1\right)^{-\frac{1}{2}} \\ \mu_s' &= \frac{S_{dc}^2}{3\mu_a} - \mu_a \end{aligned} \tag{2.13}$$

and using S_{DC} and S_{AC};

$$\mu_a = \frac{\omega}{2v}\frac{s_{dc}}{s_{ac}}\left(\frac{s_{ac}^2}{s_{dc}^2} - 1\right)^{-\frac{1}{2}}$$
$$\mu_s' = \frac{S_{dc}^2}{3\mu_a} - \mu_a \tag{2.14}$$

Building upon the theoretical foundation of FD-NIRS presented above, the methodologies used to apply it in this work will be introduced next. The two general approaches were: the multi-distance and the self-calibrating method. Another approach, the Dual-Slope method, will also be introduced, but its application will be limited. The principles of these methods, together with the probe geometries implemented for each, are described in the following sections.

2.2 The Multi-Distance method

In the multi-distance method, the light is sent into the medium at some and then collected back by photodetectors at certain distances. There is no functional difference between sending light to multiple locations and then collecting at a single site versus sending the light at a single location but collecting at several locations. However, in the works in this document that use this method, the former idea is always used since every photodetector requires a separate read-out module, while the light sources can share the same circuitry.

The main requirements for the probe in a multi-distance FD-NIRS measurement are: (1) flexibility for good coupling with the medium, (2) several windows that allow NIR light to become incident to the tissue at known distances from the detector window, and (3) large fiber numerical aperture (NA) and diameter to accommodate large area APDs. To that end, a custom probe from ISS (Champaign, IL) was used. It has a total of 5 windows; 4 emitter windows, each accommodating two fibers (400 µm in diameter), and one detector window. For the detector window, a 2 mm fiber bundle with 0.55 NA is used. The large surface area of the fiber bundle and the high NA make it very suitable to collect low-level diffusive light in the media. As a result, the fiber can be directly connected to the APD without the use of additional expensive

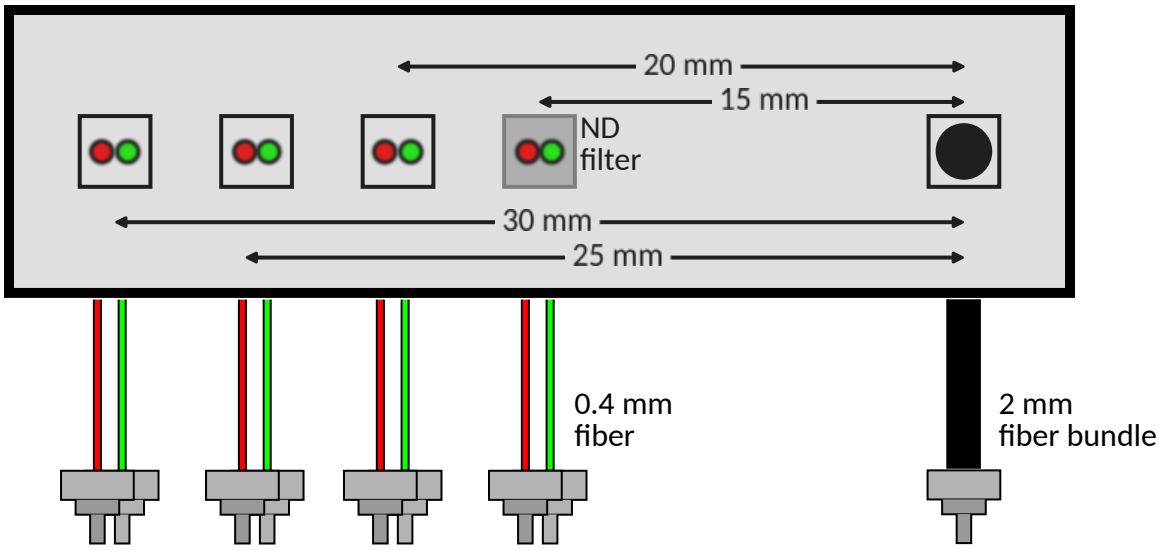

Figure 2-2: Sketch of the multi-distance probe geometry

optics. The head of the probe is made of polyurethane so that it can conform to curved surfaces. The source-detector separations on the probe are 1.5 cm, 2.0 cm, 2.5 cm and 3.0 cm. The sketch of the probe can be seen in Figure 2-2. All fibers have an SMA connector at the other end to support a solid connection between the probe and the PCBs. The available optical power at different source-detector separations varies significantly in multi-distance measurements. A high-gain photodetector can boost signal-to-noise ratio (SNR) at large source-detector separations but also may lead to saturation at small source-detector separations. Although the readout module that interfaces with the optics may have a high dynamic range, tuning the optical power can be a tricky and challenging task in many cases. To solve this challenge, a thin-film neutral density filter is placed on the surface of the first emitter window as an equalizer. The filter attenuates the optical power at 1.5 cm source-detector separation, which expands the overall dynamic range.

2.3 The Self-Calibrating method

As mentioned in Chapter 1, in FD-NIRS, the estimation of absolute optical properties, namely μ_a and μ_s', can be obtained by multi-distance [50], multi-frequency measurements [25], or even single-distance and single-frequency measurements [51],

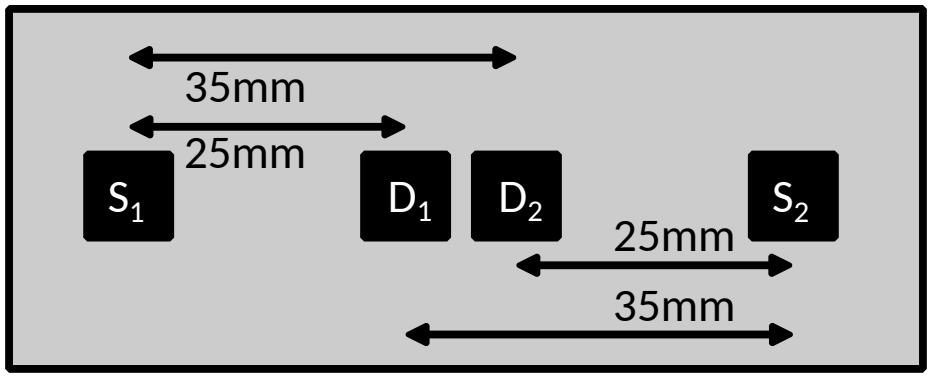

Figure 2-3: Sketch of the Dual Slope / Self-Calibrating Probe geometry

after proper calibration. Typically, these strategies require previous calibration on a phantom with known optical properties. At least two shortcomings of this phantom calibration approach can be mentioned:

- One must assume that the coupling between each optode and the medium remains unchanged between calibration and measurement on an unknown medium.
- One must also assume that the laser's output power and/or the detector's gain do not change between calibration and measurement.

These prerequisites are difficult to satisfy, especially during *in-vivo* measurements. A more robust approach that can be adopted is the Self-Calibrating method [52]. This method uses a probe with two sources (S_1 and S_2) and two detectors (D_1 and D_2), see Figure 2-3.

Many optode configurations are possible [53], but all of them must satisfy one fundamental property, that the closest detector to S_1 (i.e., D_1) is also the farthest detector from S_2, and vise versa: the farthest detector from S_1 (i.e., D_2) is the closest detector to S_2 [53]. Also, it must be verified that:

$$\overline{S_1D_2} - \overline{S_1D_1} = \overline{S_2D_1} - \overline{S_2D_2} = \Delta r \tag{2.15}$$

where Δr is the difference between long and short distances. The method relies on measurements of both ϕ and AC data types for all possible combinations of source-detector pairs (i.e., four single-distance (SD) measurements per each data type). A

single-slope (SS) measurement is identified by one source and two detectors (e.g. $S_1D_1D_2$), and it is defined by:

$$SS = \frac{\Delta Y}{\Delta r} = \frac{Y(r_2) - Y(r_1)}{\Delta r} \tag{2.16}$$

where Y is either ϕ or logarithmic AC, $\ln[r^2 AC]$, where r is the distance between the source and the detector, and the distances between the source and the detector r_1 and r_2 are defined as:

$$\begin{aligned} r_1 &= \overline{S_1D_1} \\ r_2 &= \overline{S_1D_2} \end{aligned} \tag{2.17}$$

In other words, an SS measurement is defined by using two SD measurements relative to the same source. If the data AC and ϕ were calibrated, an SS measurement of both data types would be enough to measure the optical properties [50, 54, 55]. This is impossible without calibration, because the optodes coupling to the medium and the gains of the detectors are unknown. However, when both SS measurements are averaged ($(SS_1 + SS_2)/2$), all unknowns related to source emission, detector sensitivity, and probe-medium coupling are canceled, and the true slope (due only to the optical properties of the medium) is obtained [52, 56]. Therefore, the SC method uses both SS measurements obtained with the source-detector combinations $S_1D_1D_2$ and $S_2D_2D_1$, and calculates the average of the two SS slopes. The retrieval of optical properties is obtained iteratively [55]. Once these methods recover absolute μ_a, absolute [HbO_2] and [HbR] are calculated with equations 2.11 and 2.12.

2.4 The Dual-Slope method

The absolute optical properties measured with the SC method involve AC and ϕ data types in combination. These two data types individually have different depth-sensitivities to $\Delta\mu_a$ [57]. Therefore, using the SC method to measure these changes would mix information from different depths. A straightforward depth-selective method to measure $\Delta\mu_a$ relies on only one data type (AC or ϕ). For SD data, AC data will

be more sensitive to changes occurring through superficial tissue, while ϕ data will be preferentially sensitive to deeper tissue (in the case of a semi-infinite homogeneous medium). The $\Delta\mu_a$'s can be measured with a single data type and with either SD or SS data by generalizing the concept of the differential path-length factor (DPF) for SD to the differential-slope factor (DSF) for SS [58]. By averaging the changes of two SSs, we obtain the dual-slope (DS) method [59], which allows one to eliminate most instrumental confounding factors, with the same reasoning as the self-calibrating (SC) method above. Change in absorption coefficient, $\Delta\mu_a$, can be computed using changes in DS data by using the following;

$$\Delta\mu_{a,Y} = \frac{-[\Delta SS_{Y1} + \Delta SS_{Y2}]}{\langle L_2\rangle_{Y1} - \langle L_1\rangle_{Y1} + \langle L_2\rangle_{Y2} - \langle L_1\rangle_{Y2}} \tag{2.18}$$

where $\Delta SS_{Y,i}$ is the change of slope i (where, $i \in [1, 2]$) and $\langle L_j\rangle_{Yi}$ is the generalized path-length at the distance j (where, $j \in [1, 2]$ for the short and long source-detector separation, respectively) of the slope i [58]. The $\Delta\mu_a$ may be recovered with either DS intensity (DS_{AC}) or DS phase (DS_{ϕ}) data; regardless, similar to above, $\Delta\mu_a$ is finally converted to $\Delta[\mathrm{HbO}_2]$ and $\Delta[\mathrm{HbR}]$ using Beer's law and known extinction coefficients [49].

Chapter 3

Generation 2 Instrument: Integrated signal generation

> Five is right out.
>
> Cleric, Monty Python and the Holy Grail

In Section 1.2, it was established that the works presented in this thesis are iterative and build on each other. In this respect, the starting point for these efforts was the Generation 1 Instrument that was introduced in Section 1.2. Simply put, this instrument consisted of the FD-NIRS ASIC, a PCB stack, a probe, two benchtop signal generators, and a separate benchtop data acquisition system. In this chapter, the Generation 2 Instrument will be presented. This instrument is the first step towards the goal of miniaturizing an FD-NIRS instrument.

The major improvement in this generation is the elimination of the two tabletop signal generators by integrating them into the instrument. In addition to this major step, the on-board laser driver circuit was also improved with a modified architecture. In Section 3.1, the system architecture of the Generation 2 Instrument will be laid out, in Section 3.2 the calibration method for this instrument will be explained with examples, and then in Sections 3.3 and 3.4 results with tissue mimicking solid phantoms and *in-vivo* occlusion experiments will be presented, respectively.

3.1 System Architecture

For an FD-NIRS instrument, whether it uses the heterodyned down-conversion technique or not, there are certain electronic or optical "functions" that need to be realized. An exhaustive list of these functions would depend on the exact implementation of the instrument. However, since the works described in this thesis are iterative and build on top of each other, most of the functions and solutions applied are common. The optical, mechanical and electronic components described in this section will be used not only in the instrument described in this chapter, but also in other instrument generations unless stated otherwise. The block diagram of the Generation 2 Instrument can be seen in Figure 3-1, and the actual top view of the instrument can be seen in Figure 3-2. The light sources in this instrument are laser diodes that emit at 690 nm and

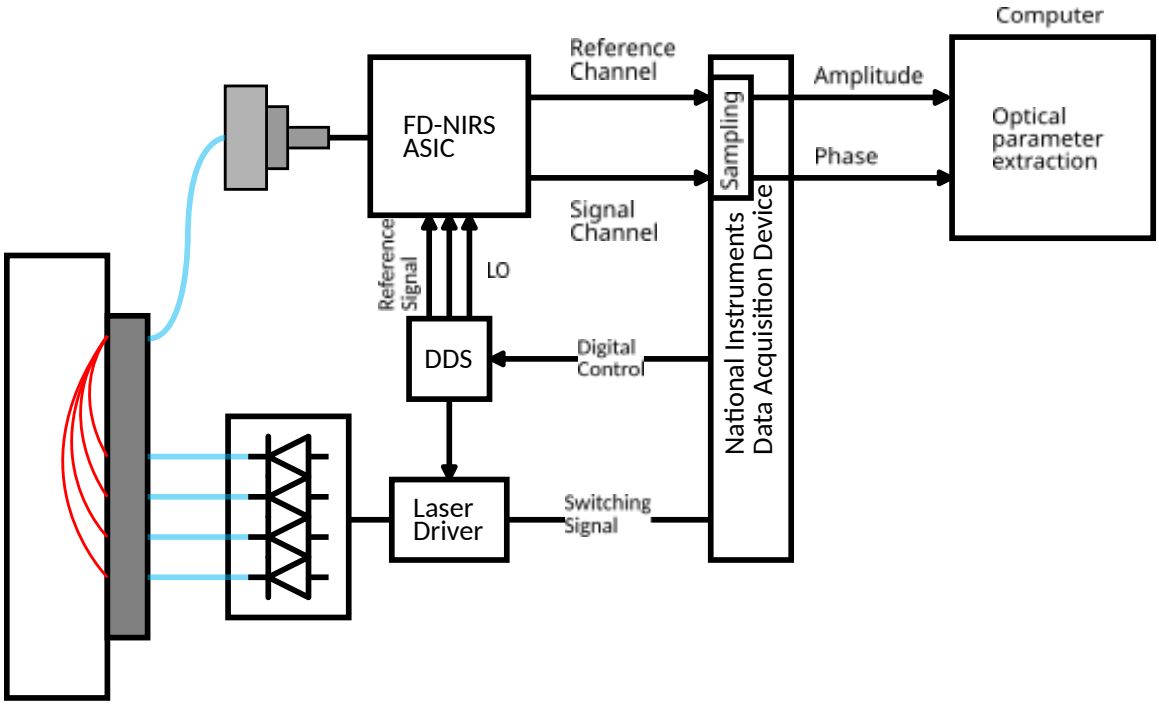

Figure 3-1: Block diagram of Generation 2 Instrument

830 nm. These laser diodes are "time-division multiplexed", in other words, turned on and off for 120 ms by the NI DAQ. The laser diodes are coupled to the probe with a fiber bundle with 400 µm fibers. Since this is an FD-NIRS instrument, the intensity of the near-infrared light sources needs to be modulated at a radio frequency (RF),

and this modulation is done by two laser driver circuits, one laser driver for each wavelength 690 nm and 830 nm. The modulation frequency in this instrument was chosen as 80 MHz. Intensity-modulated near-infrared light, delivered to the medium with the fiber, is attenuated and scattered through the medium, and then picked up by the collection fiber (2 mm diameter, 0.55 NA) and relayed to an APD. The details of the probe (delivery and collection fibers) itself were explained in detail in Section 2.2. The electrical signal recovered by the photodetector is amplified, processed and down-converted in the FD-NIRS ASIC [60]. The entire signal chain inside the FD-NIRS ASIC is fully differential for optimal common-mode suppression and noise performance. In addition to the signal that was used by the laser driver circuits to

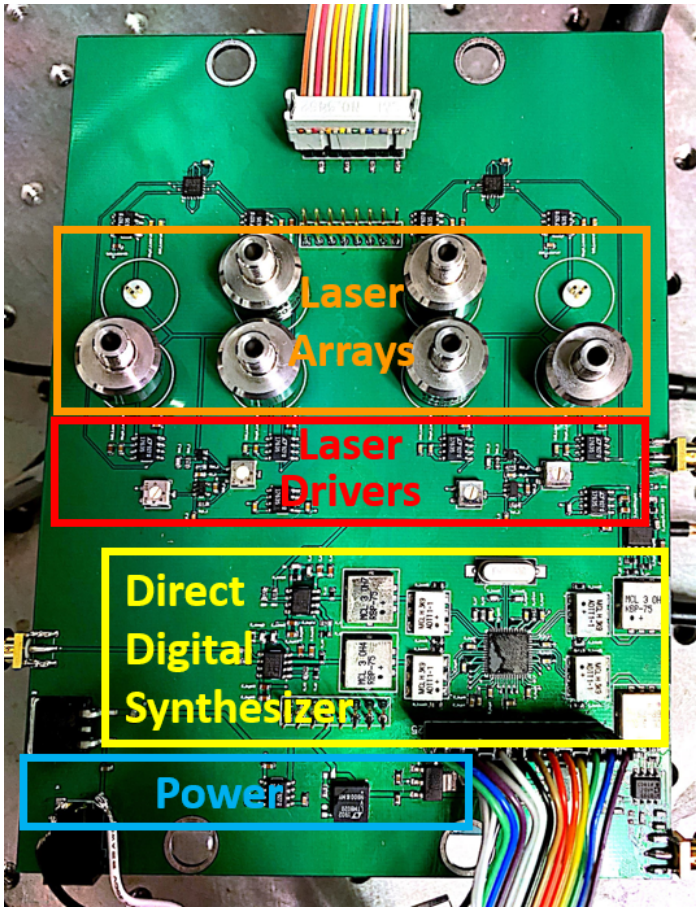

Figure 3-2: Top view of the Generation 2 Instrument

modulate the intensity of the near-infrared sources, three additional signals are needed. The first is a reference signal so that the phase shift of the modulated light can be

measured with respect to it. The other two are the differential LO signals that are needed for heterodyned down-conversion inside the FD-NIRS ASIC. To that end, a reference signal at the same frequency as the laser modulation frequency (80 MHz) and two differential LO signals that are at a frequency that is slightly different from the modulation frequency (80.0001 MHz) are generated using the on-board direct digital synthesizer (DDS). Heterodyned down-conversion conserves the amplitude and phase information that the FD-NIRS method aims to sense but carries this information to a much lower frequency, where extraction can be done much easier. The down-conversion results in output signals at 100 Hz, which are digitized by the DAQ with a sampling rate of 400 kSps and further processed in software to extract the optical properties, μ_a, $\mu_s\prime$, and finally the concentrations of HbO_2 & HbR.

In the next Section, many of these electronic and optical components will be explained in detail.

3.1.1 Optics

3.1.1.1 Laser Diodes

Simple laser diodes were chosen as light sources, since these laser drivers do not depend on very complex laser driver circuits, and they can be treated as regular light-emitting diode (LED)s from an electronics point of view. These laser diodes are HL670MG [61] which lases at 690 nm and HL8338MG [62] at 830 nm. These laser diodes come in a 5.6 mm TO can with a C-type pin configuration. The laser diodes are mounted onto the PCBs via TO can laser diode mounts (Thorlabs S05LM56), and the fibers are coupled to the laser diodes via SMA fiber adapters (Thorlabs PM20-SMA). Mounts and adapters provide robust contact and also serve as heat sinks. These laser diodes come with an integrated photodetector inside them that produces a current that is proportional to the optical output power of the laser diode. This current is called the Monitoring Current. Under typical operating conditions, the forward current that biases the laser diode and generates the light is ~ 70 mA, and the monitoring current is ~ 150 µA.

3.1.1.2 Photodetector

The photodetectors used in these instruments are S9251-15 APDs from Hamamatsu. Although photomultiplier tubes generally offer higher photosensitivity with lower noise levels than APDs, they operate under several kilovolt bias conditions, making them unsuitable for wearable or portable instruments. The important specifications of this APD are that the spectral response ranges between 400 nm and 900 nm, peaks at 860 nm, photosensitivity of $0.52\,\mathrm{A\,W^{-1}}$, with an avalanche gain of 100, the breakdown voltage is $-250\,\mathrm{V}$ and the $-3\,\mathrm{dB}$ bandwidth is 350 MHz [63]. These great performance metrics of this APD come with trade-offs, in the shape of 3.6 pF junction capacitance and 0.8 nA dark current. This APD was powered by a TR-0.2N from Matsusada Precision. This high voltage power supply works under 5 V and offers an adjustable output voltage, with less than $10\,\mathrm{mV_{pp}}$ ripple [64].

3.1.2 Electronics

3.1.2.1 FD-NIRS ASIC

The FD-NIRS ASIC is a custom-designed integrated circuit, fabricated in IBM 130 nm CMOS process [60].

The ASIC block diagram can be seen in Figure 3-3. It has two fully differential identical channels that consist of a low-noise resistive feedback transimpedance amplifier (TIA), a Gm-C bandpass filter, and a double balanced Gilbert mixer. One channel processes the signal from the APD and the other channel processes the reference signal generated by a signal generator. The very weak photoelectric current from the APD is amplified by $\sim$100 dB by the front-end TIA. The Gm-C bandpass filter further amplifies the signal by additional $\sim$20 dB and also filters noise signals that may have been coupled to the RF signal. The double balanced Gilbert mixer down-converts the RF signal to an intermediate frequency (IF) with the help of the LO signals, generated by a signal generator.

Since most of the APDs in the wavelength of interest with enough bandwidth for FD-NIRS applications that are commercially available are single-ended products, a

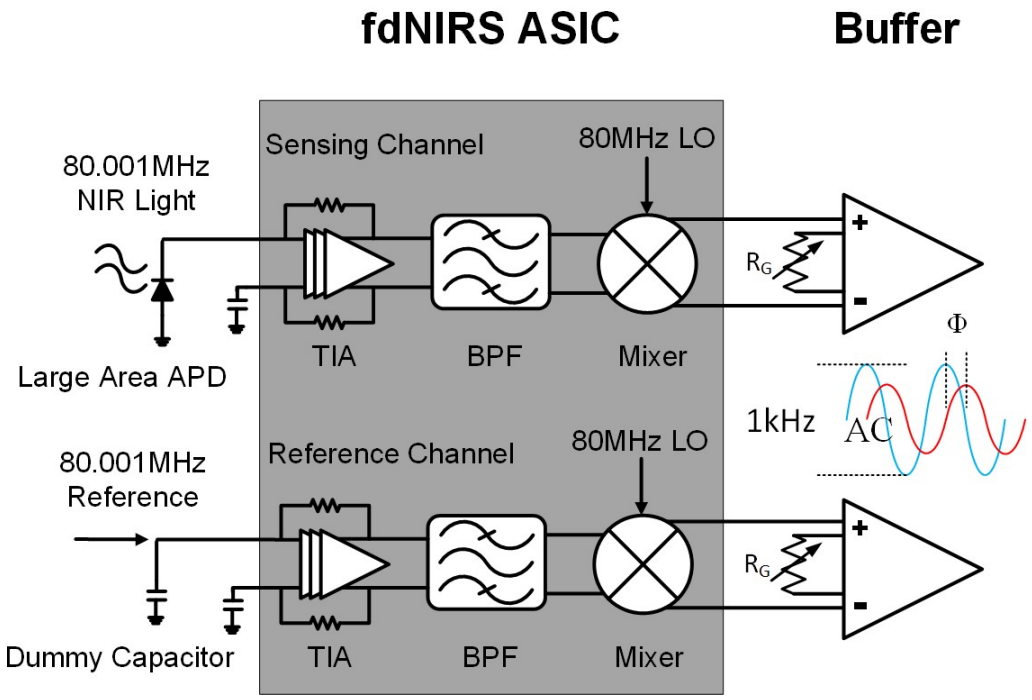

Figure 3-3: Block diagram of Generation 1 FD-NIRS ASIC.

dummy capacitor with the same capacitance as that of the APD junction is connected to the input of Channel 2. Equalization of the capacitances seen by both inputs improves noise performance and linearity of the FD-NIRS ASIC. The two differential output pairs of the FD-NIRS ASIC are converted to single-ended, buffered, and further amplified off-chip. An instrumentation amplifier is used for this purpose, since instrumentation amplifiers, by design, convert differential signals to single-ended signals with controllable gain and controllable DC common mode, so that the output can be sampled by analog-to-digital converters.

3.1.2.2 Laser Driver

Custom laser driver circuits were designed to drive the above-mentioned laser diodes. The schematic of the laser driver circuits can be seen in Figure 3-4. The basic topology of the driver is a modified constant-current regulator with a feedback loop that sets the DC voltage at the output of an operational amplifier (OP-AMP), using the monitoring current of the integrated photo diodes of the laser diodes. The conventional constant-current regulator circuit ensures the forward current of the laser diode constant.

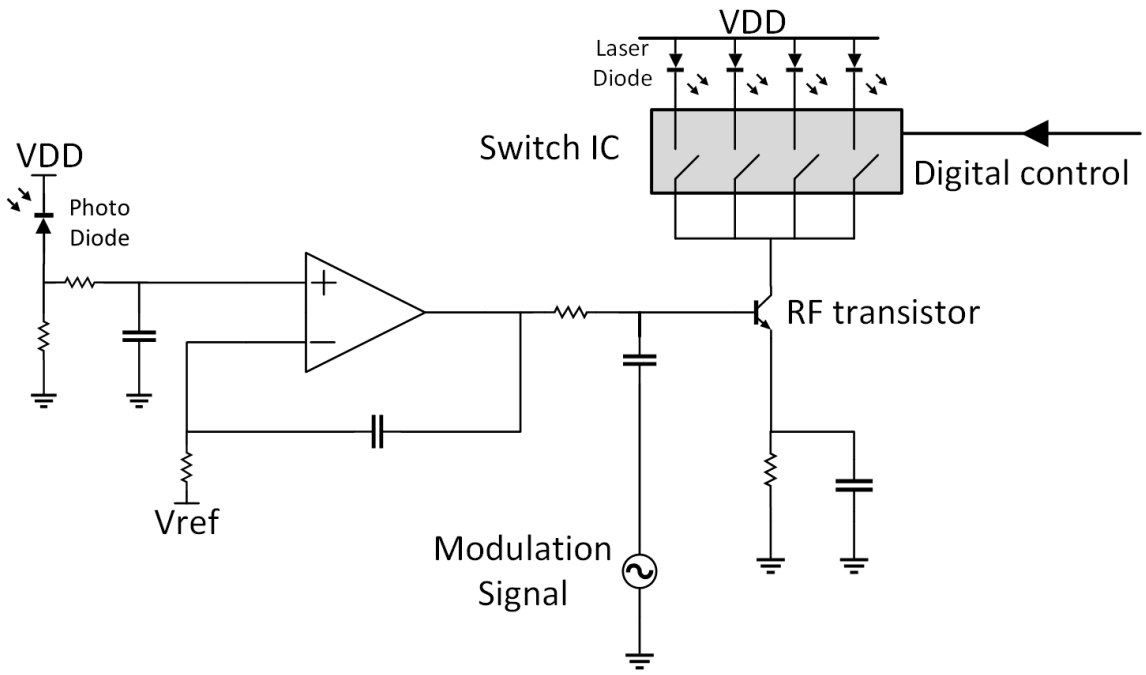

Figure 3-4: Schematic of the laser driver circuit

Instead of keeping the forward current constant, this approach works to keep the feedback current constant across temperature, aging, etc.; hence, even if the quantum efficiency of the laser diode changes, the optical output can stay constant by adjusting the forward current. For example, if a laser diode has a lower optical output power than the others with the same forward current, in other words, lower monitoring current than expected, the feedback loop increases the forward current, which increases the optical power, which in turn increases the monitoring current of that laser diode, and the loop settles.

The DC reference voltage V_{ref} sets the operating DC voltage at the output of the OP-AMP and the coupling capacitor C_c couples the RF modulation signal on top of the DC voltage. The output of the OP-AMP biases the bipolar junction transistor (BJT) and results in an emitter current with DC and AC components. The AC component of the current can be adjusted independently from the DC component by adjusting the amplitude of the modulation signal. An important detail here is that laser diodes at different wavelengths produce a different monitoring current with the same optical power. Therefore, the laser driver circuit should be slightly modified with

different laser diodes. This modification can be performed by changing V_{ref} or R_{fb}. OP-AMP was chosen as OPA695 [65] due to its very high bandwidth (600 MHz for gain = + 1) and unity gain stability. The BJT is chosen as BFP780 [66] for its linearity (23 dB output 1-dB compression point), maximum current capability (>100 mA). The switching integrated circuit (IC) is ADG1412 [67], chosen for its low channel resistance (1.5 Ω) and current capability (> 200 mA).

3.1.2.3 Signal Generation

For the multi-distance FD-NIRS instruments presented here, a total of 4 RF signals need to be generated; one for laser modulation (e.g. 80.0001 MHz), one as reference signal (e.g. 80.0001 MHz) and two as the differential LO signals (e.g. 80 MHz) for the down-conversion. Solutions such as crystal oscillators are not suitable because two RF tones that are very close to each other need to be generated, and an active feedback mechanism is needed to keep the separation between the tones. Therefore, a DDS (AD9959 [68]) is used for its four differential output channels that are frequency, amplitude, and phase independent of each other. This DDS offers 0.12 Hz frequency resolution, and 14-bit phase resolution, along with exceptional phase noise performance of −110 dBc/Hz at 1 kHz offset from carrier frequency of 75.1 MHz and −87 dBc spurious free dynamic range of ±10 kHz offset from 75.1 MHz carrier. The outputs of this DDS are differential ended and one ADTT1-1+ [69] balun is used in every output to convert from differential to single ended. The outputs are then filtered by a band-pass filter.

3.2 Calibration

The top view of the instrument can be seen in Figure 3-2. There are two laser arrays consisting of four laser diodes each, driven by a laser driver circuit. Even though the laser diodes and the laser driver circuits for the two different colors (690 nm and 830 nm) are identical to each other, there is always some mismatch due to manufacturing, layout, aging, etc., but most importantly the different coupling efficiencies of each to

the tissue. To compensate for these effects, we have developed a simple algorithm for calibrating the instrument using a "Calibration" phantom. The μ_a and $\mu_s\prime$ of this phantom is obtained with the gold standard ISS FD-NIRS instrument. When the optical properties are known, using Equations 2.9 and 2.10, we can compute the correct slopes, S_{ac} and S_ϕ, of this Calibration phantom. Then a measurement is taken from this phantom as if its optical properties are unknown, and using the correct slopes, calibration factors are created for each laser diode to compensate for the mismatch as;

$$\begin{aligned} AC_{calib} &= AC_{measured}/AC_{expected} \\ \phi_{calib} &= \phi_{measured} - \phi_{expected} \end{aligned} \tag{3.1}$$

where $AC_{measured}$ is the measured AC magnitude, and $\phi_{measured}$ is the phase shift measured from a laser diode. Similarly, the $AC_{expected}$ is the expected AC amplitude and $\phi_{expected}$ is the expected phase shift for the same laser diode, calculated by the correct slopes computed from the known μ_a and $\mu_s\prime$. This approach creates a lookup table that is used to correct for component and coupling-based mismatches.

Figure 3-5 shows an example of the calibration algorithm, where the red crosses are the measurement results before the calibration, and the blue stars are after the calibration. The black dashed lines indicate the values of S_{AC} and S_ϕ derived from the known values μ_a and $\mu_s\prime$ of the Calibration phantom, and the green dashed lines are the line fit to the calibrated results. One important note here is; subplots (a) and (c) of Figure 3-5 show the "linearized amplitudes". This linearization process allows us to realize our goal of measuring S_{AC} of the medium, which can be approximated as the slope of $ln(\rho^2 * AC)$ for reflectance measurements in semi-infinite media, where ρ is the source-detector separation [70], and AC is the amplitude of the measured AC signal.

It can be seen that, after calibration, the recovered S_{AC} and S_ϕ (green dashed lines) are very close to the known optical values (black dashed lines). The tabulated results for the calculated μ_a and $\mu_s\prime$ for two additional phantom using this calibration algorithm can be found in Table 3.1.

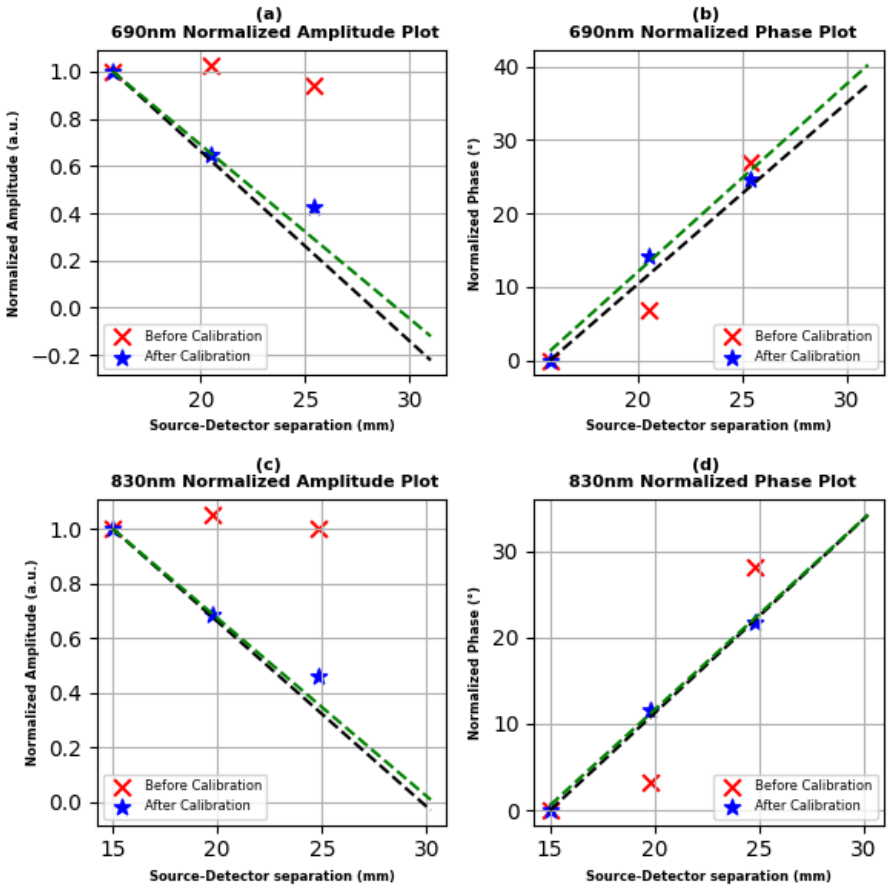

Figure 3-5: An example of the calibration algorithm. (a) & (c) Linearized and normalized amplitudes for 690 nm and 830 nm lasers respectively. (b) & (d) Normalized phases for 690 nm and 830 nm lasers respectively.

Table 3.1: Solid phantom measurement results using a calibration phantom

Phantom	**Parameters**	**Expected** (mm^{-1})	**Measured** (mm^{-1})	**Error**
Calibration Phantom	μ_a 690nm	0.0081	-	-
	μ_s' 690nm	0.761	-	-
	μ_a 830nm	0.0077	-	-
	μ_s' 830nm	0.597	-	-
Phantom1	μ_a 690nm	0.0015	0.0014	-6.67%
	μ_s' 690nm	1.023	0.880	-13.9%
	μ_a 830nm	0.0013	0.00114	-12.3%
	μ_s' 830nm	0.785	0.764	-2.66%
Phantom2	μ_a 690nm	0.0124	0.0142	+14.5%
	μ_s' 690nm	0.930	0.904	-2.79%
	μ_a 830nm	0.0106	0.0098	-7.54%
	μ_s' 830nm	0.763	0.801	+4.98%

3.3 Accuracy and Stability

Absolute accuracy is affected by both systematic errors and instrumental noise. Systematic errors such as the validity of the semi-infinite medium assumption, uneven light coupling, and variation in probe fabrication can be minimized by applying more sophisticated calibration and correction methods [20].

3.3.1 Accuracy

To characterize the accuracy of FD-NIRS instruments, measurements are usually conducted on solid and/or liquid phantoms with known optical parameters. Liquid phantom experiments were reported for a previous iteration of the instrument, which featured the same ASIC but consisted of mostly of benchtop equipment [60]. In this section, the solid phantom experiments are presented, with one phantom used for calibration and two others used for the accuracy and stability measurements.

All three phantoms were fabricated by the Diffuse Optical Imaging of Tissue Lab at Tufts University and their optical properties were characterized by a commercial oximeter instrument (ISS Model 96208) using a multi-distance approach. These characterization results were taken as the ground truth and reported in the column "Expected (mm^{-1})" in Table 3.1. The calibration phantom provides baseline results. The measured data and error results for phantoms 1 and 2 are reported in Table 3.1.

During measurements, the probe was placed on the surface of the solid phantoms. Each laser diode was turned on for 120 ms. Ten readouts of each phantom are averaged, and the results are listed in Table 3.1. The maximum error is less than 15 % in all measurements. The accuracy of this instrument and the previously reported FD-NIRS systems is compared in Table 3.2 [20, 25, 27, 29, 71, 72].

Table 3.2: Accuracy comparison

	Fantini [20]	Pham [25]	No [71]	Sthalekar [72]	Torjesen [27]	Stillwell [29]	**This Work**
Sensor	PMT	APD Module	APD Module	APD	APD	APD	**APD**
Sensing method	Multi-distance	Multi-frequency	Multi-frequency	Multi-distance	Multi-frequency	Multi-frequency	**Multi-distance**
Frequency (MHz)	120	10–1000	10–1000	100	50–400	1–400	**80**
Light Coupling	3 mm fiber bundle	1 mm fiber	Direct coupling	1 mm fiber & objective lens	6×400 µm fiber bundle	6×400 µm fiber bundle	**2 mm fiber bundle**
Maximum Error	15%	5%	14.48%	27.13%	5%	10%	**15%**
Dimensions	N/R	N/R	N/R	N/R	10×12×16 in	12×12×3 in	**12×11.5×5 cm**
Portable	No	No	No	No	Yes	Yes	**Yes**

3.3.2 Stability

In order to characterize the stability of this measurement, a 15 minute-long solid phantom measurement is performed. The ratios of the measured AC amplitudes of adjacent lasers, and their distribution can be seen in Figure 3-6, where, (a) shows the measured AC signal ratios of 2^{nd} laser to 1^{st} and the distribution over 15 minutes, (b) shows the same quantities for 3^{rd} to 2^{nd}, (c) 4^{th} to 3^{rd}, where 1^{st}, 2^{nd}, 3^{rd} and 4^{th} lasers refer to increasing source-detector separations.

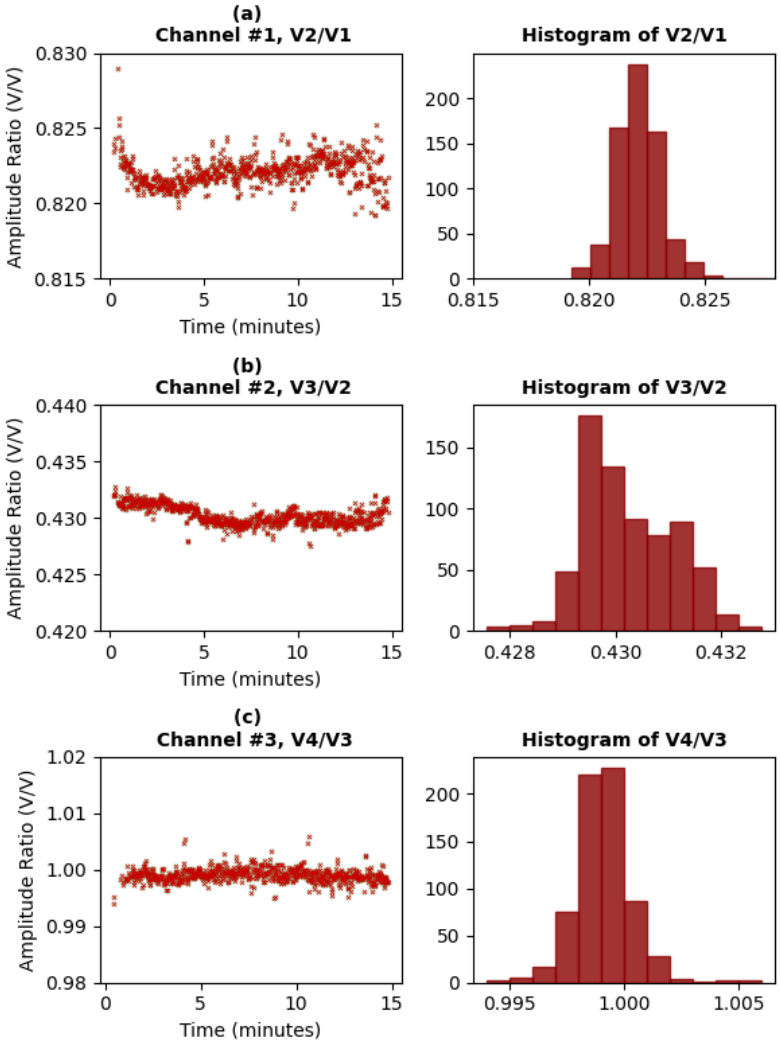

Figure 3-6: (a) The amplitude of 2nd laser normalized to 1st. (b) The amplitude of 3rd laser normalized to 2nd. (c) The amplitude of 4th laser normalized to 3rd. All are 830 nm lasers.

Similarly, Figure 3-7 shows the measured phase shifts between adjacent lasers, with (a) showing the phase shifts between 2nd & 1st, (b) between 3rd & 2nd and (c) between 4th & 3rd lasers.

Finally, Figure 3-8 shows the distribution of measured μ_a and $\mu_s\prime$ over 15 minutes, with (a) & (b) showing the μ_a and $\mu_s\prime$ for 690 nm lasers respectively, and (c) & (d) showing the μ_a and $\mu_s\prime$ for 830 nm lasers respectively.

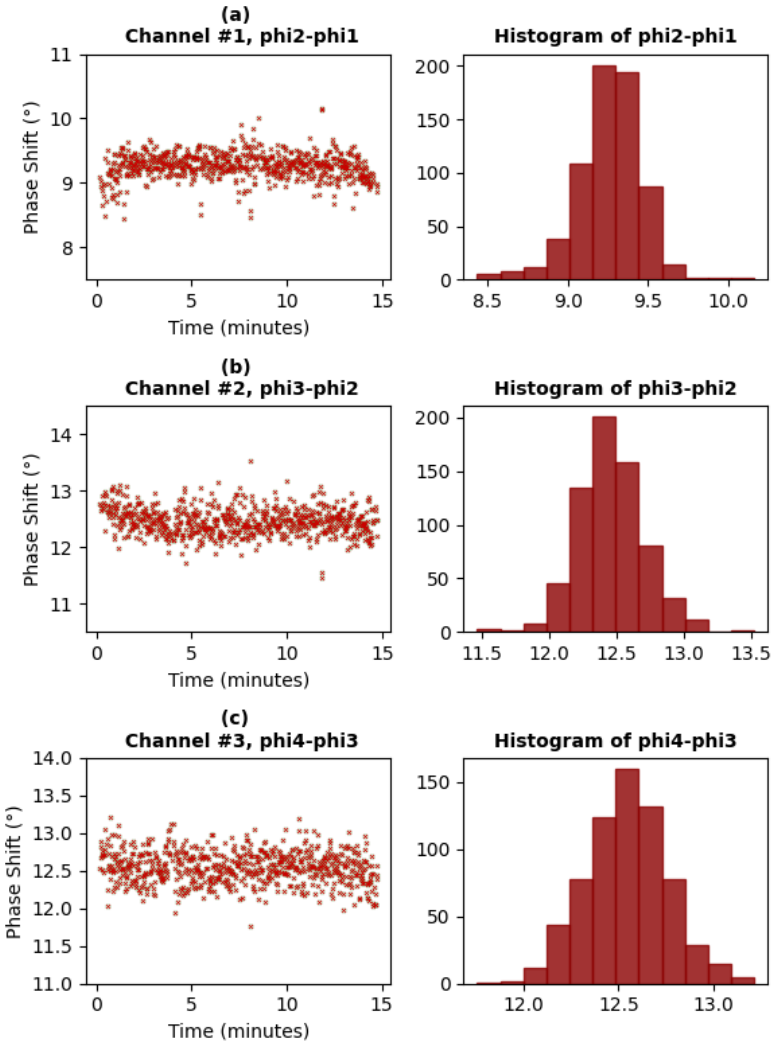

Figure 3-7: (a) The measured phase shift of the 2nd laser with respect to the 1st. (b) The measured phase shift of the 3rd laser with respect to the 2nd. (c) The measured phase shift of the 4th laser with respect to the 3rd.

It can be seen that there is little to no drift over time, but there are occasional instantaneous spikes for singular data frames. These sudden spikes are due to random

Table 3.3: Comparison between ISS model 96208 and this work.

	ISS model 96208		This work	
Parameter	690nm	830nm	690nm	830nm
μ_a uncertainty (mm^{-1})	0.00007	0.00006	0.00025	0.00018
$\mu_s\prime$ uncertainty (mm^{-1})	0.005	0.004	0.087	0.058
μ_a (mm^{-1})	0.0015	0.0013	0.0014	0.00114
$\mu_s\prime$ (mm^{-1})	1.023	0.785	0.880	0.764
Size	36.2x28.9x14.6cm		12x11.5x5cm	
Cost	>$20000		$1200	

errors, and they are many standard deviations away from the data, therefore, are of no interest to us. The distribution of all the quantities resembles a Gaussian distribution as expected. We also compared the parameters of our instrument with the commercial instrument from ISS in Table 3.3, where one can see that our design achieved comparable performance at a much lower size and cost [48].

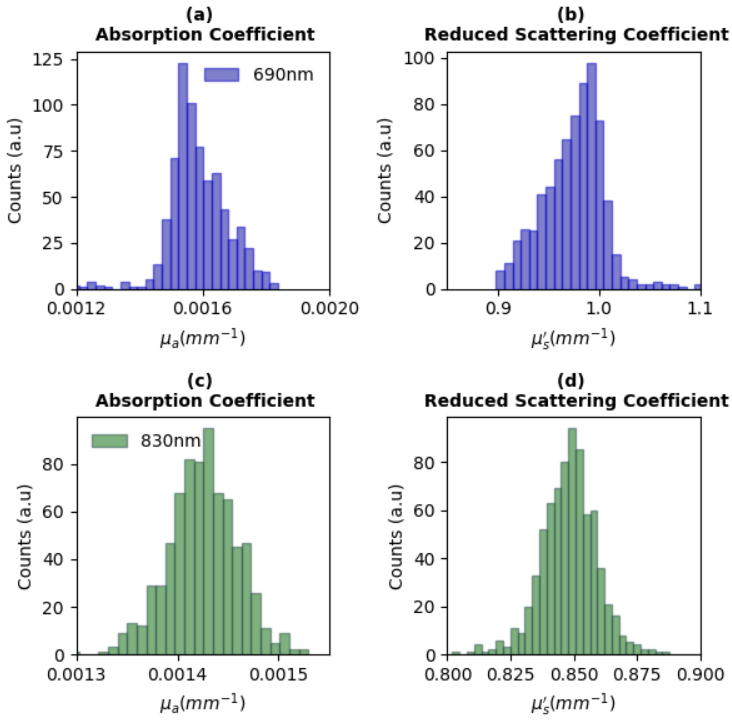

Figure 3-8: (a) & (b) The distribution of the measured μ_a and $\mu_s\prime$ respectively for 690 nm. (c) & (d) The distribution of the measured μ_a and $\mu_s\prime$ respectively for 830 nm.

3.4 *in-vivo* Occlusion Tests

After validating the instrument on solid phantoms, arterial and venous occlusion tests were performed on the human forearm. The probe was placed on the brachioradialis muscle on the right forearm and a regular blood pressure cuff was placed just above the elbow. The optical power of each laser diode is set to meet the ANSI Z136.1 laser safety standards [5]. Different pressures were used for the venous and arterial occlusion tests. The procedures were reviewed and approved by the Health Sciences Internal Review Board (HS IRB) at Tufts University.

3.4.1 Venous Occlusion Tests

In the venous occlusion test, the subject remained at rest for 30 s, then a pressure of 60 mmHg was applied for 60 s, after which the pressure was released, additional measurements were taken for another 60 s. A pressure of 60 mmHg can occlude the veins, but has a minimum influence on arterial blood flow. As a result, arterial blood continues to flow into the forearm, which will result in an increase in both HbO_2 and HbT. In Figure 3-9, the concentrations of chromophores can be seen during a venous occlusion test. The occlusion was marked with the green shaded region, 30-90 s. During the occlusion test, the HbR cannot leave the forearm, but the HbO_2 can enter the forearm as the artery is not occluded. As expected, HbO_2 enters the lower arm, resulting in an increase in concentration. HbT naturally followed these changes and increased during the occlusion test, as expected [73]. After the pressure is released, HbO_2 leaves the lower arm and the concentrations return to baseline levels.

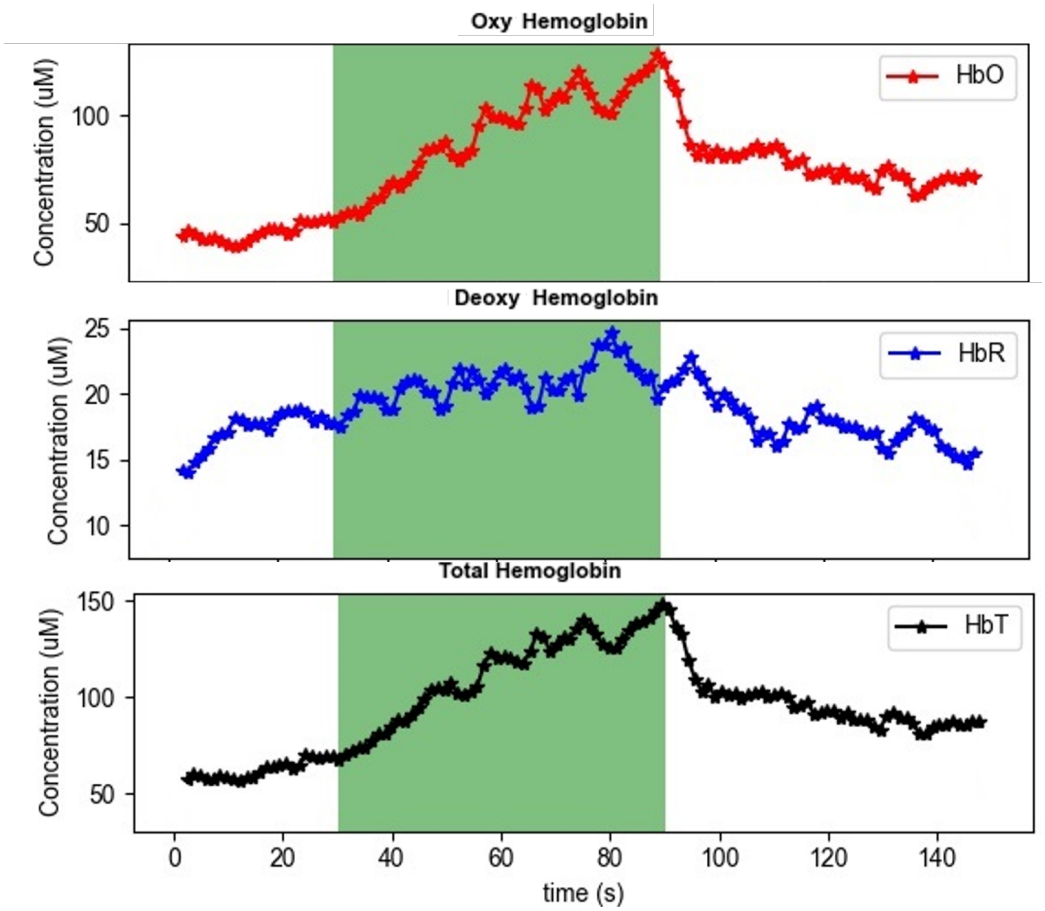

Figure 3-9: Venous occlusion test with measured chromophore concentrations

3.4.2 Arterial Occlusion Tests

In the arterial occlusion test, the procedure was identical except for pressure. In this experiment, the applied cuff pressure was 300 mmHg. In this condition, both the arteries and the veins are occluded. Therefore, the expected behavior is that while the HbR concentration increases, the HbO_2 concentration falls during occlusion and the HbT stays roughly the same. Figure 3-10 shows an arterial occlusion test. The occlusion is again indicated with the green shaded region, 30-90 s. As expected, it is observed that when occlusion starts, HbR increases and HbO_2 decreases by roughly the same amount; hence, HbT remains the same. After the cuff is released, there is a rush of HbO_2 because the artery is reopened; therefore, an increase in HbO_2 and HbT is observed. All results are consistent with previously reported data.

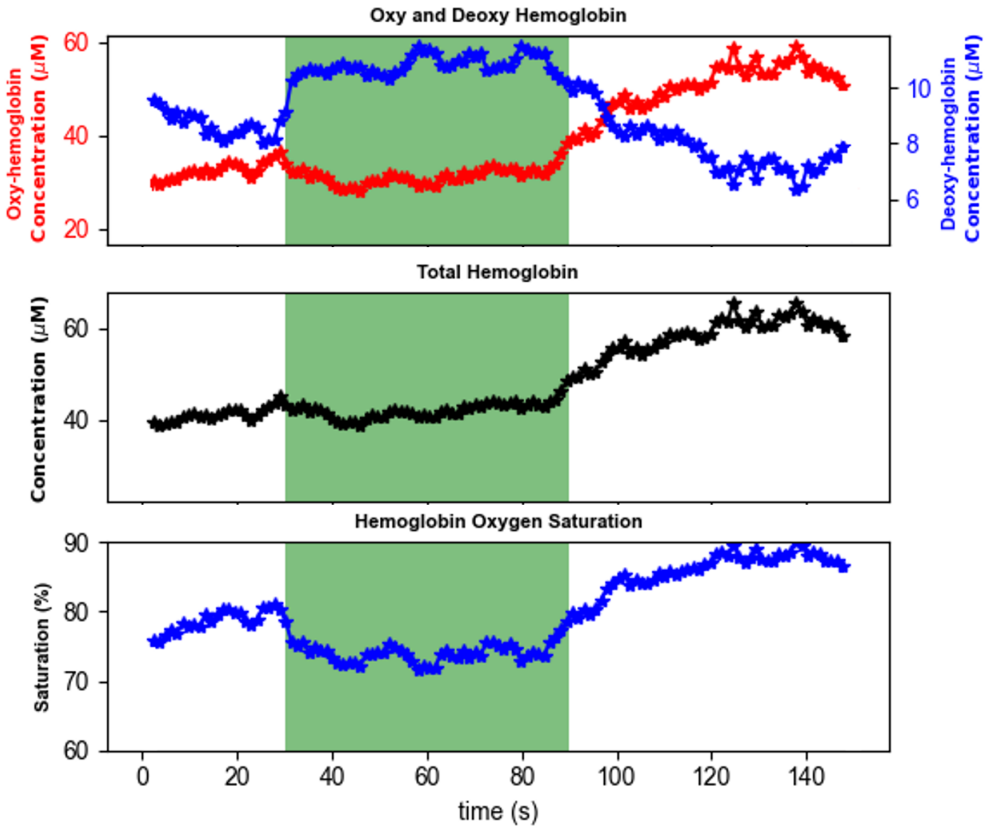

Figure 3-10: Arterial occlusion test with measured chromophore concentrations and oxygen saturation

3.5 Discussion

The Generation 2 FD-NIRS instrument presented here achieves a performance approaching that of the commercial ISS instrument, while offering the advantages of portability and reduced hardware complexity. Validation with tissue-mimicking phantoms demonstrated absorption coefficient recovery errors below 15 % and reduced scattering coefficient recovery errors below 20 % across a physiologically relevant range. These levels of accuracy are comparable to those typically obtained with the ISS instrument, indicating that quantitative fidelity can be preserved even in a compact implementation.

Physiological tests further highlighted the capability of the instrument for tissue monitoring. During arterial occlusion, the expected increase in HbR and the corresponding decrease in HbO_2 were observed, with HbT remaining nearly constant.

Following release of the cuff, rapid overshoot was observed due to rapidly increasing HbO_2 and HbT concentrations. The ability to capture these characteristic dynamics confirms that the instrument maintains sufficient sensitivity and stability for *in-vivo* measurements.

Several design choices were key to balancing miniaturization with performance. The use of a large-area photodetector directly coupled to optical fibers enabled efficient photon collection at source-detector separations up to 35 mm, providing sensitivity to deeper tissue layers. A fully differential analog front-end improved performance by removing the common-mode noise, while down-conversion enabled sampling rates much lower than the modulation frequency.

Despite these strengths, the instrument has limitations compared to the ISS device. The narrower dynamic range restricts the maximum source-detector separation and requires solutions such as neutral density filters to not saturate some channels. The measurement rate, currently limited by the multiplexing scheme, remains below 1 Hz and restricts the capture of fast hemodynamic events.

In summary, Generation 2 instrument demonstrates that the essential quantitative capabilities of FD-NIRS can be achieved in a miniaturized and portable format. The instrument can recover absorption changes and resolve physiologically relevant dynamics, establishing a foundation for wearable implementations. Further development in data acquisition methods, dynamic range, temporal resolution, and calibration-free techniques will be important for the future development of this technology toward widespread clinical and field use.

Chapter 4

Generation 3 Instrument: Integrated Readout with Demodulator circuits

> Once the number three, being the third number, be reached, then lobbest thou thy Holy Hand Grenade of Antioch towards thy foe, who being naughty in my sight, shall snuff it.
>
> Cleric, Monty Python and the Holy Grail

In Chapter 3 the Generation 2 Instrument was presented. The Generation 2 Instrument represented a major step towards miniaturizing the FD-NIRS technology by integrating signal generation onto the instrument. However, readout and experiment control was still performed by a benchtop NI DAQ. The topic of this chapter, the Generation 3 Instrument, goes one step further with the miniaturization effort and integrates the amplitude and phase measurements onto the instrument via the demodulator circuits. Demodulator circuits carry the amplitude and phase information of signals at low frequencies to DC voltage levels, making their sampling trivial, the details of which will be explained in detail in Section 4.1.1. In addition, experiment control functionality is done by a Raspberry Pi 4, thus removing the only remaining

benchtop instrument, the NI DAQ. Moreover, the probe geometry is changed to an DS/SC probe (see Section 2.3). This generation was designed from the ground up with the DS/SC approach, which enables this instrument to be selective to deeper tissue and to conduct absolute measurements without calibration. In Section 4.1, the architecture of the Generation 3 Instrument will be explained along with details of the demodulator circuits, and in Section 4.2, the experimental results collected from tissue mimicking solid phantoms will be presented.

4.1 Hardware description

Similarly to previous generations, this device also employs heterodyne down-conversion using light sources modulated at a single frequency, with time-division multiplexing. However, this instrument was designed to interface with the DS/SC probe described in 2-3. The complete instrument is shown in Figure 4-1, consisting only of a PCB of 14×17 cm^2, a Raspberry Pi 4 and the DS/SC probe.

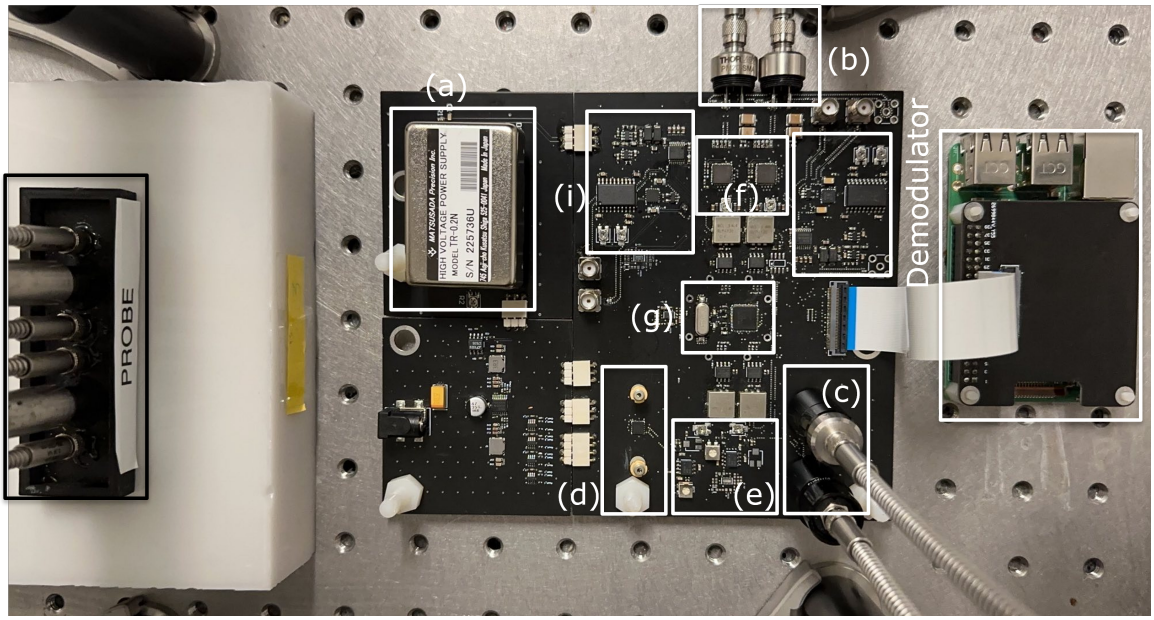

Figure 4-1: Photo of the instrument. Panels show the following: (a) APD supply, (b) APDs, (c) & (d) 830 and 690 nm lasers respectively, (e) laser drivers, (f) Application Specific Integrated Circuits, (g) Direct Digital Synthesizer, (h) Raspberry Pi 4 and (i) Demodulator circuits.

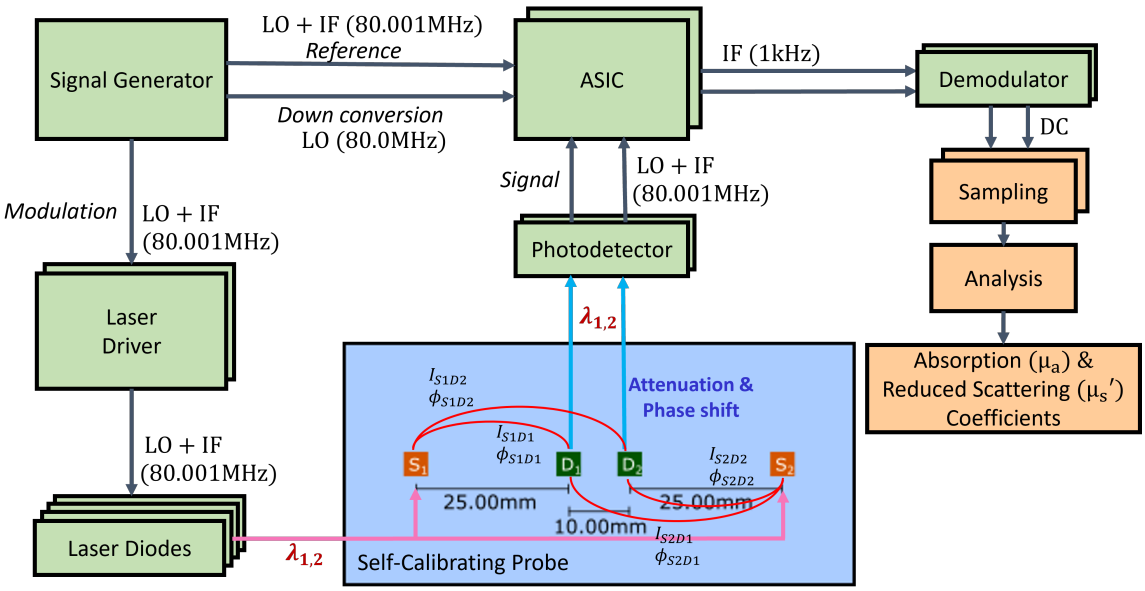

Figure 4-2: Block diagram of the instrument showing all the major building blocks. The green color denotes all the components integrated onto a single PCB, the orange are the off-board blocks, and the blue block is the DS/SC Probe. LO: Local oscillator, IF: Intermediary Frequency, ASIC: Application Specific Integrated Circuit, $S_{1,2}$: Source locations, $D_{1,2}$: Detector locations, I: Intensity, ϕ: Phase.

The key building blocks are shown in Figure 4-2. As mentioned in Chapter 1, for an FD-NIRS instrument that employs heterodyne down-conversion, two signals at radio frequencies that are separated by an intermediate frequency ($IF = 1$ kHz) are needed. In the case of this instrument, these two signals were set to 80 MHz and 80.001 MHz. The 80.001 MHz signal is used to modulate the intensity of the light sources. Therefore, the detected photon density wave from the medium will also be modulated at this frequency. With the heterodyne readout scheme, the information encoded in the recovered signal will be down-converted to 1 kHz. 1 kHz is low enough to be properly processed by the demodulator circuits, while high enough to be unaffected by low-frequency noise sources, such as 1/f noise.

Similarly to previous generations, an AD9959 DDS is used for signal generation. The reasoning behind why a DDS was used instead of simpler solutions and the specifications of this particular component were explained in detail in Section 3.1.2.3 One of the output channels modulates the intensity of the four laser diodes through two laser driver circuits, each of which drives a pair of laser diodes of the same wavelength,

830 nm or 690 nm. Another channel is fed into the ASICs as the reference signal against which the phase shift of the recovered signal is defined. The last two channels are used as differential local oscillator signals for heterodyne down-conversion. The laser driver circuits are a modified version of the well-known linear current regulator topology [74]. In this implementation, the circuit uses the monitoring current from the laser diodes, which is proportional to the optical power, to mitigate the effects of aging and thermal drifts. The details of the laser driver and how the feedback mechanism uses the monitoring currents were explained in detail in Section 3.1.2.2.

The DS/SC probe consists of two source locations and two detector locations, where the detector locations are sandwiched between the source locations. In this configuration, we have four source-detector combinations for each wavelength (as is typical for a DS set) [53]. The geometry of the probe enables this instrument to overcome the systematic errors that are multiplicative in intensity and additive in phase [52, 56] (see Section 2.4). Two fibers deliver light from one pair of laser diodes (either at 690 nm or 830 nm) to the source locations on the probe (indicated with S_1 and S_2 in Figure 4-2). In other words, in this generation of the instrument, only one wavelength can be incident on the medium without manually changing to which of the laser diodes the fibers are connected. This means that this instrument is not ready to be used for *in-vivo* experiments which require at least two wavelengths to measure the HbO_2 and HbR concentrations. However, this is a simple issue of changing the simple source fibers with bifurcated fibers and is not pertinent to the concept we set out to test with this version of the instrument.

During operation, each laser diode is alternately turned on for 50 ms, sending light to the source locations one at a time. After the light from the laser diodes is attenuated and scattered in the tissue (medium), two fibers collect the light from the detector locations on the probe (D_1 and D_2 in Figure 4-2) and guide the detected light to the photodetectors. The photodetectors used in this instrument are S9251-15 APDs from Hamamatsu. The specifications of these photodetectors were explained in detail in Section 3.1.1.2.

The low level electrical signals from the APDs (at 80.001 MHz) are then processed

by the custom-designed, low-noise analog front-end ASIC, designed in 130 nm IBM process [60] (see Section 3.1.2.1). Note that since there are two APDs, to process their outputs, either a switch to multiplex two APDs to a single ASIC is needed, or there needs to be one ASIC per APD. However, the former approach is unsuitable since the recovered light is on the order of nW to pW (considering a source on the order of mW), and the APD outputs are on the order of a few µA. The latter approach is selected since the ASICs will amplify any electronic noise contribution from additional components.

Each ASIC interfaces with one of the APDs and amplifies its output current via a low noise transimpedance amplifier (TIA) [60]. Then, the amplified signal is filtered to reject the out-of-band noise and finally down-converted to a 1 kHz signal. The ASIC uses the differential LO signal from the signal generator to accomplish the heterodyne down-conversion. The 1 kHz output signals contain all the information needed for the FD-NIRS, namely the intensity (I) and phase (ϕ) of the photon density wave recovered from the medium in the form of the amplitude and the phase shift of these electrical signals. The 1 kHz signals are ordinarily slow enough to be sampled with low-power ADCs; however, this was not an option in this instrument. The reason why the 1 kHz signals are not sampled directly by the ADCs is that the digital controller on this instrument is a Raspberry Pi. Due to the nature of the operating system that runs in a Raspberry Pi, it is not feasible to achieve predictable and repeatable sampling intervals for the ADCs. This means that the time difference between each consecutive sample will be undefined, which means that the computed amplitude and phase information will be random for all intents and purposes. However, if the information is encoded in DC levels, this sampling interval issue becomes irrelevant. This is where the demodulator circuits come into play. The 1 kHz signals are processed in the analog domain in the demodulator circuits, and their phase and amplitude information is translated into DC voltage levels, which are then sampled by two 16-bit ADS8685 ADCs [75]. These ADCs were chosen for their ease of integration, since this component does not need external clock sources, external voltage references, or ADC drivers. They are basically standalone analog-to-digital converter solutions.

Additionally, their integrated programmable amplifier allows for bipolar input, i.e. the inputs can be negative voltages as well. This capability will become important in Section 4.1.1, when the output of the demodulators can be negative.

Once the amplitude and phases are collected, μ_a and μ_s' of the medium (see Section 2.4) are computed. The Raspberry Pi 4 is also used to organize the time-division multiplexing, program the DDS, provide an interface for the user to control the experiment flow, and monitor the instrument's state. Time-division multiplexing of all the lasers, sampling of the outputs, and processing the data for one frame takes about 1.4 s, which corresponds to a 0.7 Hz acquisition rate per DS/SC data point of amplitude and phase of both wavelengths.

4.1.1 Demodulator

Demodulator circuits deserve some discussion as to how they work. Same as the previous generations, each ASIC has two inputs, one from an APD and the other from the DDS, and has two outputs. The purpose of the demodulator circuits is to measure the amplitude of the output that is associated with the APD and the phase difference between the two outputs. To do this, each demodulator circuit is designed with two inputs and one output using AD630 from Analog Devices [76]. The output of the demodulator circuit contains information about the amplitude and phase difference between the two ASIC outputs.

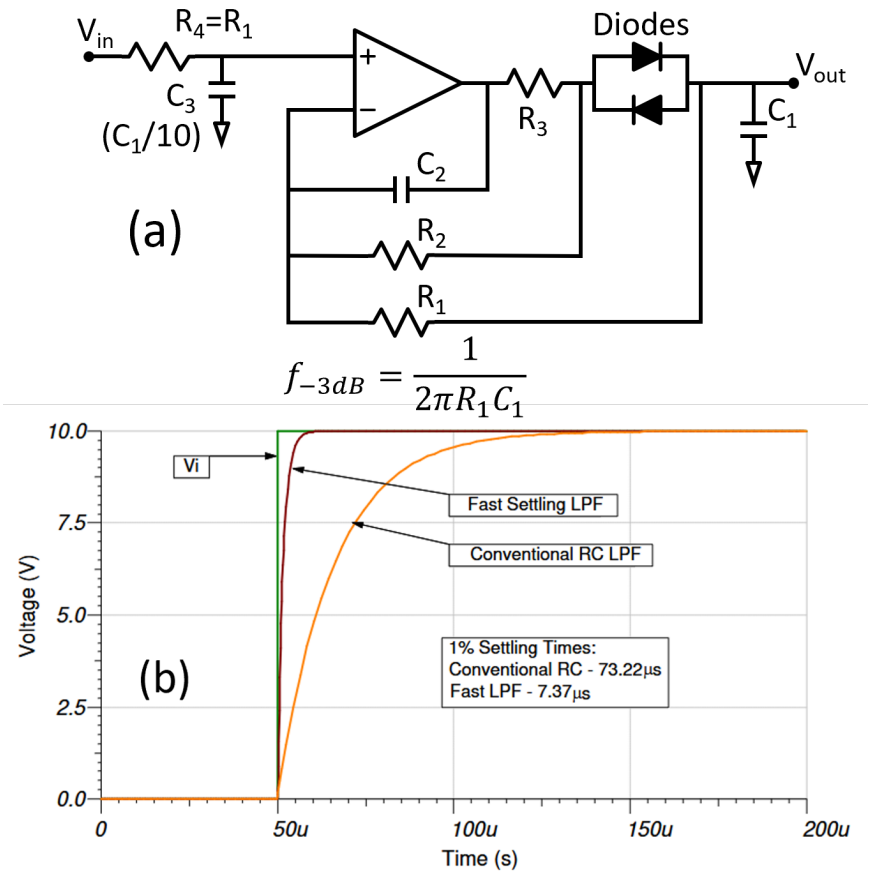

Figure 4-3: (a): The schematic of the fast settling low-pass filter; (b): Comparison between the settling time of the fast settling low-pass filter and a conventional RC filter to a step response.

Assuming that sinusoidal waveforms are available at the inputs of the demodulator, the intrinsic output of the demodulator is a $\sin^2$ waveform, since the internal operation of the demodulator is based on the multiplication of two inputs. The DC average of this $\sin^2$ waveform contains information about the amplitude of its two inputs and the phase difference between them. Therefore, a low-pass filter was designed at the outputs of the demodulators to extract the DC average. Since only the DC component was required, the passband of the filter was designed to extend only a few Hz. This introduces a trade-off: The settling time of a conventional low-pass filter is governed by its time constant τ, so that a narrower passband results in slower settling. However, allowing the passband to extend further allows more frequency content of the $\sin^2$ to pass, which contaminates the measurement. This behavior is

problematic because the instrument relies on time-division multiplexing of the laser sources, for which long settling times were not acceptable. To break this trade-off, a special fast-settling low-pass filter was implemented. The schematic of the fast-settling filter can be seen in Figure 4-3(a), and the comparison of this filter's step response with basic RC filters can be seen in Figure 4-3(b). This filter topology can extract the DC average of the $\sin^2$ output while substantially reducing the settling time. As a result, the DC average of the demodulator output could be measured with sufficient accuracy without introducing too long settling times that would interfere with the time-division multiplexing scheme.

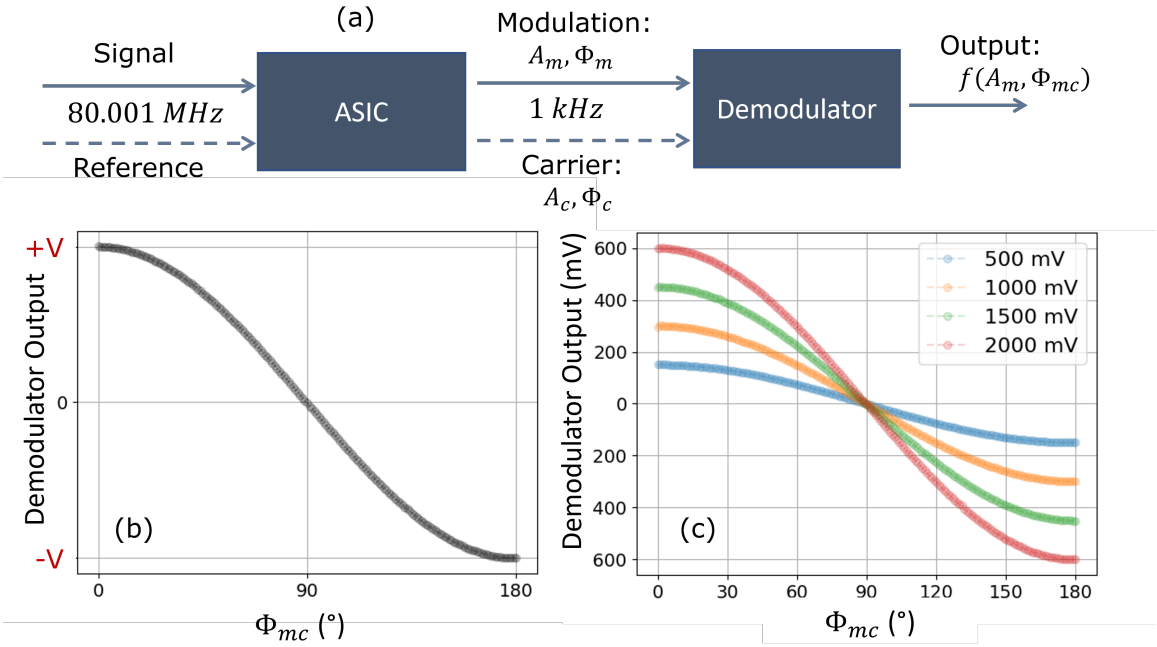

Figure 4-4: (a): The connections between the ASIC and Demodulator. DC average of the demodulator circuit's output with the phase difference between two inputs swept from 0° to 180°; (b): A_c swept and A_m kept constant. (c): A_m swept and A_c kept constant.

There are several important properties of the demodulator circuit. In order to explain the properties of the demodulator circuits, the amplitudes and phases of the two inputs of the demodulator will be denoted as A_m, Φ_m, A_c, and Φ_c, and the phase difference between them will be denoted as Φ_{mc}. Assuming that two different sin signals are available at the two inputs of the demodulator (Figure 4-4(a)) with

arbitrary values of A_m and A_c, the output shows a symmetric curve about 90° when the phase difference between the two inputs (Φ_{mc}) is swept and the output is equal to zero at 90°(Figure 4-4(b)). In panel 4-4(b), the output of the demodulator is plotted four times with four different values of A_c, with the same value of A_m. This shows that the output depends only on A_m and Φ_{mc}, but is independent of A_c. Furthermore, panel 4-4(c) shows the output with four different values of A_m with constant A_c. This suggests that the output appears to be linearly scaled with A_m. This was verified by connecting the modulation and carrier inputs together to enforce a zero phase difference (Figure 4-5(a)) and focusing only on the sliver where $\Phi mc = 0$ (Figure 4-5(b)), allowing the only variable left to be A_m (Figure 4-5(c)). Under this condition, sweeping A_m and applying linear regression confirmed a linear relationship.

This method (connecting the two inputs of the demodulator together) emerges as a method to measure the amplitude of this signal. In other words, one of the output channels of an FD-NIRS ASIC can be extracted directly from the demodulator output using this method.

Once A_m was determined, the operating curve on which the demodulator could be reconstructed (e.g., the green trace on Figure 4-4 if A_m was determined as 1500 mV), leaving the output as a function of the phase difference between modulation and carrier signals, Φ_{mc}. Although this time the dependence is not linear, it is well described by a sinusoidal fit with A_m as the amplitude of the sinusoid, achieving a fit quality of $R^2 = 0.99$. Therefore, once A_m is measured, the Carrier input can be reconnected to the second output channel of an ASIC, and the phase difference between the channels can be extracted.

Another important observation is that the curve is approximately linear near 90°, and has a higher slope than the edges where Φmc is closer to 0° or 180°. To take advantage of the higher linearity and improved sensitivity in this region, during regular operation of the instrument, the phase of the modulation signal was adjusted relative to the reference using the DDS, ensuring that the circuit operated near 90°, which improves the SNR of the instrument for phase measurements.

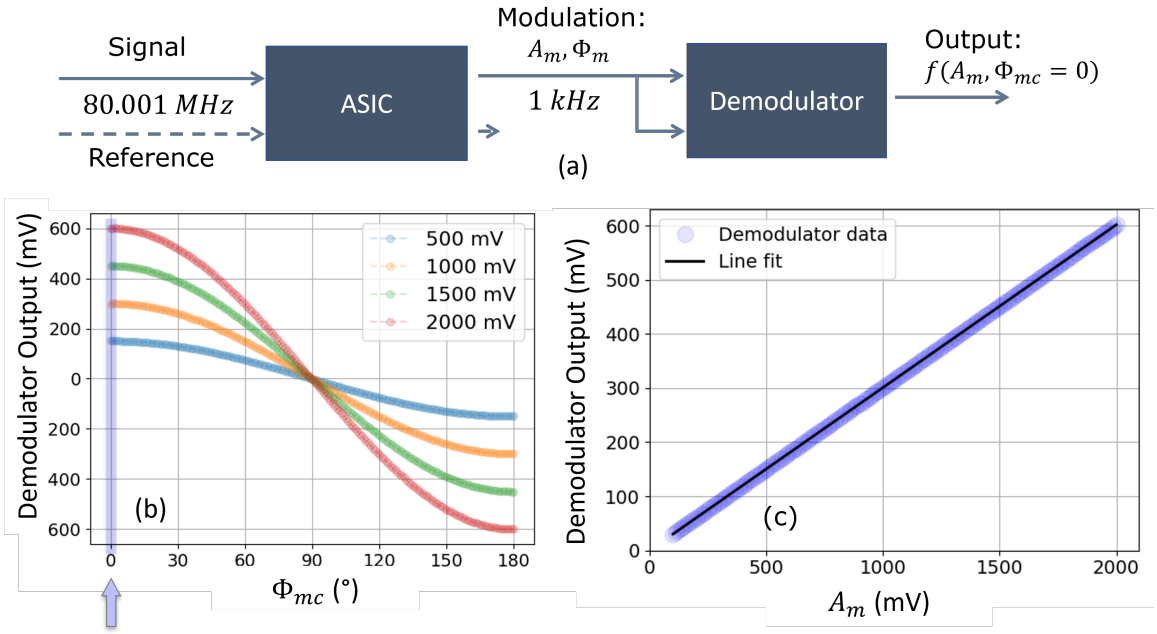

Figure 4-5: (a): The connections between the ASIC and Demodulator. (b): The operating point of the demodulator where the signals at both inputs are the same. (c): Demodulator output when A_m swept between 20 mV and 2 V.

4.2 Results

As always, the instrument must be characterized and its performance validated with tissue mimicking phantoms. For these purposes, a solid phantom with known optical properties (μ_a ~0.006 mm^{-1}, $\mu_s\prime$ ~0.7 mm^{-1} at the wavelength of interest here) was used. This solid phantom was fabricated in-house using titanium dioxide and India ink as scattering and absorbing components, respectively. Testing on a phantom allows one to characterize the instrument in terms of stability and noise, as well as determine if its performance is suitable for *in-vivo* experiments.

Figure 4-6 shows the measured amplitude and phase slopes during a 1 h long experiment. As mentioned before, this instrument uses the DS/SC probe instead of the multi-distance probe, so "Pair 1" and "Pair 2" in Figure 4-6 refer to the amplitude and phase slopes gathered by one source and two detectors. For example, S_1 as the source and D_1 and D_2 as the detectors of Figure 2-3.

The slope gathered from each pair corresponds to an SS from 2.16, and their arithmetic average, DS can also be seen under the "Average" legend in Figure 4-6.

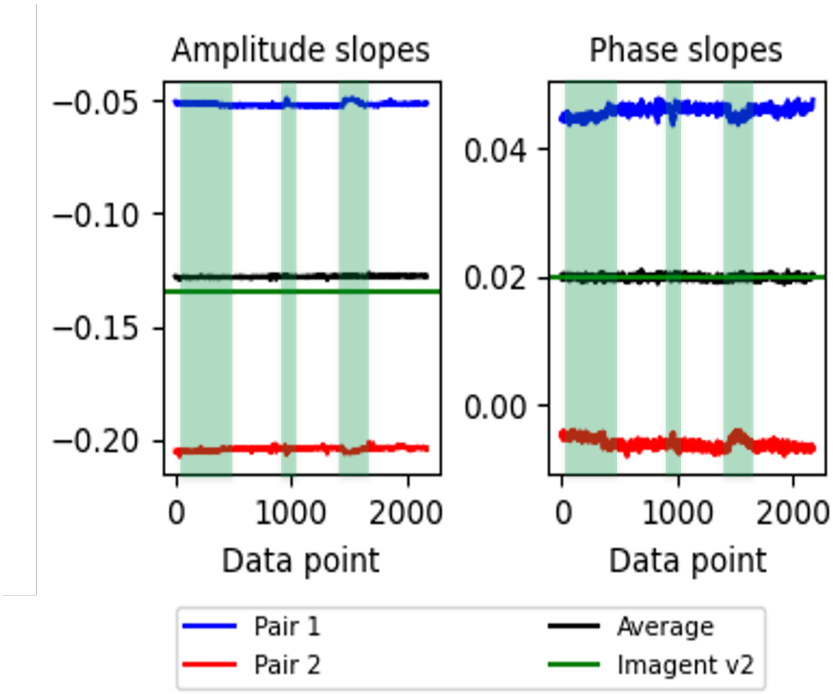

Figure 4-6: Amplitude and phase slope results of an 1 h long solid phantom experiment. "Pair 1" and "Pair 2" denotes to results from one detector and two sources and "Average" denotes their arithmetic average.

The solid green line is the true slope that was measured with an ISS Imagent v2. In the green shaded regions, some events that occurred during the experiment can be seen. These events caused temporary changes in slope measurements. However, thanks to the inherent self-calibration property of the DS/SC probe geometry, the effects of these events affect the slopes in the opposite manner, and their average stays unaffected. Here, to quantify the noise level of measured phase slopes, the standard deviation was used, as opposed to the standard deviation over mean, to quantify the noise over signal ratio for amplitude slopes. During this 1 h experiment, a 0.5 % noise over signal for the amplitude slope, and 0.25° standard deviation on the phase is measured.

After measuring the amplitude and phase slopes, the absorption and reduced scattering coefficients of the medium can be calculated using 2.9 and 2.10. During this experiment, errors of 8.9 % for μ_a and 4.9 % for $\mu_s\prime$ were achieved for the 690 nm laser diodes, and errors of 12.1 % and 11.1 % were achieved for the 830 nm laser diodes,

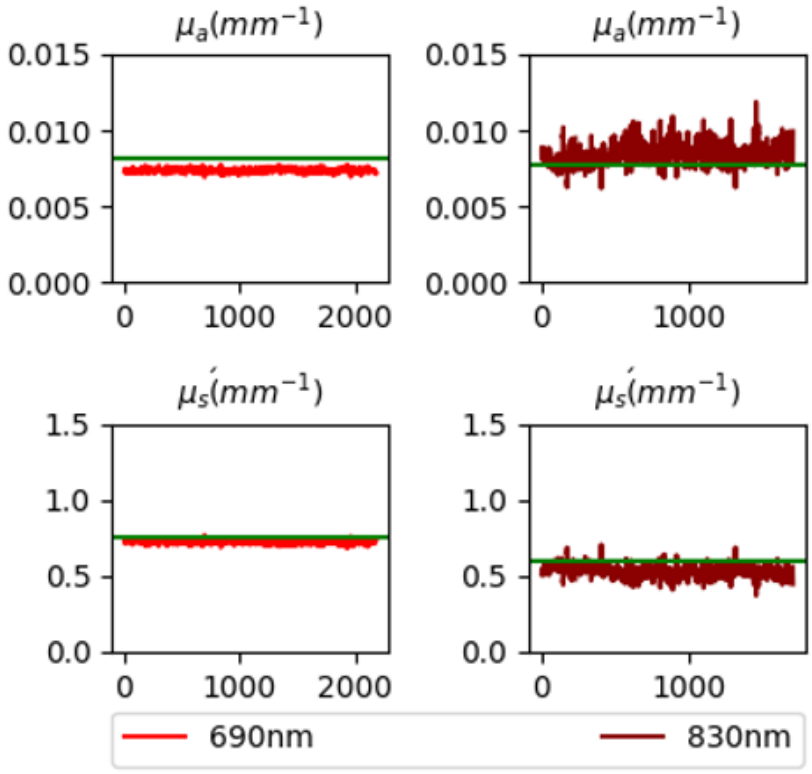

Figure 4-7: Measured absorption and reduced scattering coefficients during 1 h solid phantom experiment at 690 nm and 830 nm. The green line denotes the "ground truth" which was measured with Imagent v2.

assuming the ISS Imagent v2 as the ground truth. The corresponding plots can be seen in Figure 4-7

4.3 Discussion

The Generation 3 instrument was designed from the ground up around the DS/SC probe, which served as the central element of the system architecture, guiding decisions such as two APDs and two ASICs. In addition to all major functional blocks such as laser drivers, APDs, ASICs, DDS etc., the readout scheme in the form of the demodulator circuits was also integrated onto a single compact printed circuit board to create a fully portable and calibration-free platform. The DS/SC approach effectively cancels out systematic errors that are multiplicative for intensity and additive for phase

measurements, enabling absolute optical property recovery without pre-calibration. The demodulator circuit played a central role in enabling accurate amplitude and phase recovery by translating the phases and amplitudes of the heterodyne down-converted signals into DC voltages. To meet the timing requirements of time division multiplexing, an unconventional low-pass filter topology was implemented to achieve a narrow bandwidth for DC extraction with rapid settling. Although this approach helped with the settling time, the demodulator stage remained a source of limitation, constraining both the signal-to-noise ratio and the stability of optical property estimation. The performance of the instrument was evaluated through extended measurements in tissue-mimicking solid phantoms. The amplitude slopes were recovered with a noise-to-signal ratio of approximately 0.5 %, while the phase slopes demonstrated a standard deviation of 0.25°. The DS/SC geometry further demonstrated resilience against perturbations, with the dual-slope average remaining stable even under transient disturbances. The absorption and reduced scattering coefficients were measured with errors of 8.9 % and 4.9 % at 690 nm, and 12.1 % and 11.1 % at 830 nm. However, further validation in human experiments was not pursued because of the limitations of the demodulator circuit, which continues to restrict both signal-to-noise ratio and accuracy.

Chapter 5

Generation 4 Instrument: Integrated readout with microcontroller for improved stability

Amen.

Brother Maynard,
Monty Python and the Holy Grail

In the previous chapter, the Generation 3 instrument was presented with solid phantom results. This instrument was a ground-up new design, since it was designed with Dual-Slope / Self-Calibrating probe in mind. Moreover, this design integrated the readout functionality onto the instrument via the demodulator circuits, and hence the final benchtop instrument was finally removed. The demodulator circuit approach worked decently; however, overall performance, especially stability performance, was insufficient. This was due to the nature of the demodulator circuits, where the output was a $\sin^2$ waveform and the amplitude or phase information was encoded in the DC average of this waveform. The DC average was extracted by fast-settling low-pass filters (Figure 4-3). This specific topology was selected because of the settling time constraints imposed by the time division multiplexing technique that was used. Although this filter topology settled an order of magnitude faster than a conventional

RC low-pass filter of the same order, its output's frequency contents were still strong enough to affect the overall stability of the instrument.

The development of the Generation 4 instrument focused primarily on addressing the limitations imposed by the demodulator stage. In this design, the down-converted signals are directly sampled using an STM32 microcontroller, which has integrated high-resolution ADCs. Unlike the earlier Raspberry Pi platform, which lacked mechanisms to enforce precise sampling intervals and therefore produced data at effectively random time points, the STM32 provides deterministic sampling for its integrated ADCs. In this context, deterministic sampling means that the interval between successive samples is fixed and known, which is essential for applying Fourier-based algorithms to accurately recover both the amplitude and the phase difference of the down-converted signals. This idea removes the primary weakness of the prior design and establishes a better foundation for reliable amplitude and phase recovery. Raspberry Pi is still being used in this generation, but only for time-division multiplexing, the graphical user interface (GUI) for experiment flow control, and data processing. Performance validation in tissue-mimicking phantoms demonstrated high stability and low noise, with intensity and phase precision sufficient for accurate recovery of absorption and scattering coefficients. Subsequent *in-vivo* testing during a vascular occlusion experiment confirmed the system's ability to track hemodynamic changes in real time, establishing this generation as the first practical step toward validation on human subjects.

5.1 Hardware description

The key building blocks are shown in Figure 5-2. This block diagram looks very similar to the block diagram in Chapter 4 with one major difference; In this instrument, the demodulator circuits and the ADCs are replaced with an STM32G491 microcontroller. STM32G491 has integrated 12-bit ADCs, with a built-in direct memory access (DMA)) feature. This feature allows a pipeline to be constructed that can work in the background, without taking processing cycles in the microcontroller. This means

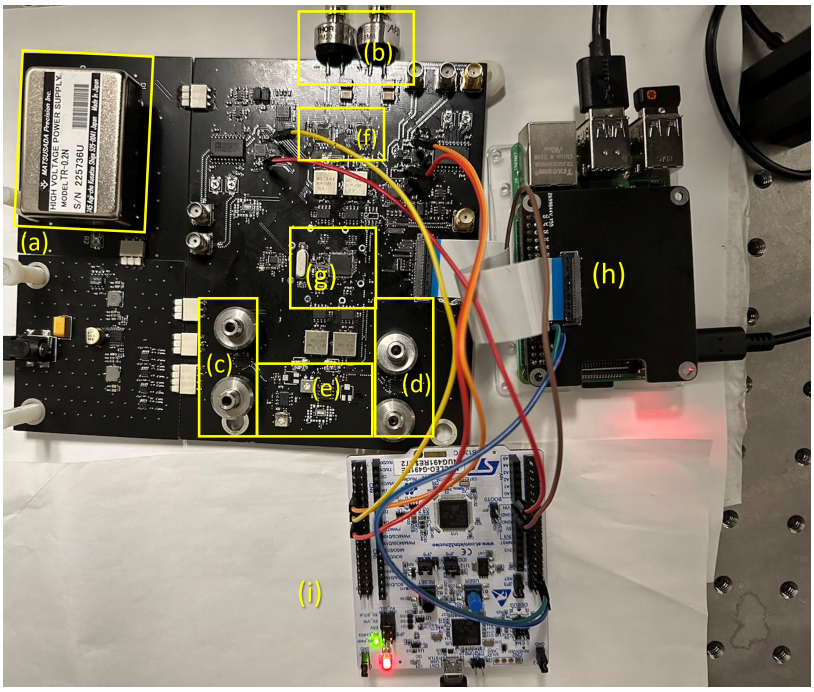

Figure 5-1: Photo of the instrument. Panels show the following: (a) APD supply, (b) APDs, (c) & (d) 830 and 690 nm lasers respectively, (e) laser drivers, (f) ASICs, (g) DDS, (h) Raspberry Pi 4 and (i) STM32G491 microcontroller.

that the built-in ADCs can keep sampling, and the samples can be written in a memory outside of the main microcontroller loop. Therefore, the sampling timing is not affected by the main loop; thus a proper sampling timing can be achieved. This feature was lacking in the Raspberry Pi 4, since the user only has access to the general-purpose input/output (GPIO) pins through the operating system that was installed. The chosen sampling rate was 44.1 kSps due to the popularity of this sampling rate in digital audio applications. Although this instrument is not intended to be used in a digital audio application, the signal being sampled falls in the same frequency range. Through the integrated ADCs and the DMA feature, amplitude and phase measurements were done in the main loop of the STM32G491 using the highly efficient built-in digital signal processing (DSP) libraries. The results were sent to Raspberry Pi 4 via serial connection, for further processing using Equations 2.9 and 2.10 and to display them on the GUI for the user. The user interface was written in the Python programming language using the PySimpleGUI package. At the time of this work being done, this package was an open-source package that was

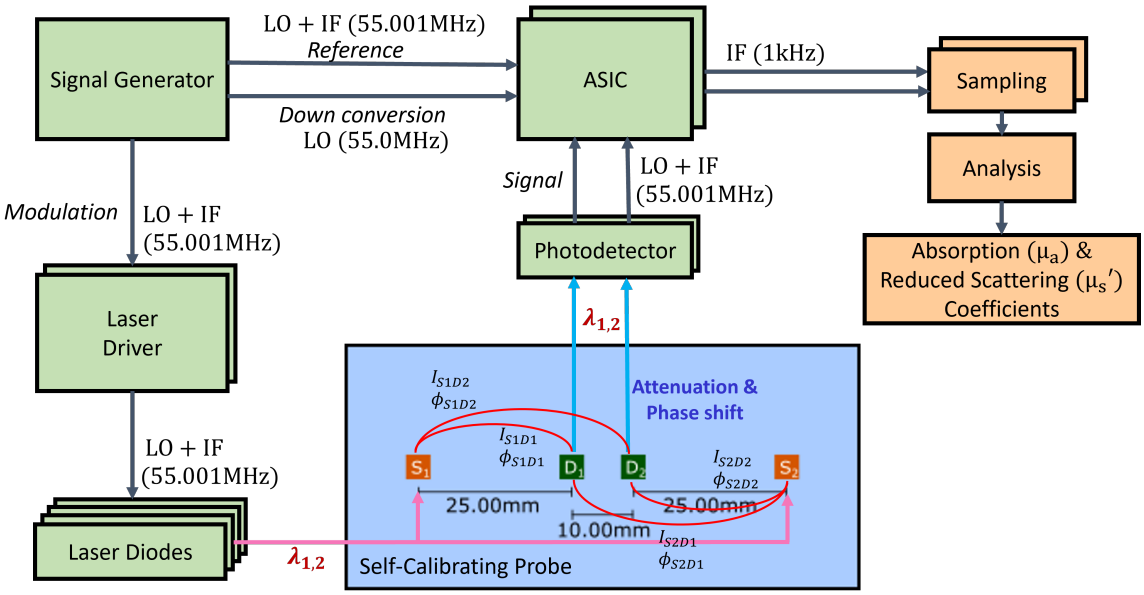

Figure 5-2: Block diagram of the instrument showing all the major building blocks. The green color denotes all the components integrated onto a single PCB, the orange are the off-board blocks, and the blue block is the self-calibrating Probe. LO: Local oscillator, IF: Intermediary Frequency, ASIC: Application Specific Integrated Circuit, $S_{1,2}$: Source locations, $D_{1,2}$: Detector locations, I: Intensity, ϕ: Phase.

free to use; however, in February 2024 this changed and the package requires a paid license now. In addition to this major difference, another minor difference between this instrument and the previous is that in this instrument the two RF signals were set to 55 MHzand 55.001 MHz. The 55.001 MHz signal is used to modulate the intensity of the light sources. With the heterodyne readout scheme, the information encoded in the recovered signal will be down-converted to 1 kHz. The final difference between these two instruments is the source fibers. In this instrument, bifurcated fibers were used instead of the previous simple fibers, because this instrument is being used for *in-vivo* experiments.

Regarding the rest of the instrument, it is mostly the same. Similarly to the Generation 3 instrument, an AD9959 DDS is used for signal generation. One of the output channels modulates the intensity of the four laser diodes through two laser driver circuits, each of which drives a pair of laser diodes of the same wavelength 830 nm or 690 nm. Another channel is fed into the ASICs as the reference signal against which the phase shift of the recovered signal is defined, and the last two

channels are used as differential local oscillator signals for heterodyne down-conversion. The reasoning behind choosing this component and its specifications were already discussed in Section 3.1.2.3. The laser driver circuits are still the modified version of the well-known linear current regulator topology [74], and how this circuit uses the monitoring current from the laser diodes, which is proportional to the optical power, to mitigate the effects of aging and thermal drifts in Section 3.1.2.2.

The DS probe consists of two source locations and two detector locations, where the detector locations are sandwiched between the source locations. Unlike Generation 3, in this instrument two bifurcated optical fibers deliver light from two pairs of laser diodes (each pair comprising one laser at 690 nm and one at 830 nm) to the source locations on the probe (indicated with S_1 and S_2 in Figure 5-2). In other words, each source location on the DS probe is connected to one laser diode at 690 nm and one at 830 nm. This change is important because using bifurcated fibers allows two different wavelengths to be sent in the medium without manually changing to which of the laser diodes the fibers are connected. This allows this instrument to be used in *in-vivo* experiments and to measure the concentrations of HbO_2 and HbR. During operation, each laser diode is alternately turned on for 50 ms, sending light to the source locations one at a time. After the light from the laser diodes is attenuated and scattered in the tissue (medium), two fibers collect the light from the detector locations on the probe (D_1 and D_2 in Figure 5-2) and guide the detected light to the photodetectors. The photodetectors used in this instrument are S9251-15 APDs from Hamamatsu. The performance and specifications of these photodetectors were discussed in Section 3.1.1.2.

Each ASIC interfaces with one of the APDs and amplifies its output current via a low noise TIA [60]. Then, the amplified signal is filtered and finally down-converted to a 1 kHz signal. The ASIC uses the differential LO signal from the signal generator to accomplish the heterodyne down-conversion. The 1 kHz output signals contain all the information needed for the FD-NIRS, namely the intensity (I) and phase (ϕ) of the intensity modulated light recovered from the medium. In the penultimate stage, the 1 kHz output signals are sampled with the integrated analog-to-digital converters

of an STM32G491 microcontroller to extract the amplitude and phase information by applying fast Fourier transform (FFT) algorithms. Once the amplitude and phase are collected, they are sent to the final stage: a Raspberry Pi 4, for the calculation of μ_a and μ_s' of the medium (see Section 2.4). The Raspberry Pi 4 is also used to organize the time-division multiplexing, program the DDS, provide an interface for the user to control the experiment flow, and monitor the instrument's state. Sweeping all the lasers, sampling the outputs, and processing the data for one frame takes about 1.4 s, which corresponds to a 0.7 Hz acquisition rate per DS data point of intensity and phase of both wavelengths.

5.2 Results

5.2.1 Solid phantom measurements

The instrument was first tested on a solid tissue mimicking phantom with known optical properties (μ_a $\sim$0.006 mm^{-1}, $\mu_s\prime$ $\sim$0.7 mm^{-1} at the wavelength of interest here). This solid phantom was fabricated in-house using titanium dioxide and India ink as scattering and absorbing components, respectively. Testing on a phantom allows one to characterize the instrument in terms of stability and noise, as well as determine if its performance is suitable for *in-vivo* experiments.

In Figure 5-3, the measured intensity and phase of the ASICs' outputs from 690 nm sources for a 30 min long solid phantom experiment is presented. Figure 5-3(a)-(d) show the intensity (I) and Figure 5-3(e)-(h) show the phase (ϕ) of all four combinations of the two sources and two detectors. Figure 5-3(i) shows changes in SS_1 and SS_2 for $\ln[r^2 I]$ slope with respect to the first point for the two SSs and DS. Figure 5-3(j) shows the ϕ absolute SSs and DS. The intensity (I) and phase (ϕ) results are denoted with their source and detector designations, and SSs are denoted by which source they are obtained from (considering they utilize both detectors). For example, the two SS measurements for phase data are obtained from phase measurements at S_1D_1 and S_1D_2 (SS_1) and S_2D_2, S_2D1 (SS_2). The average of these two SSs is the DS

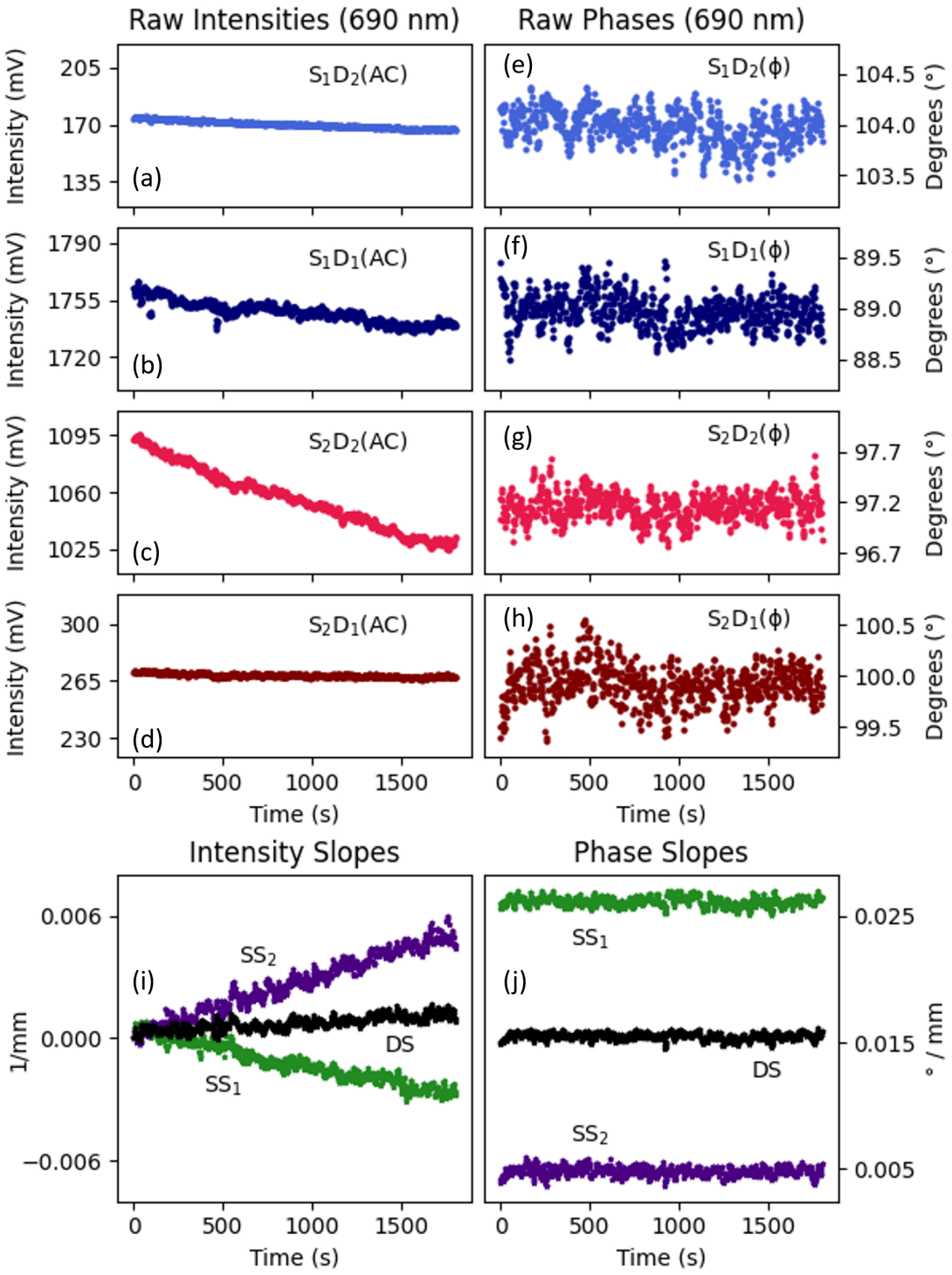

Figure 5-3: Measured intensity and phase data from 690 nm sources during a half-hour phantom experiment. Panels (a) through (d) show the intensities, and (e) through (h) show the phases for different SDs (see Figure 5-2). (i) shows the single-slope (SS) and dual-slope (DS) changes relative to the first time point for the intensities (I's), and (j) shows the absolute single-slopes (SSs) and the dual-slope (DS) for phase (ϕ).

measurement. The same logic also follows for the intensity (I) data. As mentioned in Section 2.4, the procedure for the recovery of the optical properties is based on an iterative solution of the semi-infinite medium model of diffuse reflectance and was explained in detail by Blaney et al. [55].

The most important result in Figure 5-3 is the apparent removal of instrumental drifts by the auto-calibration features of SC / DS. Due to thermal effects on the source and detector, all four intensities show varying degrees of drift, which is reflected as drift on SS_1 and SS_2 in Figure 5-3(i). However, due to the properties of the SC / DS source-detector configuration, the drift of the two SSs cancels out when calculating DS. Note that in Figure 5-3(i), the intensity slope changes with respect to the initial intensity slope (slope of $\ln[r^2 I]$) values were reported to demonstrate this autocalibration feature of the SC / DS geometries [52,56]. These initial absolute slopes are -0.164 mm^{-1}, -0.072 mm^{-1} and -0.118 mm^{-1} for SS_1, SS_2, and DS respectively.

Here, to quantify the noise level of measured ϕ's the standard deviation was used, as opposed to the standard deviation over mean to quantify the noise over signal ratio for everything else (i.e. intensities I's, etc.).

In this experiment, the average standard deviation over the mean for intensities from the 25 mm source-detector separation (S_1D_1 and S_2D_2) was 0.07 %. For the 35 mm source-detector separation this average relative error is 0.11 % (S_1D_2 and S_2D_1). For the phase, the average standard deviation was measured to be 0.069° for the 25 mm source-detector separation and 0.082° for the 35 mm source-detector separation. It should be noted that the stability metric (i.e., phase variation) is better for signals obtained from 25 mm source-detector separations than 35 mm. This is expected since the recovered signals weaken as the separation increases and the noise-to-signal ratio becomes larger. In addition, repeated probe placement experiments were performed in which the probe was placed on the phantom 30 times. For 25 mm source-detector separation, the instrument has achieved; 3.5 % standard deviation over mean for intensity and 0.64° standard deviation for phase, while for 35 mm source-detector separation, the performance was; 3.3 % standard deviation over mean for intensity and 0.77° standard deviation for phase.

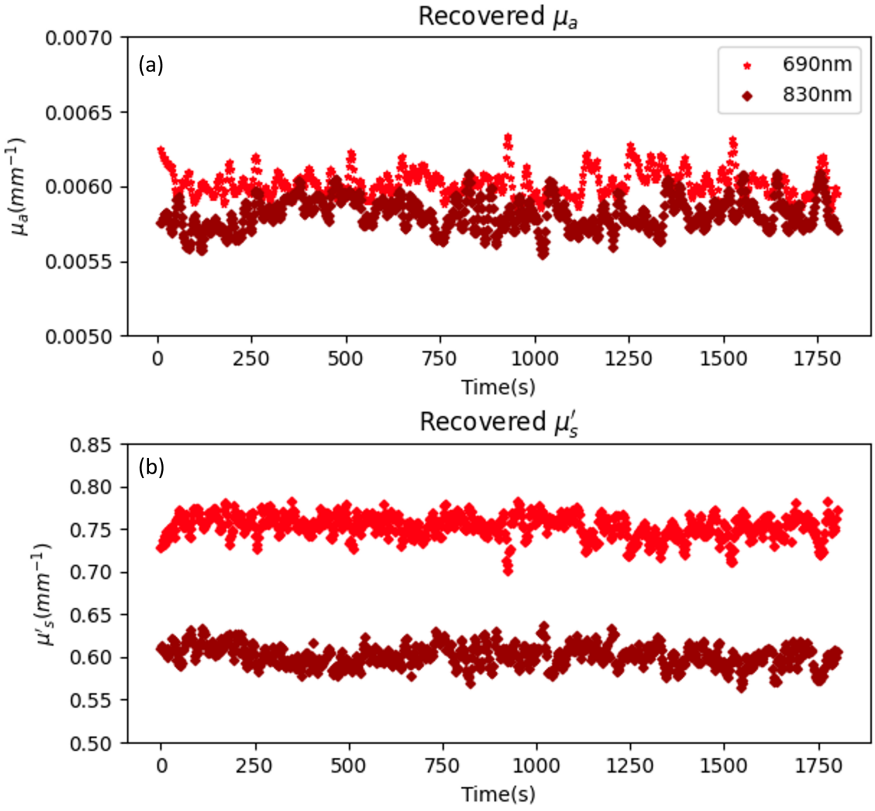

Figure 5-4: (a) Measured absorption coefficient (μ_a) and (b) reduced scattering coefficient (μ_s') during a half-hour phantom experiment.

Similarly, the recovered optical properties from this experiment can be seen in Figure 5-4. In Figure 5-4(a)&(b), the measured μ_a and μ_s' for both wavelengths are presented, respectively. For the recovered optical properties, the standard deviation over mean for μ_a was measured as 0.6% and 0.5% for 830 nm and 690 nm sources, respectively. For μ_s', this relative error was measured as 1% and 0.8% for 830 nm and 690 nm, respectively.

The stability and drift performance of the intensity and phase to the ISS Imagent V2 instrument were also compared. In terms of stability metrics mentioned above, Imagent V2 achieved 0.03% and 0.09% standard deviation over mean for intensities for 25 mm and 35 mm source-detector separation respectively, while our instrument had achieved 0.07% and 0.11%. For the phases, Imagent V2 achieved 0.013° and

0.043° standard deviation compared to our 0.069° and 0.082° for 25 mm and 35 mm separations respectively. The drift in intensity for Imagent V2 was measured as 2.3% for 25 mm and 1.6% for 35 mm source-detector separations over a duration of 10 minutes. This instrument has achieved 1.2% drift for 25 mm and 0.9% for 35 mm source-detector separations. For the phase drifts, Imagent V2's performance was 0.06° for 25 mm and 0.04° for 35 mm source-detector separation. This instrument achieved 0.02° for 25 mm and 0.04° for 35 mm source-detector separation. Even though the instrument could match or surpass the Imagent V2 in terms of drift performance, these results show that there is still room for improvement for stability.

5.2.2 Vascular occlusion experiment

After characterizing the instrument on a solid phantom and verifying its capabilities, an *in-vivo* vascular occlusion experiment was conducted on a healthy, 30 years old, male human subject in accordance with the Tufts University HS IRB. In this experiment, an inflatable cuff was placed on the left upper arm. An inflated cuff pressure of 80 mmHg was applied, which is below the arterial pressure but above the venous pressure to induce venous occlusion. Radiant exposure to the skin was calculated to be 97 $\mathrm{mJ\,cm^{-2}}$, which is well within the requirements of the ANSI Z136.1 laser safety standards [5]. The experimental procedure was as follows:

- The subject was seated on a chair with their left lower arm placed on a table, under the DS probe.
- The DS probe was positioned on the *brachioradialis* muscle and an inflatable cuff was wrapped around the left upper arm.
- 5 min of baseline optical data were collected.
- The cuff was inflated to 80 mmHg and 3 min of occlusion data was collected.
- The cuff was deflated and 2 min of recovery data was collected.

When the cuff is inflated, it is expected to occlude only the veins and not the arteries. Therefore, blood can enter the lower arm in an oxygen-rich state through the

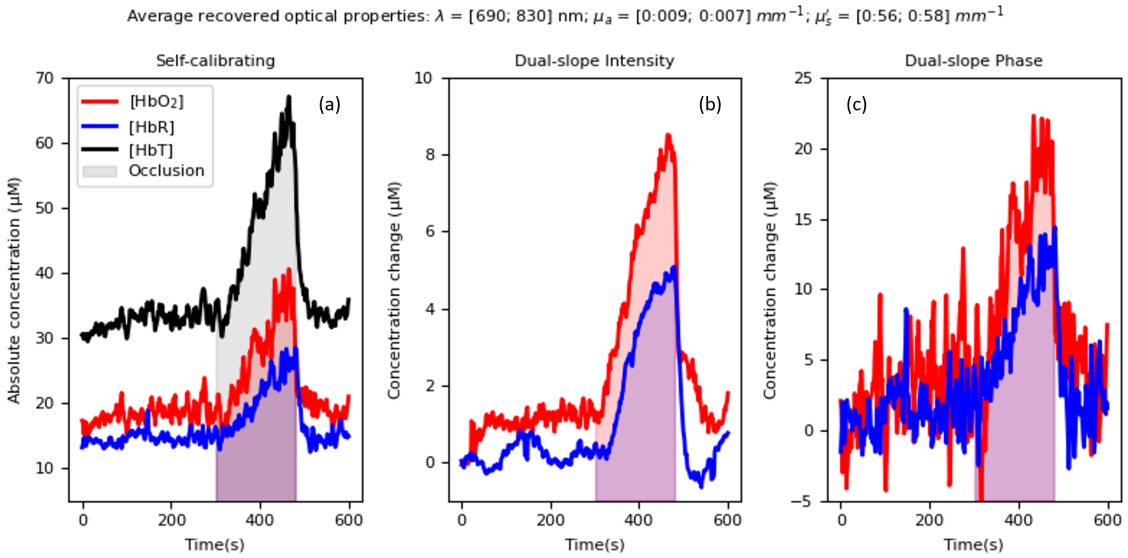

Figure 5-5: HbO_2, HbR, and HbT concentrations during venous occlusion indicated by the shaded area. (a) Self-calibrating (SC) recovered absolute concentrations (see Figure 5-6 (a)). (b) Dual-slope intensity (DSI) recovered concentration change. (c) Dual-slope phase (DSϕ) recovered concentration change.

unobstructed artery, yet it cannot leave the lower arm through the occluded veins. As a result, we expect to see a rise in both [HbO_2] and [HbR] in the lower arm as blood volume increased [77].

In Figure 5-5, the measured [HbO_2] and [HbR], as well as their summation, total hemoglobin concentration ([HbT]; for absolute measurement with SC), are presented. The occlusion interval is indicated by the shaded region. It can be seen in Figure 5-5 that during baseline (first 300 s) hemoglobin concentrations do not increase or decrease. When occlusion begins, both [HbO_2] and [HbR] rise steadily until the cuff is released at 480 s, after which point hemoglobin levels return to their baseline levels. The baseline level of tissue oxygen saturation (StO_2) level was measured as 60%, which is consistent with previously reported values for the human forearm [78]. Figure 5-5 shows three versions of these traces in three panels: the left panel shows the absolute concentrations recovered by SC [52], the center panel shows the change in concentration recovered by DSI [58, 59], and the right panel shows the change in concentration recovered by DSϕ [58, 59]. The differences between the [HbO_2] and [HbR] traces recovered by DSI or DSϕ result from the sensitivity of the data types

to different regions within the tissue [57, 79]. The SC recovered traces, on the other hand, are a combination of both I and ϕ data and allow μ_s' to vary with time (Figure 5-6) while DS methods fix μ_s' (Section 2.4) [58]. Assuming μ_s' is fixed at a baseline value (as with DS methods) is more representative of the physiological reality, and the changes in the bottom panel of Figure 5-6 (recovered by SC) are most likely an artifact resulting from the crosstalk between absorption and scattering. Venous occlusion causes a large change in μ_a that may not be spatially homogeneous within the investigated tissue volume.

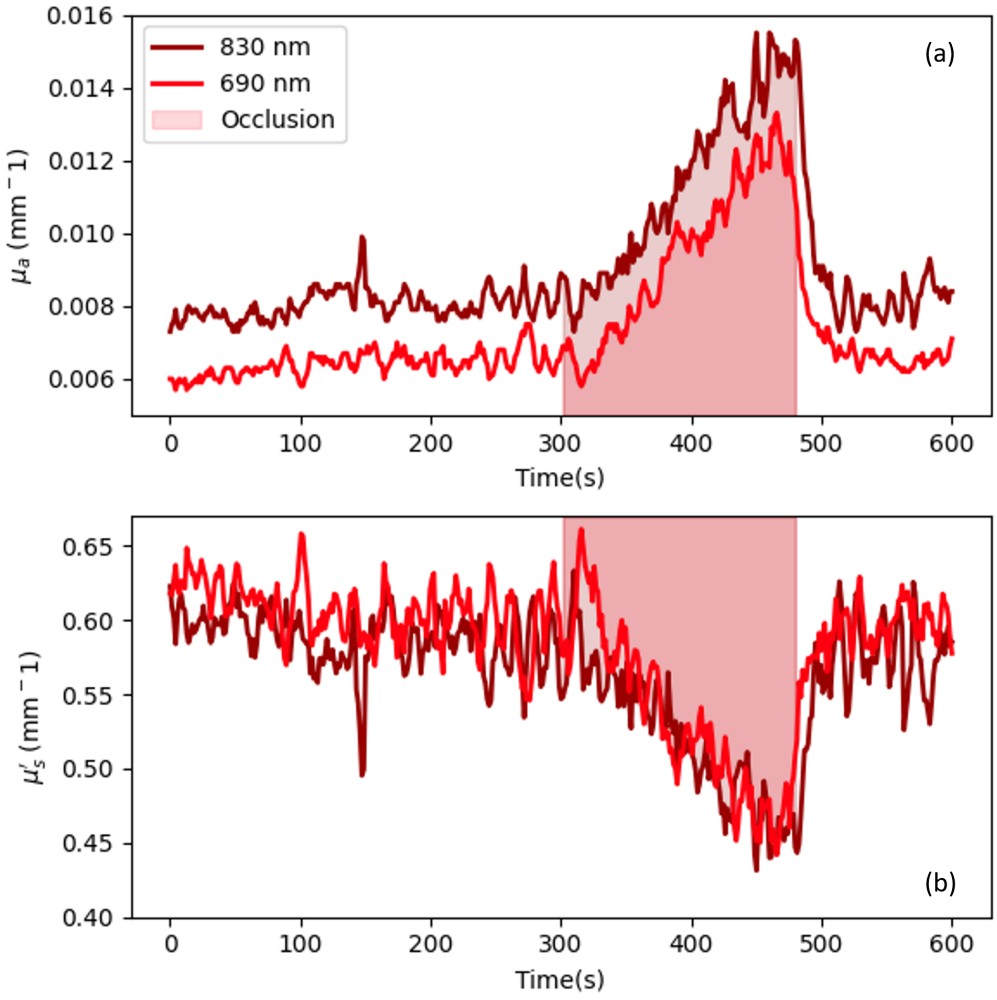

Figure 5-6: Self-calibrating (SC) recovered absorption coefficient (μ_a; (a)) and reduced scattering coefficient (μ_s'; (b)) during venous occlusion indicated by the shaded area.

Even a purely absorption change may result in an apparent scattering change as a

result of cross-talk between the measured absorption and the scattering changes [80], because during analysis the absorption change is treated as spatially homogeneous. Although an increase in red blood cell concentration can result in greater optical scattering in tissue, the large scattering change ($\sim 20\%$) and its direction (decrease) observed in the experiment during venous occlusion are assigned to model-based crosstalk between measured absorption and scattering changes.

5.3 Discussion

This implementation represents a substantial advancement over earlier iterations in three key areas. First, compact read-out solutions were adopted, replacing bulky National Instruments data acquisition hardware with an STM32G491 microcontroller, thereby removing a major barrier to the long-term goal of wearable deployment. Second, compatibility with DS and SC methods was incorporated, eliminating the need for pre-calibration in absolute measurements. Finally, the overall size of the system was significantly reduced. Together, these improvements make the instrument promising for both research and clinical applications.

Rigorous performance testing was initially conducted using solid phantoms to evaluate stability and noise characteristics. During a 30 min phantom experiment, phase noise of 0.08° and intensity variation of 0.11 % (standard deviation over mean) were measured at a source–detector distance of 35 mm. These measurements corresponded to the precisions of 0.5 % and 0.9 % for the absorption and reduced scattering coefficients, respectively. The drift and stability were compared to the ISS Imagent V2 system, with comparable or superior performance observed in both intensity and phase across 25 mm and 35 mm separations, although further improvements in stability remain desirable. These results demonstrated that the system is suitable for human testing and confirmed the effectiveness of SC/DS analysis in mitigating systematic errors induced by thermal drifts and other instrumental or environmental factors.

The capability of the instrument to measure hemodynamic changes was subsequently verified through an *in-vivo* vascular occlusion experiment on a healthy subject.

During a protocol consisting of five minutes of baseline, three minutes of venous occlusion, and two minutes of recovery, absolute concentrations of HbO_2 and HbR were observed to increase steadily during occlusion and return to baseline upon release. Dual-slope analysis performed separately on intensity and phase data highlighted differences attributable to their differing tissue sensitivities.

Several limitations and opportunities for improvement were identified. The current acquisition rate remains lower than that of comparable instruments reported in the literature; however, this limitation is primarily attributed to the serial communication bottleneck between the Raspberry Pi 4 and the STM32G491 microcontroller and is expected to be addressable through software optimization. The modulation frequency was restricted to 55 MHz by the -3 dB bandwidth of the ASIC, despite the signal generator's capability of up to 250 MHz. Since higher modulation frequencies improve phase contrast [81], operation in the 100-150 MHz range would be preferable, provided that the increased bandwidth does not compromise the signal-to-noise ratio. Furthermore, to accommodate for longer and shorter source-detector separations at the same time, a scheme allowing for larger dynamic range would be beneficial.

The next major milestone in this effort will be the design and tape-out of a new ASIC generation. This would feature improved bandwidth (> 100 MHz), a lower noise transimpedance amplifier, and, most importantly, phase and amplitude readouts. Upon success, a subsequent iteration of the instrument could be reduced to only the optics, DDS, a microcontroller, and the ASIC, enabling the realization of a wearable form factor.

Chapter 6

Generation 2 FD-NIRS ASIC: Fully integrated laser driver and readout

Right. One... two... five!

King Arthur, Monty Python and the Holy Grail

So far in this thesis, the overall architecture, design trade-offs, and performance of 3 separate generations of FD-NIRS instruments have been presented in detail. Each iteration of the instrument showed further miniaturization and integration, but each still relied on multiple discrete components and therefore remained limited in portability, scalability, and suitability for wearable use. The two common components in all of these instruments were the FD-NIRS ASIC Generation 1, which has been the core of these instruments, and the DDS. In order to reach the ultimate goal of advancing FD-NIRS technology to a wearable form factor, the obvious candidate for the next breakthrough is a new generation of FD-NIRS ASIC, where not only the AFE but as many components as possible are integrated.

The design described here addresses these limitations by advancing toward a highly integrated implementation, in which core functions such as amplitude and phase readout, and laser driving are also integrated within a single IC, on top of the existing analog front-end, leaving only the signal generation and digitization off-chip. This integration effort marks the next step towards the realization of a compact, low-power

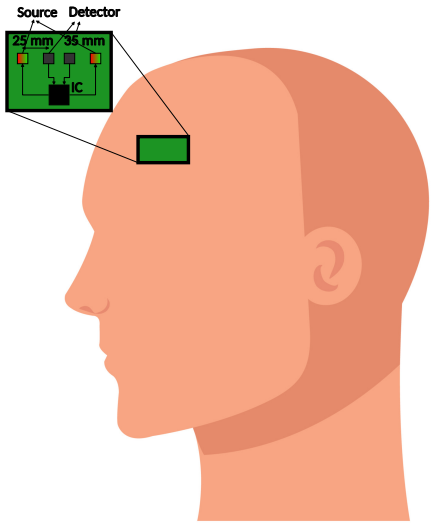

Figure 6-1: An example of sensor placement for brain neural measurements

and ultimately wearable FD-NIRS device, approaching the envisioned form factor shown in Figure 6-1.

In the next section, the overall proposed system architecture will be introduced, along with some preliminary performance calculations for the new AFE, such as the sensitivity and noise limit, dynamic range, etc. Section 6.2 presents the design process of the new AFE, followed by Section 6.3, which details the amplitude detector. Section 6.4 then describes the phase detector, and finally, Section 6.5 discusses the laser driver in detail.

6.1 System Requirements and Design

Before starting to design this FD-NIRS system, it is a good idea to analyze the key performance parameters. The optical components that were used until this point have been working well enough, so there is not a good reason to design for alternative and unproven components. Therefore, the photodetector that this instrument will be designed to work with is S9251-15, from Hamamatsu.

In order to start designing a new analog front-end that will interface with this APD, the noise limit of the APD should be quantified. The specifications and details

of this APD were already listed in Section 3.1.1.2 but will be repeated here for the sake of analysis. The spectral response of this photodetector ranges between 400 nm and 900 nm, and peaks at 860 nm. The photosensitivity is 0.52 A/W, with an avalanche gain of 100, the breakdown voltage is −250 V and the −3 dB bandwidth is 350 MHz [63]. As most things in life, there is no free lunch. These excellent performance metrics of this APD come with trade-offs, in the shape of 3.6 pF junction capacitance and 0.8 nA dark current. Using these metrics, one can estimate the optical noise floor of this APD as follows;

$$\begin{aligned} P_{min} &= \frac{i_{dark}}{Responsivity} = \frac{0.8\,\text{nA}}{0.52\,\text{A/W}} = 1.5\,\text{nW} \\ I_{min} &= P_{min} * M = 115\,\text{nA} \end{aligned} \tag{6.1}$$

The circuit that will interface with this APD should have a noise floor lower than this to maximize the overall noise performance.

Another very important challenge for any FD-NIRS system is the dynamic range requirement. The power of the optical signal can easily change as much as 20 times between a short source-detector separation and a longer one. Therefore, the signal chain through which these signals will pass, the AFE and the subsequent heterodyne down-converter, should have at least a dynamic range of 32 dB.

Toward the goal of integrating as many discrete components as possible, laser the driver and the phase and amplitude read-out circuits are also integrated. During phase measurements, an error of 1° can result in an error of $\sim 6.5\,\%$ in μ_a and $\mu_s\prime$ [47]. Hence, the phase resolution target is chosen as 0.02°. Similarly, the amplitude read-out circuit should be able to perform accurately throughout the dynamic range. An error of 5 % in amplitude due to insufficient dynamic range and hence gain compression, can result in an error of 3 % in μ_a and $\mu_s\prime$ [47].

Finally, the laser driver circuit should be able to modulate the target light sources. The target light sources for this system are again HL6750MG and HL8338MG from Thorlabs. These are 3-pin C-configuration laser diodes with 50 mW optical power. The operating forward current they require is ∼70 mA. Therefore, the laser driver

circuit should be able to handle at least 100 mA, to account for transient current spikes that may occur due to switching from one laser diode to the other. These laser diodes also have an integrated photodetector that senses the optical output of the laser diode and generates a small monitoring current proportional to it. The laser driver circuit will take advantage of this monitoring current in order to regulate the optical output of the laser diodes.

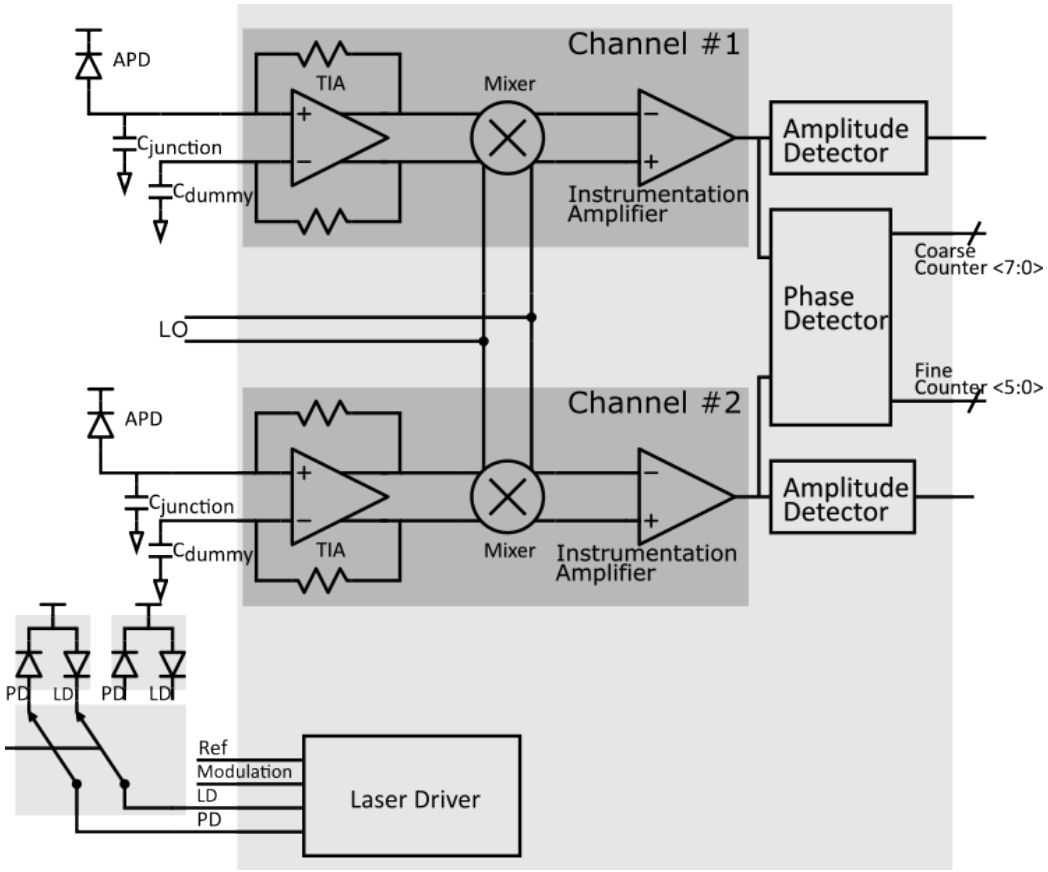

Figure 6-2: The proposed system block diagram for Generation 2 FD-NIRS ASIC.

The proposed system block diagram can be seen in Figure 6-2. There are two identical signal channels (Channel #1 and Channel #2 in Figure 6-2), with their own AFEs and Amplitude Detectors, and they share the Phase Detector. Each channel will interface with one S9251-15 APD, amplify its output, and perform heterodyned down-conversion. The amplitude detectors will measure the heterodyne down-converted, low-frequency signals. The shared phase detector will measure the phase difference between the two low-frequency signals. The Phase Detector has two sets of output,

an 8-bit set for the coarse counter and a 6-bit set for the Fine Counter. The output of the Amplitude Detectors is in the analog domain and need to be digitized by an external ADC.

Additionally, there is a Laser Driver circuit that will modulate the light sources. The laser driver's output will be in open-drain form, where one laser diode can be connected. Alternatively, a switching IC such as ADG1412 can be connected to this open-drain output in order to be able drive multiple laser diodes with this laser driver.

In the following chapters, the design details and simulation results of these circuits will be presented. In Section 6.2, the design of the transimpedance amplifier will first be discussed starting with a review of various possible topologies. Then the heterodyned down-conversion will be examined.

6.2 Analog Front End

In a noise-conscience system with multiple stages of amplification and signal conditioning, analyzing noise and investigating the most important noise contributors is very difficult. The Friis' formula (Equation 6.2) for the noise figure simplifies this process significantly, more importantly, provides insight about where to put the most effort:

$$F_{total} = F_1 + \frac{F_2 - 1}{G_1 G_2} + \frac{F_3 - 1}{G_1 G_2 G_3} + ... \frac{F_N - 1}{G_1 G_2 ... G_{N-1}} \tag{6.2}$$

where F_k is the noise figure of the k^{th} stage and G_k is the gain of the k^{th} stage. It is apparent from Equation 6.2, that the very first stage is the most important one for noise performance: Its noise contribution F_1 is not divided by any of the gains in the later stages, and its gain G_1 mitigates the noise contributions of every stage after it. Thus, the noise performance of the first stage is crucial. Another crucial performance metric for this application is the dynamic range, because the optical power recovered from the short source-detector separation can be ~ 20 times greater than the long one. The important distinction between the dynamic range requirement and noise requirement from a system design point of view is that the dynamic range

of a system is as high as its weakest link, whereas only the noise performance of an earlier stage is significantly more important than that of a later one. This means that not only the TIA, but also the Mixer must have a large dynamic range. In addition, the read-out scheme must be able to function throughout the entire dynamic range. Different topologies for each AFE part will be discussed in the relevant sections.

6.2.1 Transimpedance Amplifier

There are several popular topologies for TIA to be considered; such as capacitive feedback [82], resistive feedback, and logarithmic transimpedance amplifier [83].

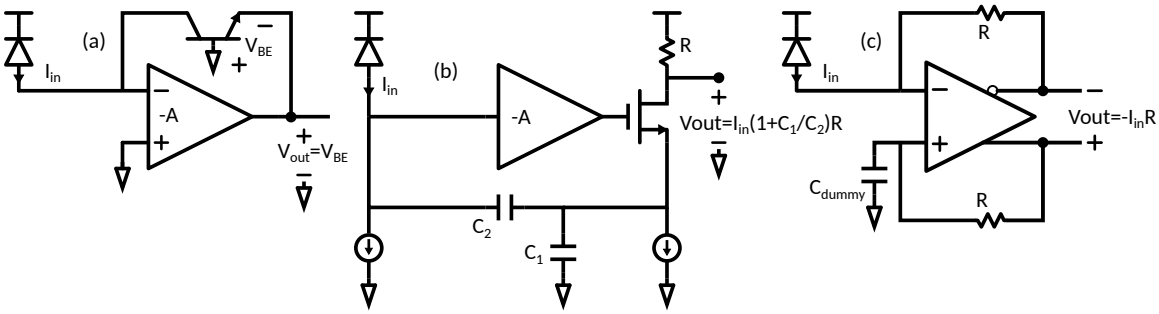

Figure 6-3: Schematics of (a) Logarithmic and (b) Capacitive Feedback TIAs

Logarithmic transimpedance amplifiers (Figure 6-3(a)) take advantage of the relationship between the collector current and the base-to-emitter voltage of a BJT. Assuming a forward active region for a BJT, this relationship can be expressed as Equation 6.3, where I_C is the collector current, I_S is the process-dependent saturation current, V_{BE} is the base emitter voltage, k is the Boltzmann constant, T is the ambient temperature and q is the fundamental charge.

$$I_C = I_S * (e^{\frac{V_{BE}}{kT/q}} - 1) \tag{6.3}$$

From 6.3, it can be seen that there is an exponential relationship between I_C and V_{BE}. This relationship can be inverted to achieve a logarithmic one. Due to this logarithmic relationship, it becomes trivial to achieve ∼60 dB dynamic range, with a logarithmic transimpedance amplifier. However, there is also a big downside; the small signal

transconductance, g_m, of a BJT depends on I_C (Equation 6.4).

$$g_m = \frac{I_C}{kT/q} \tag{6.4}$$

This reality represents two very important issues. The bandwidth and noise performance of the logarithmic transimpedance amplifier become a function of I_C. Another way to put this is that the smaller the input signal, the lower the bandwidth and worse the noise performance. For large enough signal strength, this reality might not pose a significant problem, but an FD-NIRS instrument will have to interface signals that are quite close to the noise floor. The strength of the logarithmic transimpedance amplifier becomes arguably its weakness.

$$V_{out} = \frac{1}{C}\int_0^T I_{in}(t)dt \tag{6.5}$$

Capacitive feedback TIAs (Figure 6-3(b)) are a quite suitable option for high-bandwidth and low-noise TIA applications. However, they tend to suffer from saturation problems. This saturation problem arises when the input current I_{in} has some non-zero DC component. Considering the I-V characteristic of a capacitor (Equation 6.5), one can see how the capacitor in the feedback path causes the amplifier to integrate I_{in} and

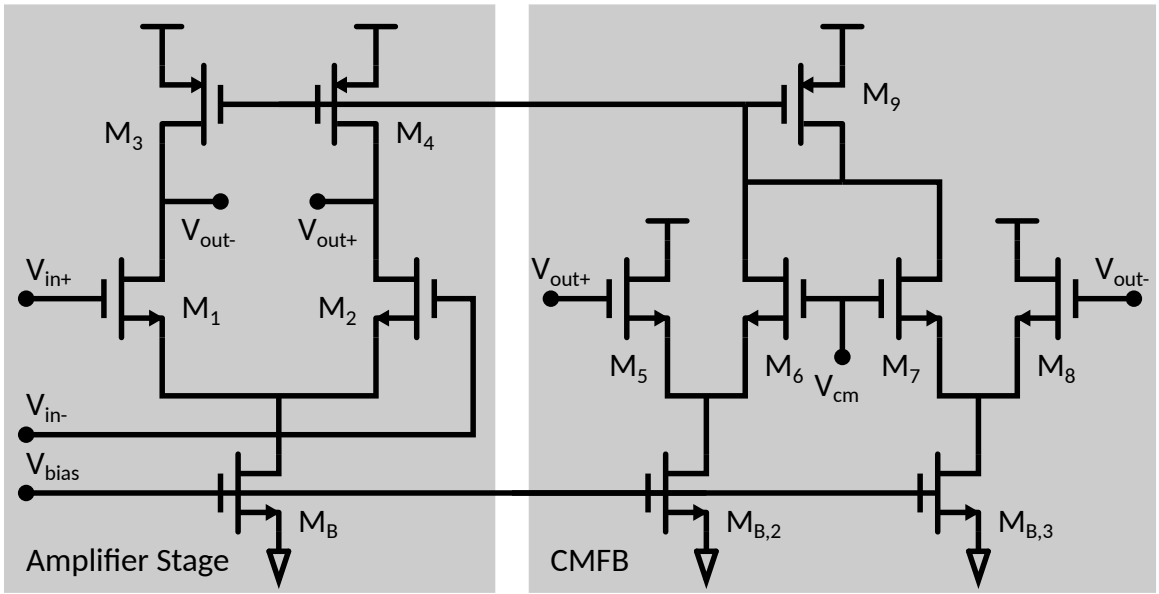

Figure 6-4: Schematic of one of section the sections of the core amplifier

eventually causes the amplifier to saturate. To resolve this issue, either a mechanism to reset the output of the TIA or an additional feedback mechanism to perfectly cancel the DC component of I_{in} is needed. Furthermore, capacitive feedback TIAs are unsuitable to be designed in a fully-differential manner. Considering all of these pros and cons for different topologies, the TIA was designed as a fully-differential resistive-feedback TIA. The schematic of this topology can be seen in Figure 6-3(c).

The core amplifier of the TIA was distributed into 3 separate amplifiers to extend the bandwidth of the overall amplifier. One section of the core amplifiers can be seen in Figure 6-4. Each amplifier section is a simple fully differential amplifier with active loads. Since it is fully differential with active loads, common-mode feedback (CMFB) is needed to stop the amplifier's outputs from hitting either rail. The CMFB circuit is designed as a scaled down replica of the amplifier part, e.g. $(\frac{W}{L})_{M_B} = 80 * (\frac{W}{L})_{M_{B2}}$ and $(\frac{W}{L})_{M_3} = 80 * (\frac{W}{L})_{M_{B9}}$. In this way, the CMFB can keep the output common mode $V_{out_{cm}} = [V_{out+} + V_{out-}]/2$ equal to V_{cm}, with minimal current consumption.

The noise model of the proposed TIA should be examined first, before moving forward with the design. A simplified noise model of resistive feedback TIA can be seen in Figure 6-5. The first step is the thermal noise current contribution of the

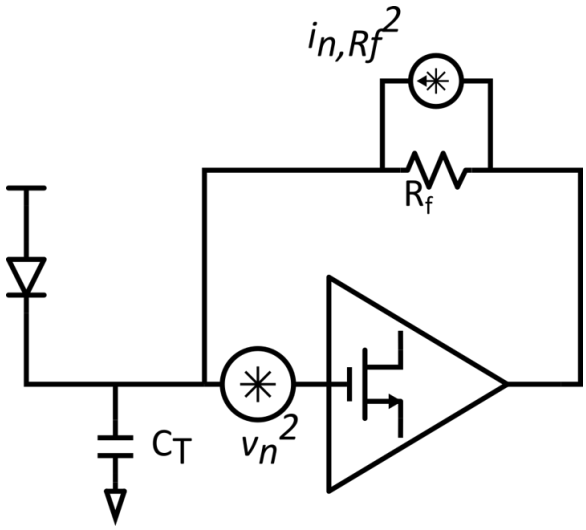

Figure 6-5: Simplified noise model for a resistive feedback TIA

feedback resistor, which can be modeled as;

$$i_{n,R_f}^2 = \frac{4kT}{R_f} \tag{6.6}$$

where k is the Boltzmann constant and T is the ambient temperature. The next step is the contribution of the amplifier. The voltage noise source of the amplifier appears across the total capacitance C_T at the inverting input. Therefore, one can define a noise current that flows through the capacitor;

$$i_{n,v_n}^2 = \frac{v_n^2}{|Z_C|^2} = (\omega C_T)^2 v_n^2 \tag{6.7}$$

where v_n^2 is the input-referred noise voltage of the amplifier. Combining Equation 6.6 and Equation 6.7, we get;

$$i_{n_in}^2(\omega) = \frac{4kT}{R_f} + (\omega C_T)^2 v_n^2 \tag{6.8}$$

The next step is to relate the amplifier noise v_n^2 to the transistor parameters. Equation 6.2 can be used to simplify the analysis once more. As such, only the noise contribution of the first stage will be considered, because there are 3 cascaded stages, and the noise contribution of the next stages will be divided by the combined gains of the previous stages.

Inspecting Figure 6-4, one can observe that the noise contribution of the amplifier considered in Equations 6.7 and 6.8 was, in fact, the noise contribution of the input transistors M_1 and M_2. The input referred noise voltage of a MOSFET can be modeled as;

$$v_n^2 = \frac{4kT\gamma}{g_m} \tag{6.9}$$

where γ is a process-dependent variable, usually $0.7 - 3$ for MOSFET. Substituting Equation 6.9 into Equation 6.7, and combining Equation 6.7 with Equation 6.6, the

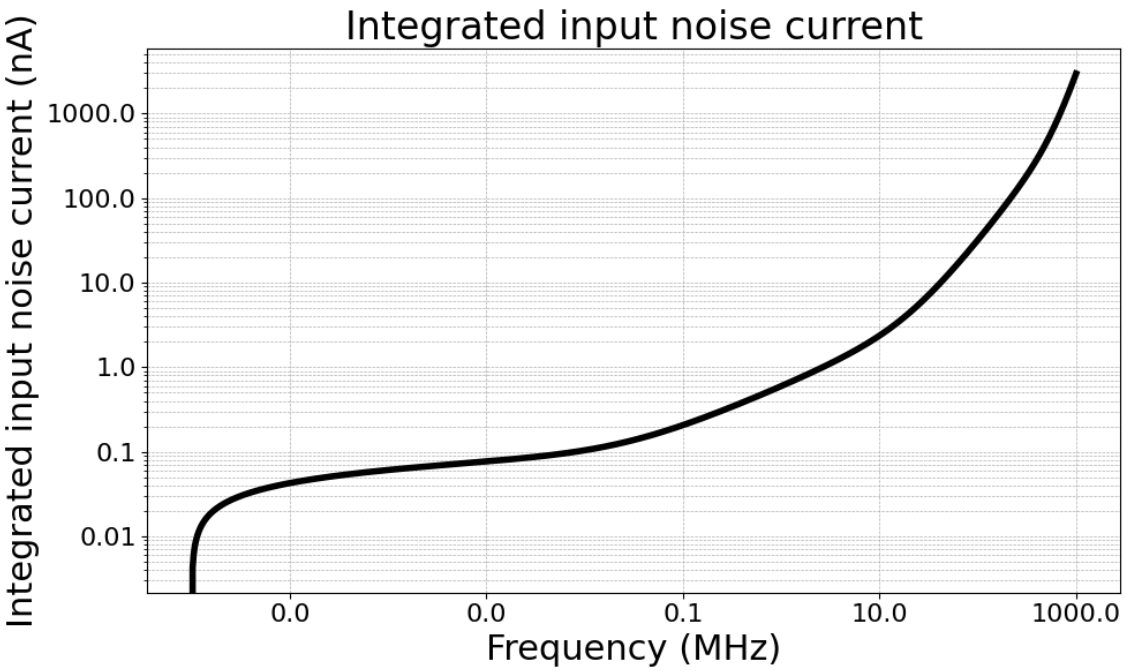

Figure 6-6: Input referred integrated noise current of the TIA versus frequency

total input-referred noise of the resistive feedback TIA can be approximated as;

$$i_{n,TIA}(\omega)^2 = \frac{4kT}{R_f} + (\omega C_T)^2 \frac{4kT\gamma}{g_m} \tag{6.10}$$

This equation suggests that in order to reduce noise, one should increase R_f or increase g_m. The former not only reduces noise but also increases the gain of the TIA which further reduces the overall noise of the analog front-end; however, larger R_f also means reduced bandwidth. The latter means higher power consumption and larger transistors. It is important to note that larger transistors also mean increased C_T and higher noise, so there is a limit to it. Taking all of these trade-offs into account, the design was finalized with $R_f = 100k\Omega$ and $g_m = 10\,\text{mS}$. In order to achieve 10 mS transconductance, the first stage was designed to consume 1 mA current. This reduces to 0.75 mA in the second stage and 0.5 mA in the third stage, all under the supply voltage 1.8 V. Overall, the TIA was designed to consume 4.1 mW power, has a transimpedance gain of 100 dB with 147 MHz 3-dB bandwidth, and only 30 nA_{rms} integrated input-referred noise current (Figure 6-6). A high bandwidth allows freedom

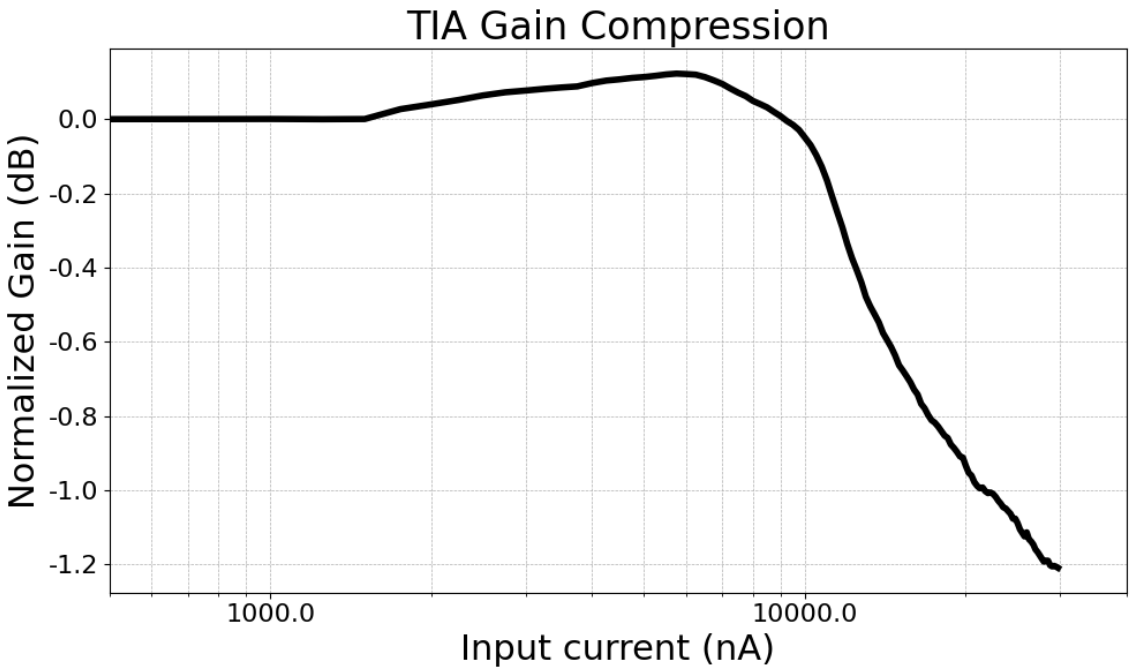

Figure 6-7: Input referred 1 dB gain compression performance of the TIA

in selecting modulation frequencies after tape-out. Furthermore, the TIA also has a input-referred 1-dB gain compression at 21.5 µA input current (Figure 6-7), which results in 57 dB dynamic range.

6.2.2 Mixer

As mentioned, the readout strategy for this generation of ASIC was chosen to be heterodyned down-conversion, and this requires a mixer circuit. It is possible to divide the mixer topologies into two; passive mixers and active mixers. Passive mixers, as the name implies, are built with passive components and do not provide any conversion gain, but are simpler to implement. For example, a ring-diode mixer consists of only 4 diodes, but they suffer from conversion loss, higher noise, and they require transformers to work. Although they are very popular as discrete components, they are not easy to integrate (due to transformers), thus not suitable for this application. Active mixers on the other hand, are very popular in integrated circuits since they are mainly constructed with transistors. Additionally, active mixers offer a certain range of conversion gain control through the LO power, whereas the parameters of passive

mixers cannot be controlled after tape-out. Therefore, in this design, the topology of the mixer was chosen among the active mixers.

As mentioned in Section 6.2.1, the design of the TIA stage was optimized for noise performance, while maintaining the high enough bandwidth and transimpedance gain of 100 dB. However, for the Mixer design, the design is focused on the dynamic range, since the signal levels can fluctuate ~ 20 times between short and long source-detector separation. Keeping the active mixer considerations and the focus on the dynamic range performance, the topology selected for the mixer design is the Double Balanced Gilbert Mixer with folded input pairs and source degeneration resistors, and the schematic can be seen in Figure 6-8. The double balanced Gilbert Mixer provides inherent even harmonic cancellation for improved linearity, and the folded input pair combined with source degeneration resistors provides even further linearity. Additionally, the supply voltage V_{DD} for the mixer and all the subsequent circuits from now on operates under 3.3 V. The mixer was designed with passive loads R_L instead of active loads similar to the TIA due to simplicity, because there would be a need for a complex CMFB circuit since the design is fully-differential.

In Figure 6-8, the matched transistors M_1 and M_2 convert the differential input signal $V_{RF} = V_{rf}cos(\omega_{rf}t)$ into differential current and route it to the second branch, where the current steering with the differential LO signal V_{LO} is done by M_{3-6} to achieve frequency mixing. The transconductance of the first stage can be represented as;

$$G_m = \frac{1}{1 + g_m/R_s} \approx 1/R_s \tag{6.11}$$

Defining V_{LO} as a square wave, it can be expanded into an infinite series using Fourier transform;

$$V_{LO} = \frac{4}{\pi}[cos(\omega_{lo}t - \frac{cos(3\omega_{lo}t)}{3} + \frac{cos(5\omega_{lo})}{5}...] \tag{6.12}$$

$$V(t) = V_{RF} * V_{LO} \tag{6.13}$$

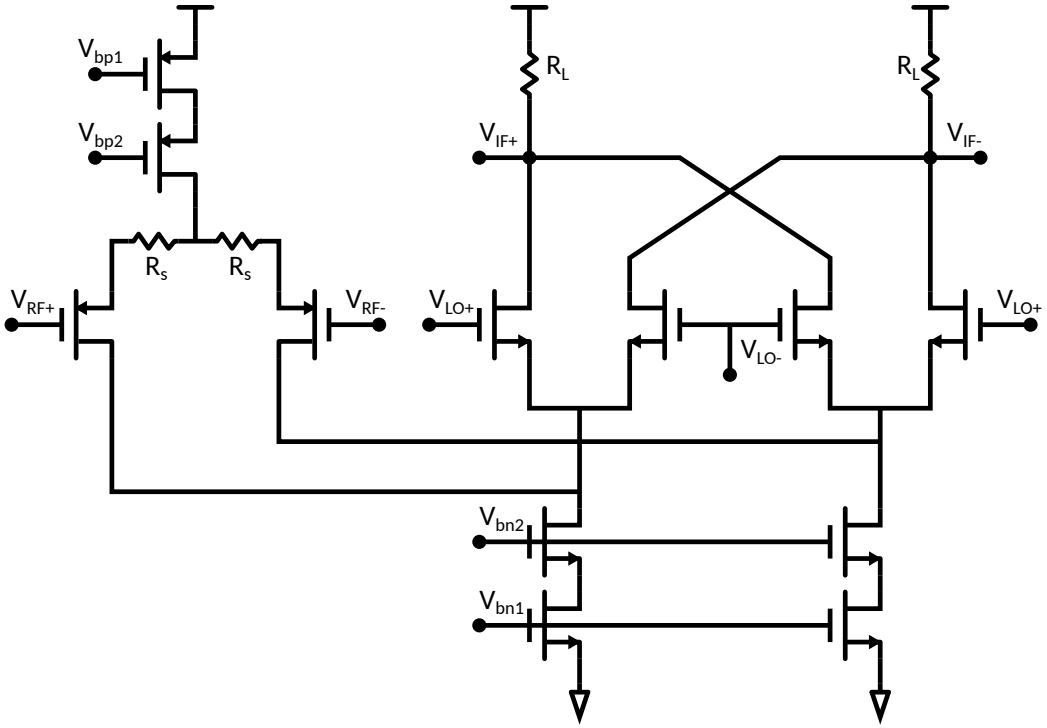

Figure 6-8: Schematic of the Double Balanced Gilbert Mixer with folded input pair

$$\begin{aligned} V_{mix}(t) = &\frac{2V_{rf}}{\pi}[cos(\omega_- t) - \frac{cos(\omega_{3-} t)}{3} + \frac{cos(\omega_{5-} t)}{5}...] + \\ &\frac{2V_{rf}}{\pi}[cos(\omega_+ t) - \frac{cos(\omega_{3+} t)}{3} + \frac{cos(\omega_{5+} t)}{5}...] \end{aligned} \tag{6.14}$$

where

$$\begin{aligned} \omega_+ &= \omega_{lo} + \omega_{rf} \qquad \omega_- = |\omega_{lo} - \omega_{rf}| \\ \omega_{3+} &= 3\omega_{lo} + \omega_{rf} \quad \omega_{3-} = |3\omega_{lo} - \omega_{rf}| \\ \omega_{5+} &= 5\omega_{lo} + \omega_{rf} \quad \omega_{5-} = |5\omega_{lo} - \omega_{rf}| \\ &\cdot \qquad\qquad\qquad \cdot \\ &\cdot \qquad\qquad\qquad \cdot \\ &\cdot \qquad\qquad\qquad \cdot \end{aligned} \tag{6.15}$$

Equations 6.14 and 6.15 show that $V_{mix}(t)$ contains the heterodyne down-converted IF signal $V_{IF} = \frac{2V_{rf}}{\pi} cos(\omega_- t)$, the up-converted signal $V_{up} = \frac{2V_{rf}}{\pi} cos(\omega_+ t)$ as well as odd numbered harmonics with $\omega_{3+}, \omega_{3-}, \omega_{5+}, \omega_{5-}$ terms. Notably, even harmonics are missing, due to the balanced nature of this topology. The conversion gain provided by the mixer versus the LO power can be seen in Figure 6-9. The gain peaks at 14 dB at

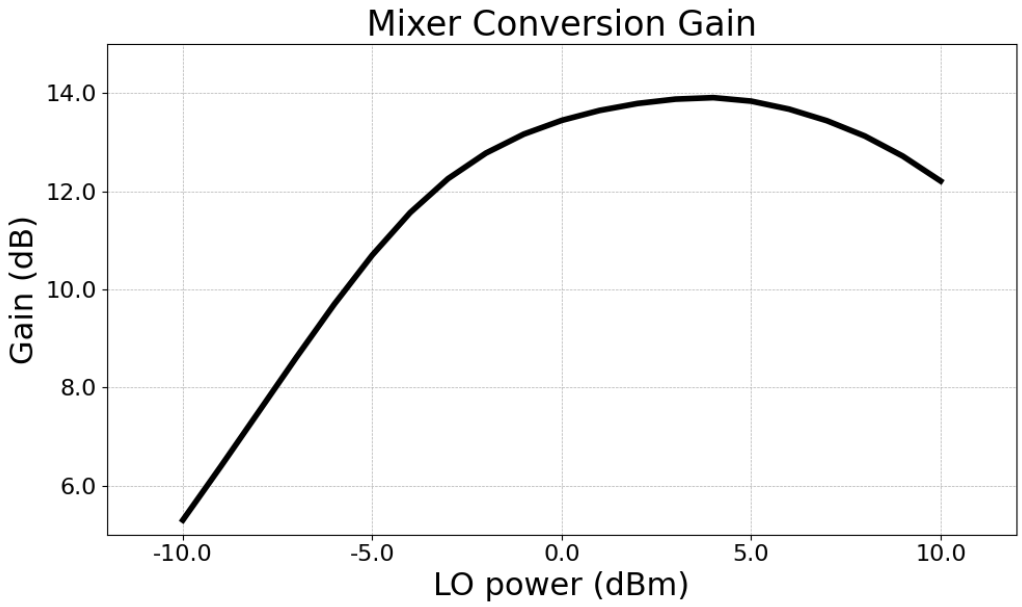

Figure 6-9: Conversion gain vs LO power

$\sim$4 dBm, or 1 V LO. This figure also presents a way to control the conversion gain between 5 and 14 dB, by adjusting the LO power between -10 and 4 dBm.

Figure 6-10 shows the gain compression performance of the mixer. The mixer shows -1 dB conversion gain compression at ~ -5.5 dBm or 340 mV input RF power. Dividing this RF power by the TIA gain corresponds to $\sim$3.4 µA of the photodetector current. This value is significantly smaller than the maximum photodetector current the TIA can amplify without compression, therefore, the factor limiting the dynamic range of the Analog Front-end is the mixer. Considering the noise floor of the TIA is 30 nA and the mixer's gain compression at $\sim$3.4 µA photodetector current, the worst case AFE dynamic range is $DR = 20 * log_{10}(\frac{3.4\,\mu A}{30\,nA}) = 41$ dB. This dynamic range can be extended by 9 dB to 50 dB by reducing the conversion gain of the mixer per Figure 6-9. Overall, the mixer consumes 1.1 mA current under 3.3 V supply, which is $\sim$3.63 mV.

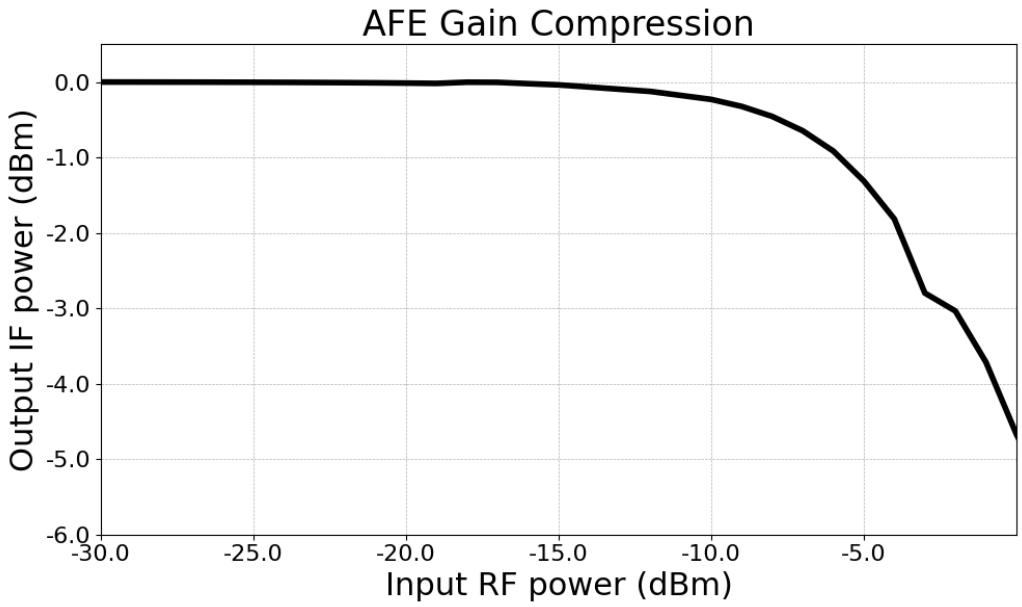

Figure 6-10: Input referred 1 dB gain compression performance of the mixer

6.3 Amplitude Detector

At its core, the amplitude detector circuit works as a peak detector, and was introduced in [84]. This design improves upon that by managing the leakage currents into the output capacitor and therefore mitigating the drift at the output V_{out}. It consists of an OP-AMP, a cascode current mirror, a capacitor to hold the output voltage, a transistor for resetting the output, and a 2-to-1 MUX. The schematic can be seen in Figure 6-11. Assuming Reset signal to be LOW, with a sine wave at the input (V_{in}), and some initial DC output voltage V_{out} that is lower than V_{in}; as the input voltage increases and goes above V_{out}, the output of the OP-AMP goes low and starts sinking current from the left-hand side of the current mirror, which is then copied to the right-hand side.

Since the Reset signal is LOW at this point, V_{bias} is equal to V_{fb} and the transistor is in cut-off region, and the capacitor is being charged. This continues as long as V_{in} is greater than V_{out} and Reset is LOW. Then, as the input voltage starts to decrease below the output, the OP-AMP stops sinking current, and since there is no current to be copied to the right-hand side, V_{out} stops rising. The output is held at the peak

level. There is an important non-ideality that disrupts V_{out}. Even though there is no current to be copied, the right-hand side of the current mirror is still leaking some current, and this leakage current causes V_{out} to rise slowly over time. In order to mitigate this, the current mirror was implemented as a triple cascode current mirror. This implementation greatly reduced this leakage, but did not eliminate it completely. To balance this leakage current, the gate of the transistor is connected to V_{fb} during Reset is LOW, keeping the transistor in the deep subthreshold region, but not entirely in the cutoff region. The leakage current from the triple cascode mirror was balanced by appropriately sizing the transistor, V_{out} does not drift over time. When the Reset signal becomes HIGH, the transistor discharges the output to V_{cm}.

The operation of the circuit can be seen in Figure 6-12. In this figure, the input current to the AFE was swept from 250 nA to 1 µA, and the transient results of the amplitude detector's output is shown. It can be seen that the amplitude detector circuit successfully follows the input and keeps the peak voltage, until the Reset signal comes, after which the output goes to V_{cm}.

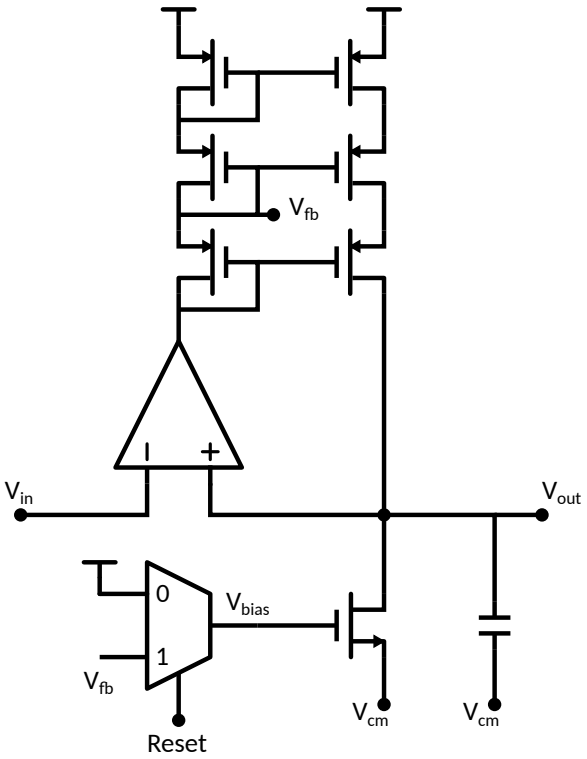

Figure 6-11: Schematic of the Amplitude Detector Circuit

The operating range and the DNL of the circuit are two important metrics. Simply put, if the circuit is ideal and DNL is zero, there is a constant relationship between the change in the input and the change in the output. In other words, $\partial V_{peak}/\partial V_{in}$ is constant across the entire region. The absolute accuracy of the circuit is not a critical metric, since it can be calibrated afterwards, by injecting signals with known input amplitudes and looking at the output. To test these metrics, simulations were done in which the input amplitude was swept from 10 mV to 1.65 V. Note that, since the circuit operates under 3.3 V supply voltage, the common mode voltage V_{cm} is 1.65 V, and when the input amplitude is also 1.65 V, it becomes rail-to-rail. Figure 6-13(a) shows the input signal amplitude versus the measured V_{peak}, and Figure 6-13(b) shows the derivative of the previous plot or the DNL of the circuit, and gives better insight to Figure 6-13(a). Since this is a peak detector circuit, the ideal relationship between V_{peak} and V_{in} is constant and unity. We can see this in Figure 6-13(b) where the circuit deviates from this ideal result by less than 1% from ∼20 mV to ∼1.6 V, which is almost all the way to V_{DD}. An important factor to achieve this result is

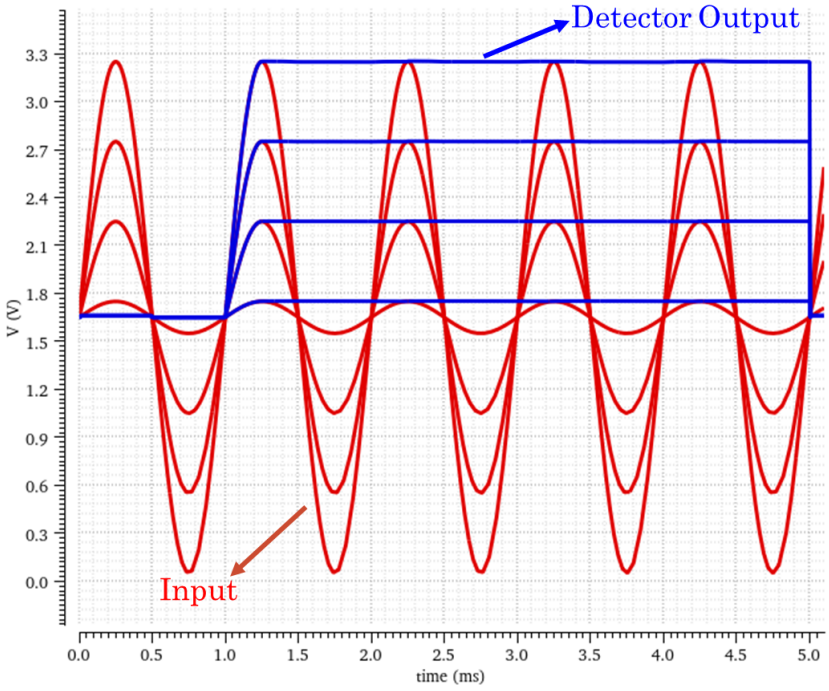

Figure 6-12: Transient results of the Amplitude Detector when the input to the AFE is swept friom 250 nA to 1 mA.

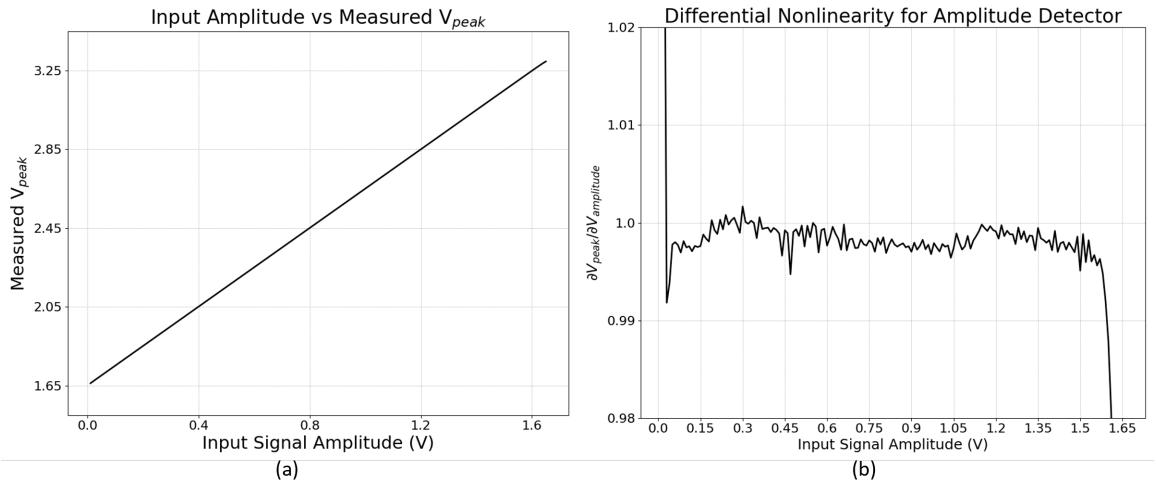

Figure 6-13: (a) Detected V_{peak} with input amplitude swept from 10 mV to 1.65 mV (b) DNL performance of the amplitude detector

the rail-to-rail designed OP-AMP. Figure 6-12 shows the transient simulations of the amplitude detector with input amplitudes ranging from 100 mV to 1.6 V. It shows that the output tracks and rises with the input until input's peak, and then kept at this level until Reset becomes HIGH.

6.4 Phase Detector

Accurate phase measurement of FD-NIRS signals is a very important step for successful FD-NIRS instruments. As mentioned in Chapter 1, using the heterodyne down-conversion method makes it easier to measure the phases of FD-NIRS signals. So far, the phase measurement schemes used were discrete implementations whether with an additional circuit, or using a microcontroller to sample the signals and use FFT algorithms. Integrating the phase detection is an important milestone towards the goal of miniaturizing an FD-NIRS instrument.

The Coarse-Fine Phase Detector circuit that was implemented is based on [84], with improvements to make it work 0°-360°, reducing power consumption and simulation time. The circuit works in two steps; first, the 8-bit Coarse Counter simply counts clock periods. This returns an amount of time that represents the phase difference between the two channels. The block diagram of this architecture can be seen in

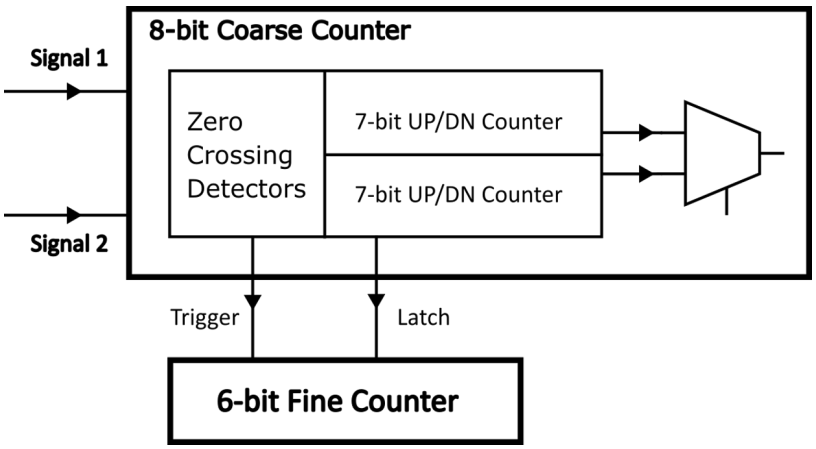

Figure 6-14: The architecture of the Coarse-Fine Phase Detector

6-14. The clock frequency of the Coarse Counter is chosen such that one period of the signals corresponds to 256 Coarse Counter steps. This ensures that the Coarse Counter result is accurate to 1 clock period.

The 6-bit Fine Counter, on the other hand, counts a predetermined and programmable time step in analog fashion, within 1 Coarse Counter clock. This time step is programmed to make sure that 1 Coarse Counter clock corresponds to 64 Fine Counter steps. Working together, this Coarse-Fine Counter approach makes it possible to keep time in the ns scale with only a few MHz external clock frequencies. This approach effectively divides the signal period into $2^6 * 2^8 = 16384$ steps and gives $360°/16384 = 0.022°$ phase resolution. To give an example: assuming that the signal frequency is 10 kHz, or with a period of 0.1 ms, the Coarse Counter clock is set to 2.56 MHz, and the time step for the Fine Counter is set to 6.2 ns. Hence, the entire range of the Coarse Counter spans one signal period, and the entire range of the Fine Counter spans one Coarse Counter clock. This makes sure that the entire range of the Coarse-Fine Counter is used, and the accuracy is maximized.

6.4.1 Coarse Counter

The Coarse Counter was designed as two identical 7-bit Up-Down Counters, that are triggered by the zero-crossing instances of the two signal channels. One counter works when the phase difference between two signal channels is 0°-180°, and stays at 0 when

it is 180°-360°. The other counter works when the phase difference is 180°-360°, and stays at 0 when it is 0°-180°. The zero-crossing instances of the signals are determined

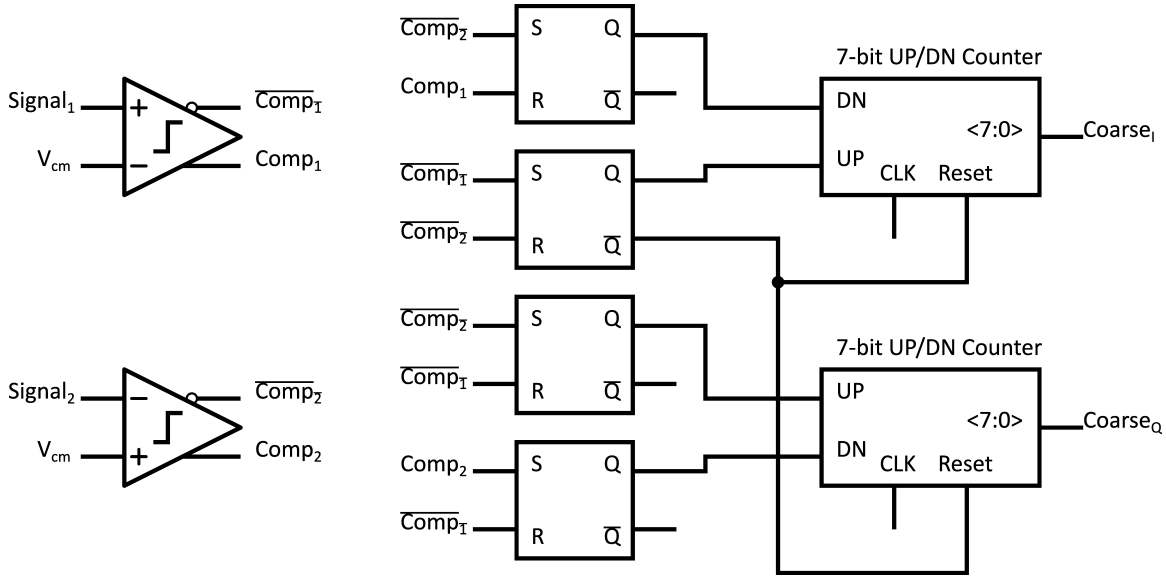

Figure 6-15: Schematic of the Coarse Counter

by two positive-feedback comparator circuits. The outputs of the comparators are fed into a couple of SR latches to produce four trigger signals for the previously mentioned two 7-bit Up-Down Counters. The combined schematic of the Coarse Counter can be seen in Figure 6-15. The Up-Down Counters count up only if UP is HIGH and DN is LOW. When UP and DN are both HIGH or both LOW, a simple clock-gating circuit stops the counters. A simple multiplexing circuit selects the counter (I or Q) that is nonzero to be available at the output as the 7 (out of 8) least significant bits bits of the Coarse Counter circuit. The most significant bit of the result is simply "which (I or Q) counter is currently active". Put together, the Coarse Counter circuit gives a result with 8-bit resolution. Figure 6-16 illustrates how the I and Q counters work from 0° to 360°. It can be seen that only one counter counts at any time, and the other one stays at 0. An example of waveforms showing how the internal logic of the Coarse Counter works is presented in Figure 6-17. In this example, the comparators' outputs are designated as $Comp1$, $\overline{Comp1}$, $Comp2$ and $\overline{Comp2}$. Similarly, the outputs of the SR Latches are designated as UP_{I},DN_{I}, UP_{Q} and DN_{Q}. $Signal_1$ goes over V_{cm} at $t = 0$, and triggers state changes in the SR latches, which in turn triggers the

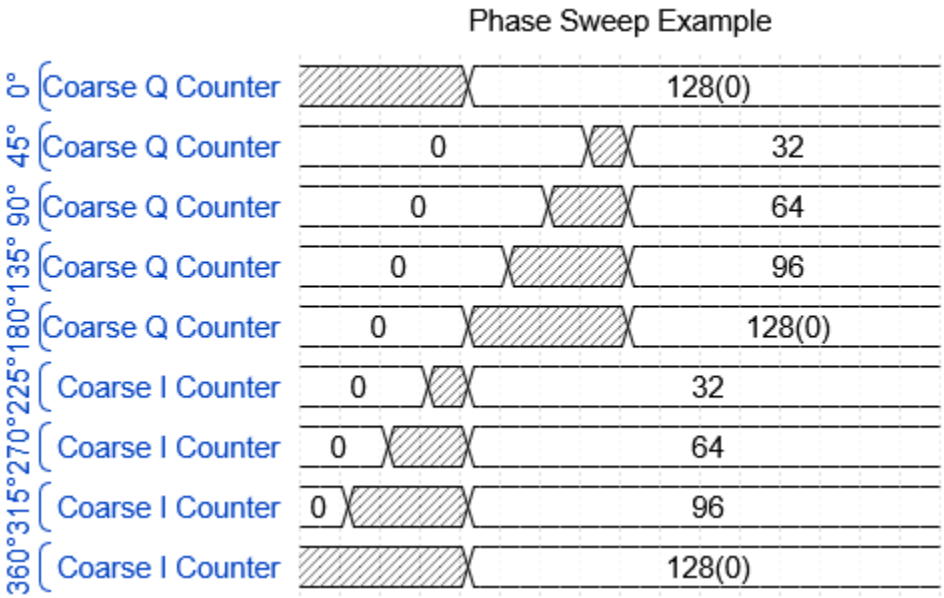

Figure 6-16: Example waveforms of how the I and Q Coarse counters work across 0°-360°.

counters. However, as designed, only one counter starts counting. $Coarse_I$ stays at 0 because UP_1 and DN_1 are both LOW, but $Coarse_Q$ starts counting since UP_Q is HIGH and DN_Q is LOW. $Coarse_Q$ keeps counting until $Signal_2$ goes over V_{cm} as well, and triggers another wave of changes to the SR Latches. This time, DN_Q also goes HIGH and stops $Coarse_Q$, thus the output of the Coarse Counter is ready.

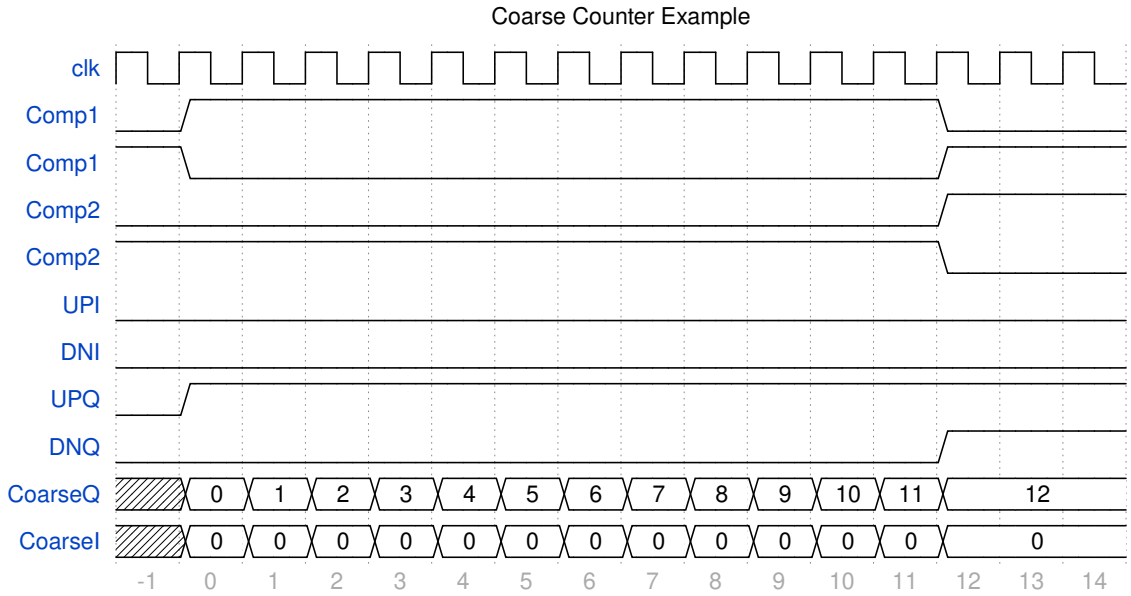

Figure 6-17: Example waveforms of how Coarse Counter works

6.4.1.1 Positive Feedback Comparator

This specific implementation of the positive-feedback comparator circuit can be seen in Figure 6-18 (a). The core circuit resembles a basic 5-Transistor operational transconductance amplifier (OTA), but the cross-coupled branches provide positive feedback. Then two inverters on the outputs of the comparator help with restoration of the core's outputs to rails. This comparator design can become a hysteresis comparator, and can be used like a Schmitt Trigger, when $k > 1$. An example of voltage transfer characteristic of the comparator circuit with $k = 1$ and $k = 8$ can be seen in Figure 6-18 (b). Hysteresis comparison is a very popular and powerful tool, since it solves the comparator bounce issue, which is the rapid bounce that can happen at the output of a comparator when the two inputs are very close to each other. The comparator only settles to a state (HIGH or LOW) when the difference between the two inputs exceeds some threshold. However, in the FD-NIRS application, this hysteresis can significantly degrade the phase measurement results. For example, assume that this threshold is set to 50 mV. If the signal coming to a comparator has 100 mV amplitude, the signal will cross the threshold at 30°, but if the signal has 1 V amplitude, it will cross the threshold at ∼2.9°. The phase measurement results of the two cases would

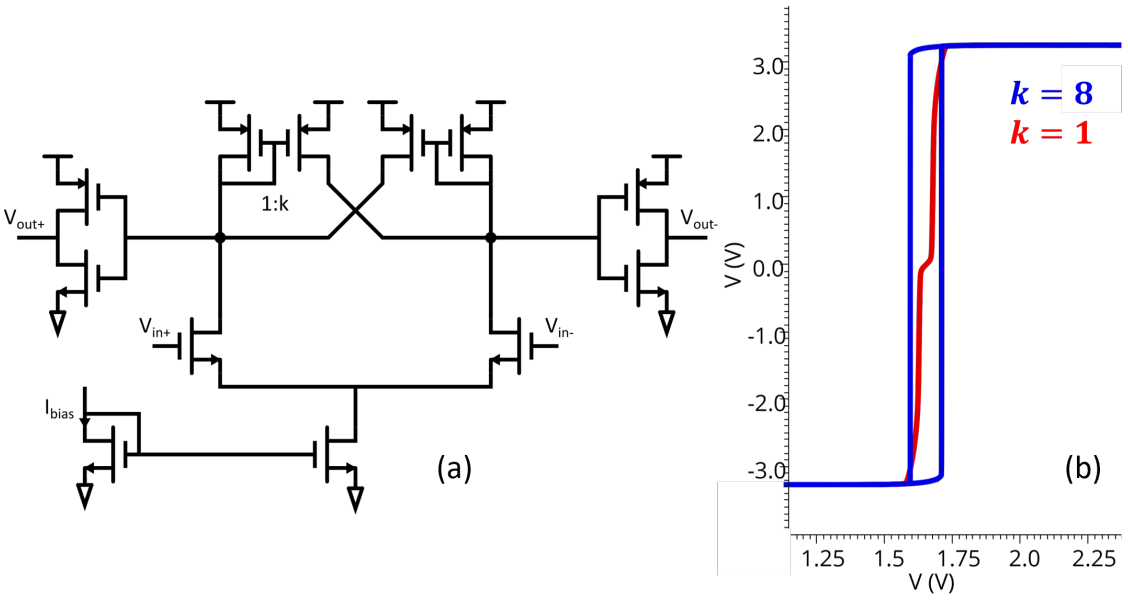

Figure 6-18: (a) The schematic of the positive-feedback amplifier (b) The different effects of $k = 1$ and $k = 8$ on hysteresis.

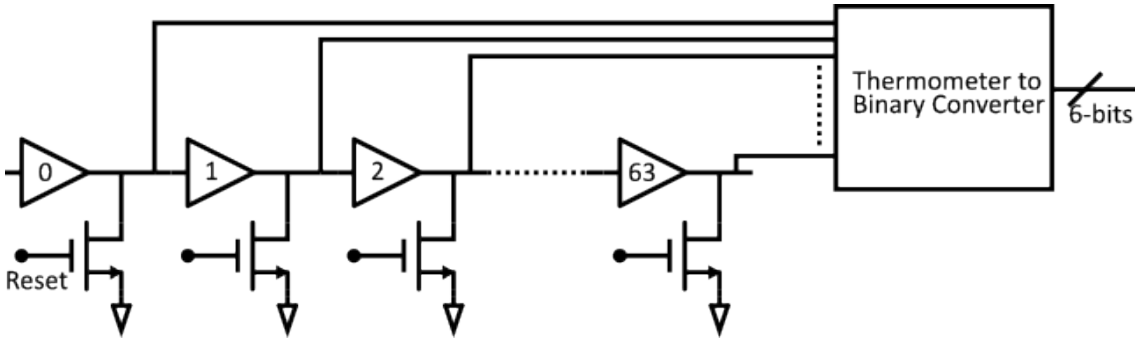

Figure 6-19: Schematic of the Delay-Line based Fine Counter with the Thermometer-to-Binary Converter

be different by ∼27.1°.

6.4.2 Fine Counter

Fine Counter is a delay-line based circuit that breaks down one period of the Coarse Counter into 64 equal pieces. The core circuit consists of 64 Delay Elements, followed by a Thermometer-to-Binary Converter. The basic idea is to propagate a pulse-like trigger signal through the delay-line and keeping track of how many delay-elements that the trigger signal passes through. The schematic of this chain can be seen in

Figure 6-19. The delay amounts are programmable by an external current source, and should be calibrated carefully to ensure that entire range of the Fine Counter spans one period of the Coarse Counter for the best performance. If the Fine Counter span falls short, there will be blind spot of phase values that can't be properly measured. For example, if one period of the Coarse Counter is 300 µs and the delay is set to 4 ns, the Fine Counter will start counting as designed for the first 256 ns of the Coarse Counter period and will reach to 63 count. However, the rest of the period will also return 63 count as the measurement result. On the other hand, if the Fine Counter span exceeds one Coarse Counter period, the full resolution of the Fine Counter will not be achieved. For example, if the Coarse Counter period is 300 ns but the Fine Counter delay is 10 ns, the Fine Counter's maximum count will be only 30 and the resolution of the phase detector becomes almost half of what it could have been with properly calibrated delay.

6.4.2.1 Delay Element

The Delay Elements are designed as two simple inverters, where the first one is current-starved. The current-starved inverter slows down and controls the second inverter's propagation delay. The second inverter, on the other hand, both regenerates

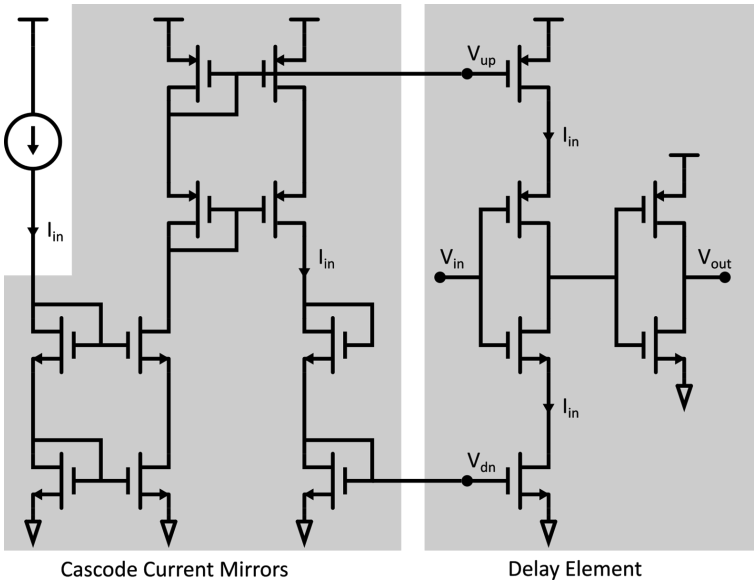

Figure 6-20: The schematic of the Delay Elements

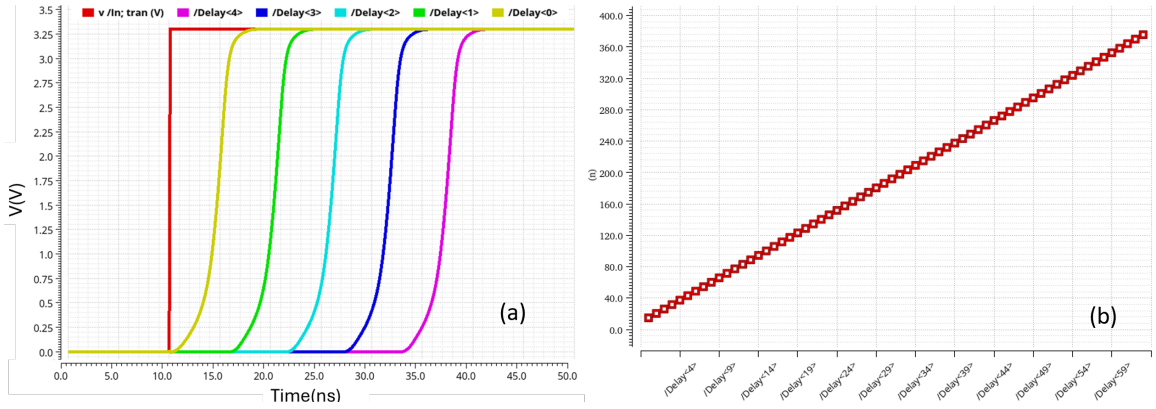

Figure 6-21: (a) The schematic of the Delay Element, (b) Example transient waveforms of five consequent Delay Elements with a trigger signal In.

the output to the rails and turns V_{out} to the same polarity as V_{in}. Current starvation is done by forcing the current of the first inverter with current mirrors on both the low-side and the high-side. The schematic can be seen in Figure 6-20. An example transient waveform group can be seen in Figure 6-21(a). The input trigger signal In becomes HIGH at $t = 10\,\text{ns}$. Then the outputs of the Delay Elements (up to 5 elements in this example) follow In one by one with equal propagation delays. Another way of extending and visualizing the behavior of delay elements can be seen in Figure 6-21 (b). Here, the time instances of each delay element that crosses the midpoint of V_{DD} are plotted. As expected, each delay element crosses the mid-supply point the same amount of time after the previous one.

6.4.2.2 Fine Counter Driver

Even though the working principle of the Fine Counter is simple, it needs some peripheral circuits to work properly. There are two main problems that need to be solved. The first is, at which Coarse Counter clock should the Fine Counter be triggered. This is more a performance improvement in real life power consumption and simulation time, rather than a functionality assurance. The trivial solution is to trigger the Fine Counter at every Coarse Counter clock. This works because the Fine Counter is already supposed to work inside the Coarse Counter period. However, this also means that the Fine Counter will just keep resetting at each Coarse Counter

clock, counting again and again, waste power after the tape-out, and also increase the simulation time significantly during development. To solve this, simple combinational logic circuits were designed to trigger the Fine Counter only after zero-crossing events happen, but before the clock edge that starts the Coarse Counter. In other words, instead of the Fine Counter working inside a Coarse Counter period, it starts just before the clock edge that starts the Coarse Counter. This brings us to the next problem: When should the Fine Counter stop? If it does not stop or at least its output is latched at some point, the Fine Counter will just count up to 64 and the information will be lost. To avoid this, the Fine Counter's output is simply latched by 6 flip-flops (FFs) on the clock edge that makes the Coarse Counter 1.

6.4.2.3 Thermometer to Binary Converter

Due to its nature, the output of the Delay Line is a 63-bit Thermometer code. Obviously, it is unrealistic to use this as output due to pin count limitation. Therefore, a Thermometer to Binary Converter is designed to reduce the pin count to only 6. There are a few different implementations in the literature, such as read-only memory (ROM) encoders [85, 86], Fat Tree encoders [87, 88], Wallace tree encoder [89]. The design chosen here is a based on multiplexers [90] due to simplicity and the modular structure. The multiplexers were designed with the transmission gate approach. The schematic of a 15-to-4 thermometer to binary converter can be seen in Figure 6-22. The design philosophy is extended to 63-to-6 for the purposes of this design.

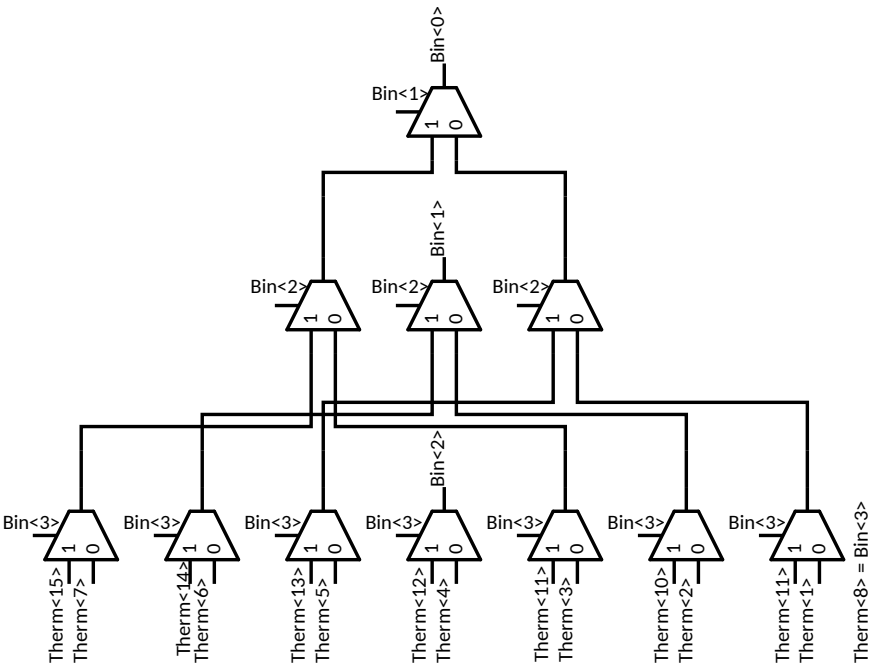

Figure 6-22: Schematic of the MUX based 15-to-4 thermometer to binary converter.

6.5 Laser Driver

Towards the effort of integrating as many functionality as feasible that an FD-NIRS instrument needs, a laser driver circuit is also integrated. The circuit is a modification of the well-known constant current driver circuit [91]. However, the key difference is how the feedback is implemented. The commercial laser diodes aimed to be used in our instrument (HL6750MG, HL8338MG) come with a low bandwidth integrated photodetector inside the package, which produces a feedback current that is proportional to the optical power output of the laser diode. A feedback mechanism can be designed around this feedback current, so that the optical output of the laser diodes is constant across a range of temperature, aging, and other factors that affect the efficiency of the laser diode. In the constant current driver circuit (Figure 6-23), feedback is taken between the source of the driver transistor and the resistor connected to its source. The error amplifier will ensure that the voltages at its two inputs are equal to each other, hence $V_{fb} = V_{ref}$ and $I_S = I_{LD}$. This approach keeps the forward current of the laser diode; however, if the quantum efficiency of the laser diode ($\eta = P_{optical}/P_{electrical}$) changes due to temperature or aging, this type of feedback is not useful. Therefore, a

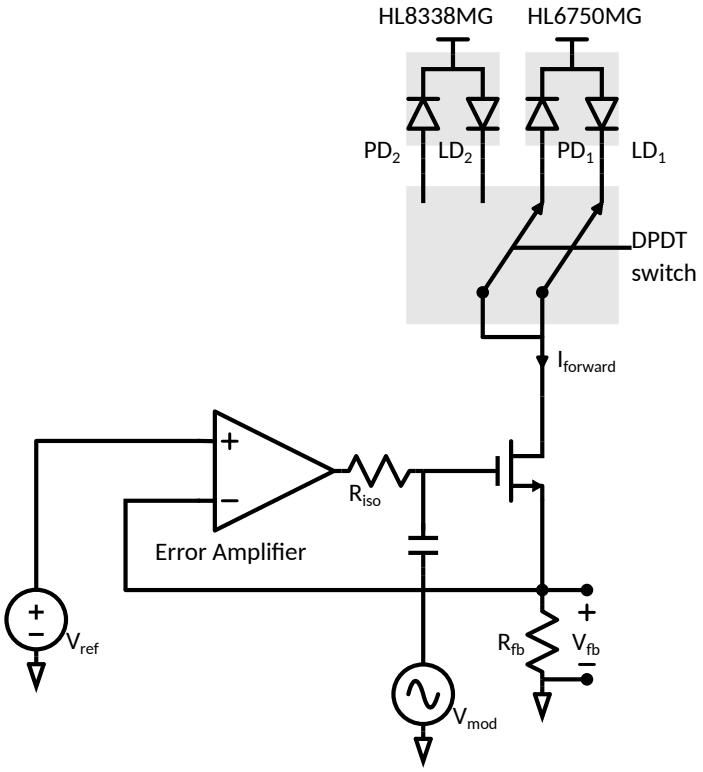

Figure 6-23: Schematic of the Constant-current Laser Driver

new feedback was designed to utilize the feedback current produced by the integrated photodetector. The schematic can be seen in Figure 6-24. The feedback current is routed to a resistor to produce a feedback voltage V_{fb}, and the error amplifier ensures that $V_{fb} = V_{ref}$. Instead of keeping the forward current constant, this approach tries to keep the feedback current constant across temperature, aging, etc.; hence even if the quantum efficiency of the laser diode changes, the optical output can stay constant by adjusting the forward current. This mechanism in action can be seen in Figure 6-25. In this plot, the ratio $\Gamma = I_{forward}/I_{feedback}$ is used to model the quantum efficiency of the laser driver. This approach is useful since $I_{forward}$ is a direct representation of $P_{electrical}$ and $I_{feedback}$ is a direct representation of $P_{optical}$. The nominal value for Γ was taken as 466. This number was calculated from the HL6750MG datasheet [61] as the ratio of the operating current (70 mA) and the monitor current (0.15 mA) under typical specifications. In Figure 6-25, this ratio was swept between 400 and 532. The feedback mechanism adjusts $I_{forward}$ to 59.7 mA at $\Gamma = 400$, and 79.4 mA at $\Gamma = 532$, while $I_{feedback}$ changes only from 149.332 µA to 149.330 µA, a total of only 1.4 parts

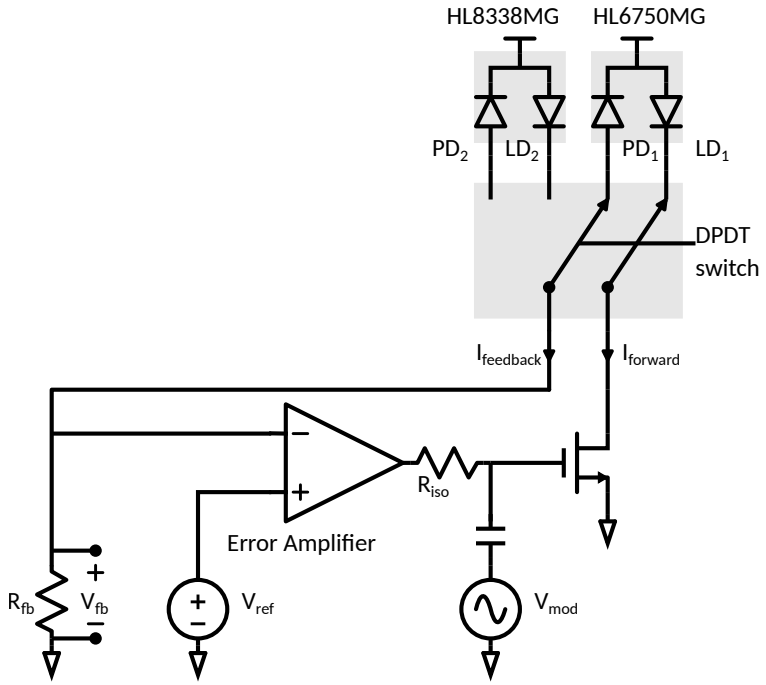

Figure 6-24: The implemented laser driver circuit with monitoring current feedback

per million. Another way of looking at how the feedback mechanism works can be seen in Figure 6-26. In this figure, it can be seen how the DC average of $I_{forward}$ changes from $\sim 60\,\text{mA}$ to $\sim 80\,\text{mA}$ to compensate for the change Γ, while the DC average of $I_{feedback}$ does not change. The AC sinusoidal modulation on top of the DC average changes $\sim \pm 14\%$ due to changing Γ. If the laser driver was a simple constant current feedback circuit, the amount of change in $I_{feedback}$ would have been $\sim \pm 14\%$, which would correspond to $\sim \pm 14\%$ change in $P_{optical}$. As mentioned in Chapter 1, FD-NIRS utilized a sinusoidally modulated light source, so the sinusoidal modulation needs to be coupled to the laser driver somehow. There are a few different ways to achieve this, such as injecting the signal into the drain of the driver transistor, using a sinusoidally varied V_{ref}, or injecting the modulation into the gate of the driver transistor. Using a variable V_{ref} does not work properly with the feedback scheme selected here, since the integrated photodetectors are low-bandwidth, they cannot keep up with V_{ref}. This disturbs the balance between the inputs of the error amplifier, and causes the error amplifier's output to bounce between the rails. Injecting the modulation into either the gate or the drain of the driver transistor options works with the feedback scheme.

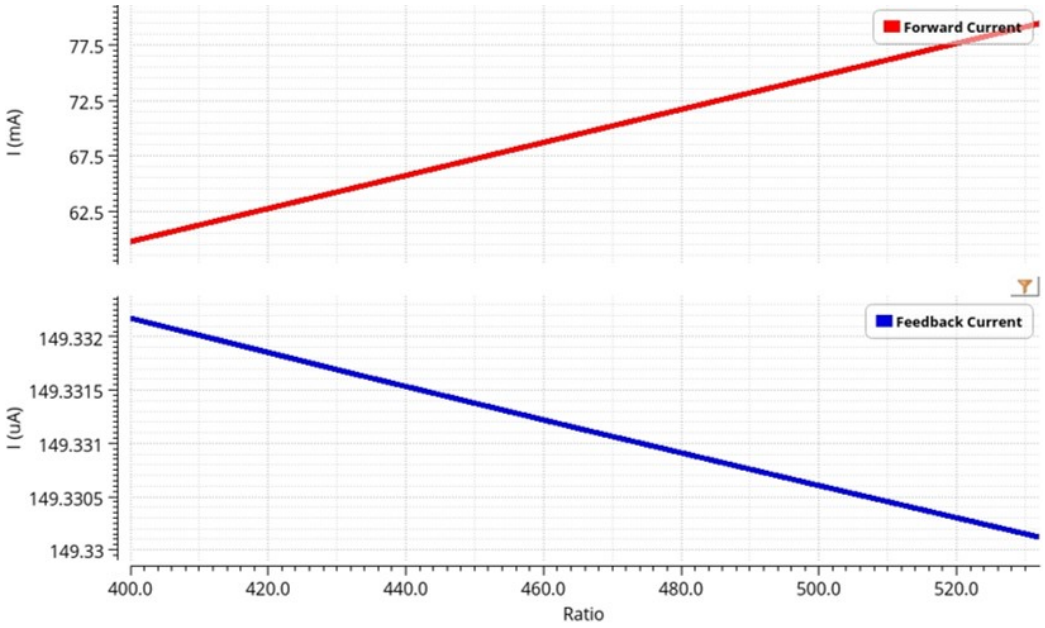

Figure 6-25: Forward current and Feedback current versus changing quantum efficiency η, for various ratio Γ.

Here, injecting to the gate of the driver transistor was selected because this allows for better post-tape-out flexibility. For example, if the laser driver circuit does not work properly after tape-out, the circuit in Figure 6-23 can still be operational by shutting down V_{ref} and driving the transistor solely with V_{mod}. In this scenario, V_{mod} has to provide appropriate DC bias to the driver transistor as well as the modulation, but the feedback mechanism becomes non-operational. If the modulation were to be injected into the drain of the driver transistor and the laser driver circuit does not work post-tape-out, there is nothing can be done to salvage some functionality.

6.6 Conclusion

In this chapter, the design methodology and implementation of the major analog and mixed-signal components of a compact FD-NIRS system were presented. The performance limitations of the chosen avalanche photodiode were quantified and the requirements they imposed on the front-end circuitry were derived. Trade-offs between noise, bandwidth, and dynamic range were examined in detail, leading to the design of a fully differential resistive-feedback TIA with optimized gain and power consumption.

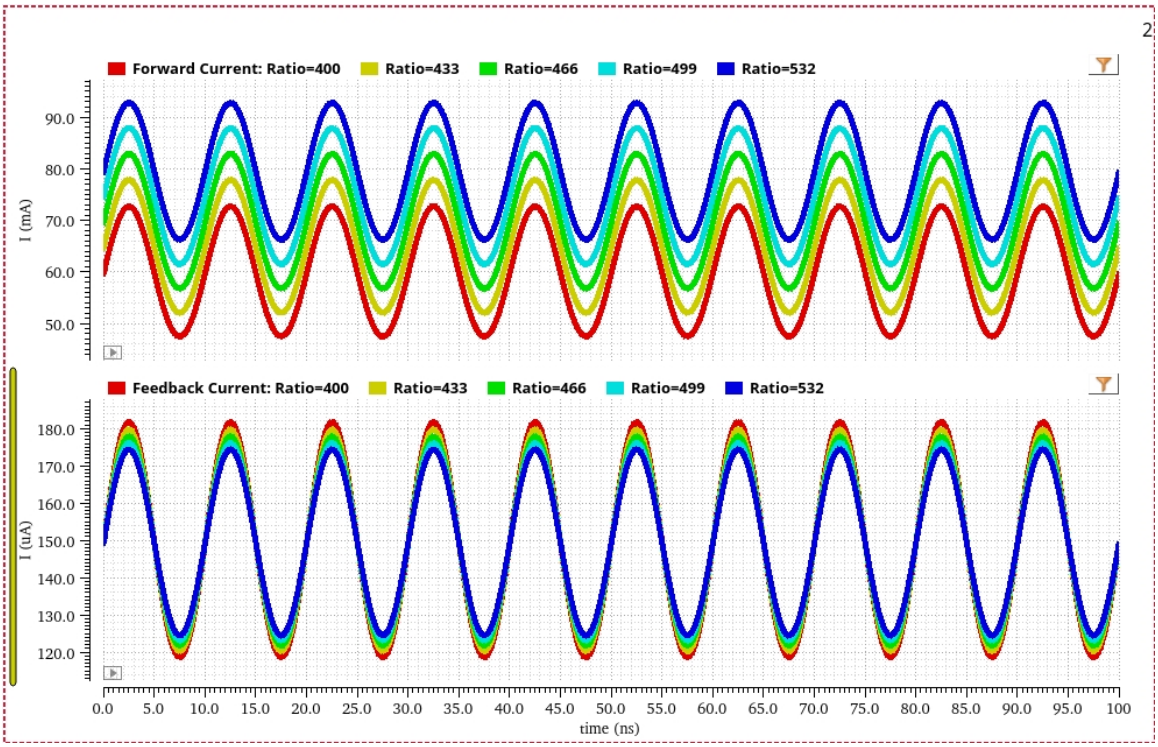

Figure 6-26: Time series representation of Forward current and Feedback current with changing quantum efficiency η, for various ratio Γ.

The subsequent mixer stage was designed with emphasis on linearity and dynamic range, while the amplitude detection and phase detection circuits were integrated in a manner compatible with miniaturization and low-power operation. On top of the analog front-end and readout, a laser driver circuit was developed that incorporates feedback from integrated monitor photodiodes to ensure stable optical output under varying conditions.

The presented analysis and designs establish the foundation for a highly integrated FD-NIRS system that balances sensitivity, accuracy, and compactness. Although trade-offs remain in terms of bandwidth, linearity, and noise performance, the work demonstrates how careful circuit-level considerations can overcome the primary challenges of FD-NIRS instrumentation. These results not only guide the construction of the next-generation ASIC, but also highlight a path toward wearable and scalable FD-NIRS devices capable of advancing both research and clinical applications.

Chapter 7

Conclusions and Future Outlook

7.1 Conclusions

Three, sir.

Galahad, Monty Python and the Holy Grail

Turning FD-NIRS technology into a miniaturized and wearable form factor can unlock new capabilities and features at a time when there is a shift towards personalized point-of-care platforms instead of conventional healthcare. The works described in this thesis make important contributions towards this eventual miniaturized and wearable instrument in the following ways:

- 3 separate new generations of instruments were designed, each with further integration than the previous ones. These instruments were validated with tissue mimicking solid phantoms, and with further *in-vivo* occlusion experiments. The first new-generation instrument replaced two separate benchtop signal generators with an integrated DDS. The resulting instrument consisted of a three-stack PCB, the probe, and an NI DAQ for phase and amplitude readout. The next generation integrated phase and amplitude readout functionality with the help of demodulator circuits. In the final instrument, the readout circuits were replaced with an STM32 microcontroller, which reduced instrument size and complexity. Each of these generations represents a step towards miniaturizing and wearability

of the very powerful FD-NIRS technology.

- The efforts to miniaturize the instrument through the integration of the functionalities led to the identification of specifications and performance metrics for the modules that realize these functionalities. Some of the recognitions include phase noise performance for signal generator, system-wide data acquisition rate, noise performance and dynamic range analysis for the AFE, readout circuit performance in terms of phase and amplitude stability, etc. These realizations and experiences will guide future efforts and be helpful as rules of thumb.

- A new generation of FD-NIRS ASIC where many of the fundamental functionalities required by an FD-NIRS system are integrated. In addition to the analog front-end, the phase and amplitude detectors as well as a laser driver circuit are designed. The simulations suggest that this ASIC had a bandwidth of 147 MHz with 8 pF input capacitance load, with a noise performance of 30 $\mathrm{nA_{rms}}$ input-referred noise current. This noise performance is better than the minimum amount of current the chosen APD is calculated to output, therefore shifting the noise limitation to the photodetector. Furthermore, the dynamic range of 41 dB was achieved. The phase detector employs the Fine-Coarse scheme and achieved a resolution of 0.02° with a 14-bit digital output. The designed amplitude detector is based on a peak detector architecture and shows only 1 % DNL within the 95 % of the supply range, making its performance almost rail-to-rail. The laser driver was designed to automatically compensate for the factors that affect the quantum efficiency of the laser diodes such as aging/temperature. Additionally, the laser driver circuit can easily be turned into the simpler, constant-current driver topology in the post-silicon phase, if needed. An eventual FD-NIRS instrument can be constructed with this new ASIC, a DDS, and a microcontroller.

7.2 Outlook

7.2.1 Signal Generation

In Chapter 6, the requirements and the design process of Generation 2 FD-NIRS ASIC were discussed. In this new proposed design, on top of a new analog front-end, a laser driver circuit and amplitude and phase detector circuits were integrated. The only major block that was still not integrated was signal generation. The main reason why this approach was chosen was that integrating a DDS would be a huge ordeal. The working principle of a DDS boils down to a very high performance digital-to-analog converter (DAC) that is driven by either a lookup table of digital codes or an FPGA that generates the digital codes on the fly. Both designing this DAC and the generator of the digital codes should be considered as multi-year projects. However, in their work Yazdi et. al. showed an FD-NIRS ASIC where they integrated a signal generator [44]. This signal generator was designed as a current-starved quadrature ring voltage controlled oscillator (VCO). The oscillation frequency could be adjusted by adjusting the current supplied. This approach allowed Yazdi et. al. to vary the frequency between 50 MHz to 1 GHz. They reported -40 dBc/Hz at 1 kHz offset from 100 MHz carrier and -80 dBc/Hz at 100 kHz offset from 100 MHz phase noise. This performance is significantly worse than the performance reported for AD99959. In post tape-out solid phantom experiments, they measured 1.7°rms. Although our Generation 4 Instrument achieved 0.082° and performance differences cannot be solely attributed to signal generators, these results suggest that there can be a signal generator design between these two in terms of design efforts. This could be one of the next avenues to be investigated if the Generation 2 FD-NIRS ASIC succeeds and yet another generation of the FD-NIRS ASIC to be designed.

7.2.2 Fine Counter Driver

In Section 6.4.2.2, the driver circuit for the Fine Counter was mentioned but was not explained in detail due to the design process of this circuit. This circuit was designed

by plotting several time domain signals in Figure 6-15 such as $\overline{Comp1}$, $Comp2$ and UP_{I} or DN_{Q} and figuring out which combination of these signals would trigger the Fine Counter so that it is activated only once and just before the Coarse Counter starts. No formal solution to this triggering problem was developed. Although extensive simulations with phase differences at every quadrant (if one divides 360° into four quadrants) did confirm that the driver works for each quadrant, this is only an epagoge, not a formal solution. Investigating a formal solution for the generation of this trigger signal can be a worthwhile effort.

7.2.3 Temperature Stabilization

The instruments that were described in Chapters 3, 4 and 5 all featured laser driver circuits that use a feedback mechanism to modulate the forward current of the laser diode in order to keep the optical power output constant across varying conditions like temperature or aging. Although metal SMA connectors help to dissipate heat passively, one important missing feature was active temperature control. Figure 7-1 shows how The wavelength and the quantum efficiency of laser diodes drifts with case temperature. For example, 0.175 nm/degree drift is reported for the HL6750MG diodes used in the works reported throughout this document [92]. Similarly, the quantum efficiency η of these laser diodes degrades with increasing temperature, causing the laser driver to push more current to compensate, which in turn increases temperature and eventually causes thermal runaway. This was not observed in the instruments presented here. However, as the work on these instruments progresses and the overall sizes of the instruments become smaller, the thermal runaway can become a real concern. This could affect not only the laser diodes, but all other electronics as well, especially consumer grade ICs, which can have operating temperature ceilings as low as 70 °C.

One solution can be to use butterfly laser diode mounts instead of simple SMA connectors. These mounts usually come with built-in TEC controllers, which monitor the laser diode's temperature and keep it constant with active cooling. An example of such a solution can be seen in Figure 7-2(a). Obviously, this type of solution increases

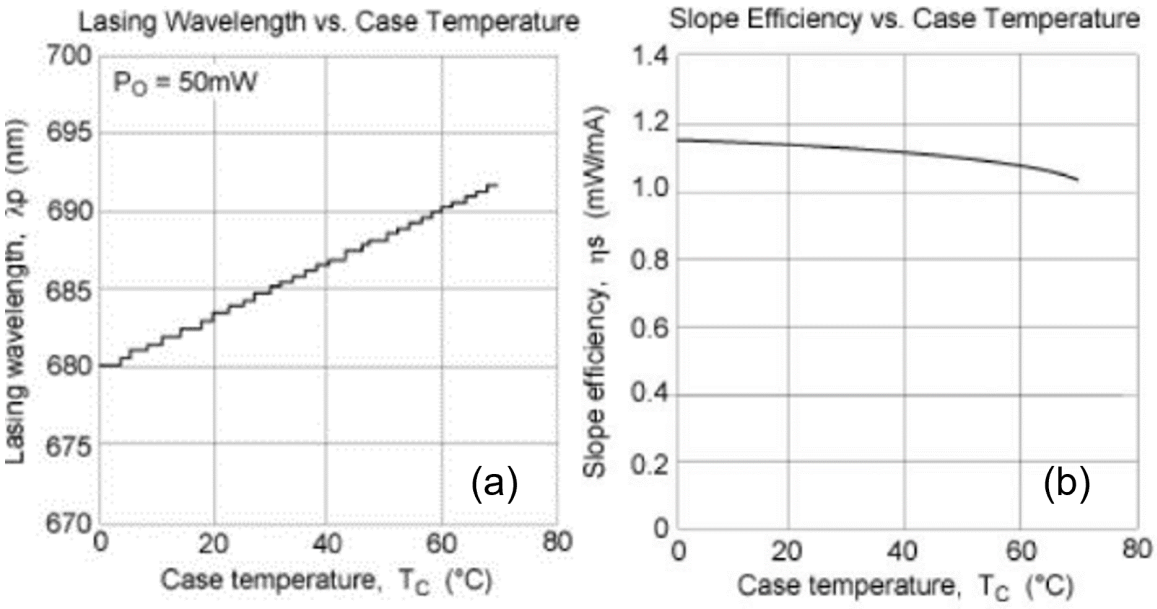

Figure 7-1: (a) Wavelength drift with case temperature. (b) Quantum efficiency with case temperature.

the laser diode footprint significantly, therefore, a hindrance for the miniaturization attempts. So, a different solution might be more suitable. One candidate might be Peltier TEC coolers (Figure 7-2(b)). These devices transfer heat from one side of a semiconductor to the other side using the Seebeck effect, creating a cool surface and a hot surface.

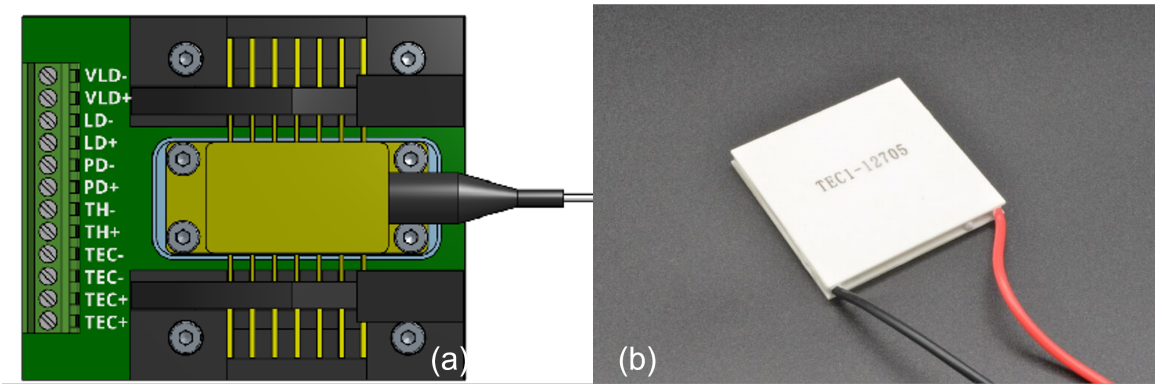

Figure 7-2: (a) An example of a butterfly mount laser diode with pigtail fiber on the right hand side. (b) An example of a Peltier TEC cooler.

7.2.4 Dynamic Range Enhancement

In Section 6.2 the logarithmic transimpedance amplifiers were discussed as a part of the TIA design. These amplifiers create a logarithmic relationship between their input and output by leveraging the exponential relationship between the collector current and V_{be} of a BJT. However, they were found to be to be unsuitable for FD-NIRS applications because of their varying bandwidth and noise performance with varying input signal amplitudes. A further investigation can be made towards pseudo-logarithmic amplifiers. As the name suggests, these are not true logarithmic amplifiers, therefore there might suitable designs which the bandwidth and noise performances might not be affected by the input signal amplitude. Although the pseudo-logarithmic amplifier was designed as a variable gain amplifier after the TIA, one such implementation was presented in [43]. One other avenue for dynamic range enhancement can be gain switching. This feature can easily be integrated into the TIA design described in Section 6.2.1. However, gain switching is not compatible with the DS / SC approach, since one of the assumptions that enable DS / SC is constant detector gains. In this context, detector gain should be considered not only as the photodetector gain, but the entire chain from the photodetector all the way to amplitude measurement.

7.2.5 Silicon Photodetectors

Throughout all these instruments, the photodetector of choice has been S9251-15 (Hamamatsu), Even the Generation 2 FD-NIRS ASICs analog front-end was designed with this photodetectors noise performance and parasitic junction capacitance in mind. This photodetector operates at $-200\,\mathrm{V}$ supply voltage to achieve avalanche breakdown and avalanche gain of 100. Silicon photodetectors, on the other hand, can be sensitive to light in the spectrum of interest, operate at supply voltages as low as $5\,\mathrm{V}$, and have significantly smaller junction capacitances, all at the same time. However, at the time of writing this thesis, no commercially available silicon photodetector in a suitable packaging had a low enough noise level. Research and development on better

silicon photodetectors is an ongoing effort in both academia and industry. These efforts are also being supported by the emerging technology of self-driving cars that uses ligth detectrion and ranging (LiDAR) for object detection. Therefore, silicon photodetectors with better noise performance might be available in the future and be integrated into a future instrument. This would eliminate one more obstacle towards the miniaturized and wearable FD-NIRS instrument.

Chapter 8

Appendix

Three!

King Arthur, Monty Python and the Holy Grail

After the design and validation of the Generation 4 Instrument that was described in Chapter 5, in Chapter 6 the new Generation 2 FD-NIRS ASIC is described. However, before tackling such an undertaking like a completely new IC design in a new process node, some preliminary work towards the system specifications should be done. To this end, a new generation of the instrument was designed. This version of the instrument should not exactly be considered as one of the iterations towards miniaturized FD-NIRS technology. It should be considered as a sidestep, where the analog front-end inside the Generation 1 FD-NIRS ASIC was completely disintegrated and built with off-the-shelf components. This approach allowed to put some minimum or maximum numbers to some of the design specifications. Although the miniaturization of the FD-NIRS technology was not a goal of this instrument, it can still be an example of how small an FD-NIRS instrument can become.

The top view of the instrument can be seen in Figure -1. The electronics and mechanical components in this instrument are all on the top-side, and the optics are all on the bottom. The size of this instrument is 8×5.5 cm^2, the same as that of a regular credit card. Similarly to Generations 3 and 4, this instrument was also designed with the DS / SC approach in mind, therefore the design contains two separate analog

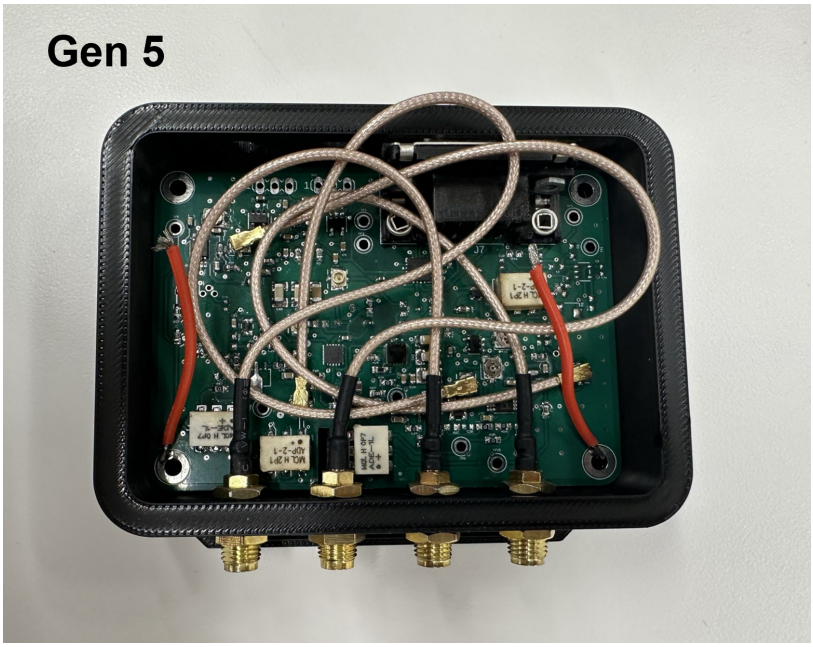

Figure -1: Top view of the Generation 5 instrument.

front-end channels that interface with two separate S9251-15 APDs. There are also four laser diodes, two at 690 nm and two at 830 nm. As mentioned above, these optics are all on the bottom side of the instrument, so they cannot be seen from Figure -1. Since this instrument was designed as a side step, not all functions that were integrated into the instrument in Generations 1-4 are available. This decision was made to obtain a faster turnaround time both for the design of the instrument and for iterating over the design. There were three missing modules; the DDS for signal generation, a microcontroller for sampling the outputs and experiment flow control, and the high voltage APD supply. In order to compensate, one D-sub 9 and four SMA connectors were added. The D-sub 9 cable brings in power, signals to turn on/off the laser diodes, and the -200 V APD supply. One of the SMA connectors brings the modulation signal for the laser driver, another one brings in the LO signal, and the final two connectors are used to connect the outputs of the two analog front-end channels to an oscilloscope for inspection and phase/amplitude extraction. One feature of this instrument is that there are two additional SMA connectors in addition to the ones mentioned. These connectors can be used to inject a very small signal from a benchtop signal generator to mimic the APD signal. In this way, a controlled amount of signal can be injected

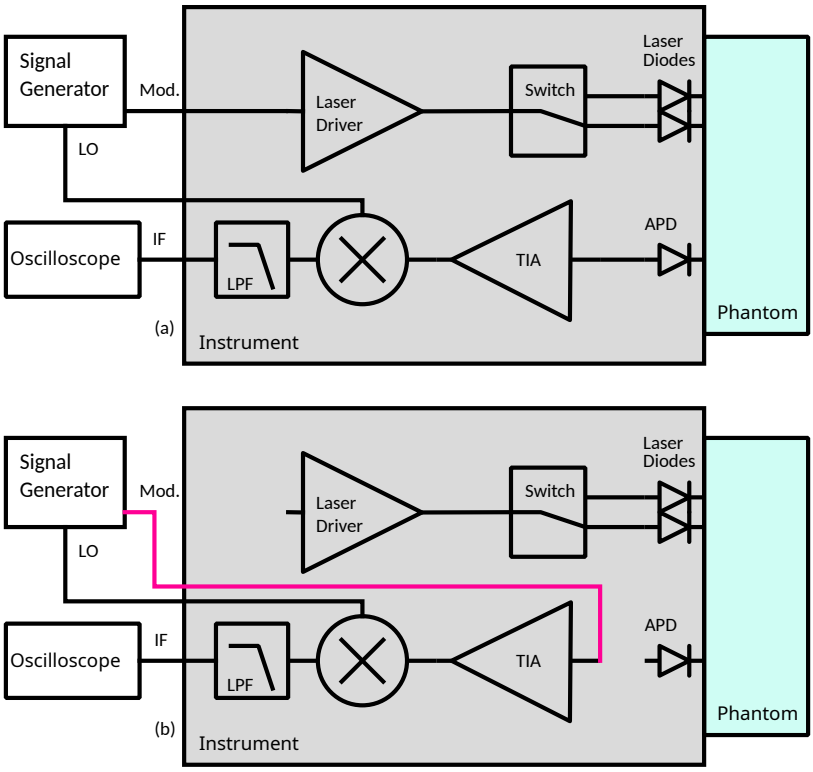

Figure -2: Block diagrams of the two functional configurations of the instrument. (a) is the default configuration, which would be used in an actual FD-NIRS experiment. (b) is the configuration that isolates the optical components, and was used for characterizing the instrument.

into the analog front-end, and the response of the entire chain can be characterized. Without these additional connectors, characterizing the channels would be nearly impossible. The options for off-the-shelf TIAs that are suitable for FD-NIRS are quite slim. The need for simultaneous need for low-noise, high-gain, high-bandwidth, and tolerance to high-capacitance photodetectors is a very challenging trade-off. The only suitable option available was MAX40661. Although originally this component was designed for LiDAR applications, and hence digital rail-to-rail output waveforms, it can still be suitable for analog applications. The component has a bandwidth of 160 MHz with two gain options, 25 k (90 dB) and 50 k (93 dB) and is optimized for C_{in} of $5 - 12$ pF. As mentioned above, an SMA connector is used to bring in modulation and LO signals. Since there are two channels in this instrument, the signals that were brought in should be divided into two, keeping the characteristic impedance considerations in mind. This is done by the ADP-2-1+ Power Splitter/Combiners

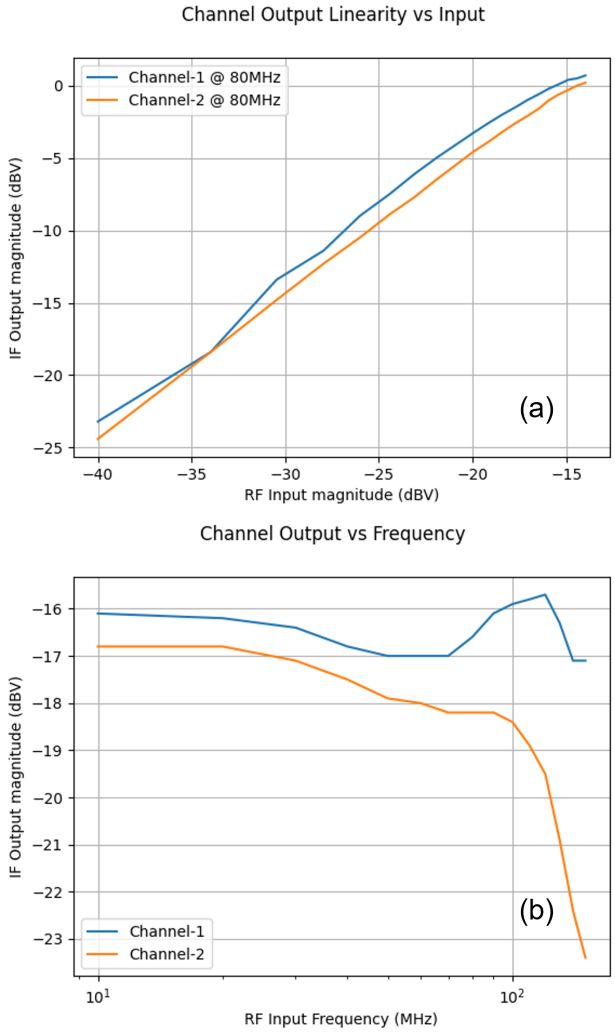

Figure -3: Panel (a) shows the RF input magnitude vs IF output magnitude of both channels. Panel (b) shows the IF output magnitudes versus modulation frequency.

from Mini-Circuits. These are passive, surface mount power splitters/combiners. The heterodyned down-conversion is done by ADE-1L+ Mixers from Mini-Circuits. These are passive ring-diode mixers with 500 MHz bandwidth and 5.3 dB conversion loss. Finally, the low-pass filtering after the heterodyne down-conversion was done by two active filters with Sallen-Key topology. Since these are active filters, they provide significant gain to compensate for the passive mixers and the relatively, with respect to Generation 1 FD-NIRS, limited gain of the TIAs. A detailed characterization was performed on the receiver channels, using the idea in Figure -2 (b), that is, injecting the modulation signal directly into the TIAs. Figure -3(a) shows the dynamic range

of the two channels. The inputs and outputs are shown in units of dBV. The 0 dbV on the y-axis at the upper limit corresponds to $\sim 2.8 V_{peak-to-peak}$, which is very close to the upper supply rail of 3.3 V. However, the lower limit was achieved with the smallest amplitude option available with the signal generator that was used. So, a dynamic range of at least 25 dB was achieved, but the real dynamic range of this instrument can be higher.

Figure -3(b) on the hand shows the frequency response of the channels. Keep in mind that the channels include the heterodyned down-conversion, therefore the quantity in the y-axis is the down-converted IF signal's amplitude. An interesting observation is that one channel shows significantly higher -3 dB bandwidth than the other due to the gain peaking around 100 MHz. This was unexpected since the channels are constructed with the same components. One possible cause could be issues with the characteristic impedance control with the PCB. Although special care was taken to ensure that every trace that will carry high-frequency signals was designed with the characteristic impedance 50 Ω, the manufacturing process of cheap turn-key PCB manufacturers can introduce variations within different locations of a PCB. This also illustrates why the multi-frequency method is more difficult to implement engineering-wise compared to the multi-distance method. Figure -4 shows the measured amplitude and phases of both channels, with the configuration in Figure -2(a), that is, with the optical components in the loop and the light travels through a solid phantom. In Figure -4 (a), the phase increase can be seen with increasing modulation frequency. This behavior was predicted in Equation 2.7. Similarly, the low-pass behavior in Figure -4 (b) is consistent with Equation 2.6, however, since Figure -3 already established a low-pass behavior for the analog front-ends of this instrument, the low-pass behavior in Figure -4 (b) cannot solely be explained by Equations 2.6.

After all this characterization efforts, unfortunately no successful solid phantom or *in-vivo* experiments could be performed. The reason for this was determined to be the insufficient noise performance of the TIA. The datasheet of the TIA suggests $\sim 1\,\mathrm{mV}_{rms}$ output referred integrated noise. Although this number itself is quite low,

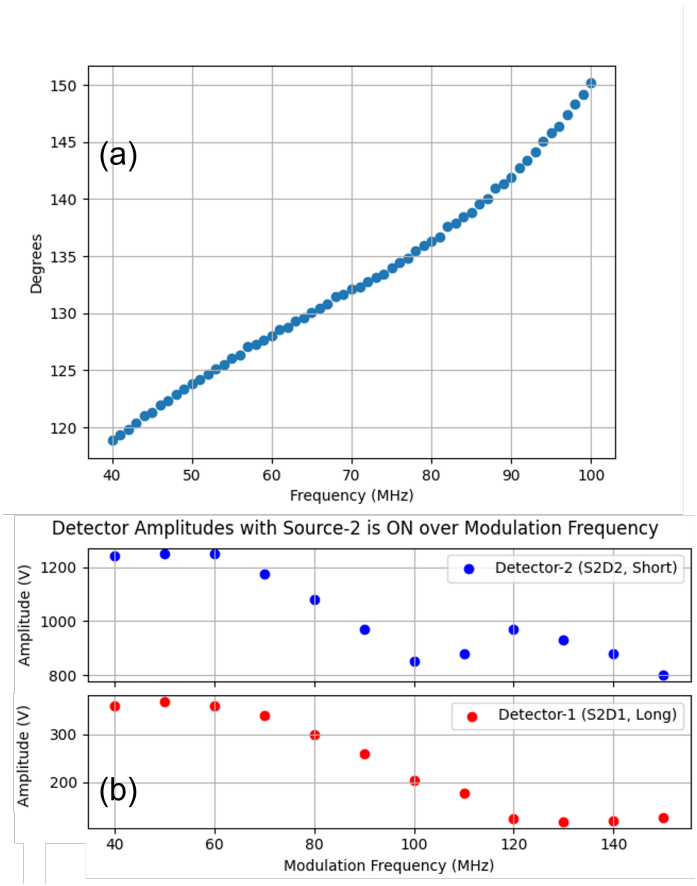

Figure -4: Panel (a) shows the measured IF phase versus modulation frequency for one channel, and Panel (b) shows the measured IF magnitudes versus frequency for both channels.

it is not sufficient because this noise of $\sim 1\,\mathrm{mV}_{rms}$ is also amplified by the Sallen-Key low-pass filters by 40 dB before being sampled by the oscilloscope. This TIA noise on top of the additional noise coupling from one channel to the other via the PCB resulted in very low signal-to-noise ratio and contaminated all measurements. However, this effort resulted in valuable knowledge and experience as to how to design the next generation of FD-NIRS ASIC.

Bibliography

[1] P. Taroni, A. Pifferi, A. Torricelli, D. Comelli, and R. Cubeddu, "In vivo absorption and scattering spectroscopy of biological tissues," *Photochemical & Photobiological Sciences*, vol. 2, no. 2, pp. 124–129, 2003.

[2] B. A. Crookes, S. M. Cohn, S. Bloch, J. Amortegui, R. Manning, P. Li, M. S. Proctor, A. Hallal, L. H. Blackbourne, R. Benjamin *et al.*, "Can near-infrared spectroscopy identify the severity of shock in trauma patients?" *Journal of Trauma and Acute Care Surgery*, vol. 58, no. 4, pp. 806–816, 2005.

[3] L. A. Schwarte, I. Schwartges, K. Thomas, P. Schober, and O. Picker, "The effects of levosimendan and glibenclamide on circulatory and metabolic variables in a canine model of acute hypoxia," *Intensive care medicine*, vol. 37, no. 4, pp. 701–710, 2011.

[4] A. Villringer, J. Planck, C. Hock, L. Schleinkofer, and U. Dirnagl, "Near infrared spectroscopy (NIRS): a new tool to study hemodynamic changes during activation of brain function in human adults," *Neuroscience letters*, vol. 154, no. 1-2, pp. 101–104, 1993.

[5] I. J. Bigio and S. Fantini, *Quantitative Biomedical Optics: Theory, methods, and applications*. Cambridge University Press, 2016.

[6] S. Nioka and B. Chance, "NIR spectroscopic detection of breast cancer," *Technology in cancer research & treatment*, vol. 4, no. 5, pp. 497–512, 2005.

[7] C. Hock, K. Villringer, F. Müller-Spahn, M. Hofmann, S. Schuh-Hofer, H. Heekeren, R. Wenzel, U. Dirnagl, and A. Villringer, "Near infrared spectroscopy in the diagnosis of Alzheimer's disease," *Annals of the New York Academy of Sciences*, vol. 777, no. 1, pp. 22–29, 1996.

[8] E. L. Heffer, *Frequency-domain optical mammography for detection and oximetry of breast tumors*. Tufts University, 2004.

[9] M. Kaiser, A. Yafi, M. Cinat, B. Choi, and A. J. Durkin, "Noninvasive assessment of burn wound severity using optical technology: a review of current and future modalities," *burns*, vol. 37, no. 3, pp. 377–386, 2011.

[10] M. Calderon-Arnulphi, A. Alaraj, S. Amin-Hanjani, W. W. Mantulin, C. M. Polzonetti, E. Gratton, and F. T. Charbel, "Detection of cerebral ischemia in neurovascular surgery using quantitative frequency-domain near-infrared spectroscopy," *Journal of neurosurgery*, vol. 106, no. 2, pp. 283–290, 2007.

[11] M. A. Khalil, H. K. Kim, I.-K. Kim, M. Flexman, R. Dayal, G. Shrikhande, and A. H. Hielscher, "Dynamic diffuse optical tomography imaging of peripheral arterial disease," *Biomedical optics express*, vol. 3, no. 9, pp. 2288–2298, 2012.

[12] A. Edwards, C. Richardson, M. Cope, J. Wyatt, D. Delpy, and E. Reynolds, "Cotside measurement of cerebral blood flow in ill newborn infants by near infrared spectroscopy," *The Lancet*, vol. 332, no. 8614, pp. 770–771, 1988.

[13] M. Dehaes, P. E. Grant, D. D. Sliva, N. Roche-Labarbe, R. Pienaar, D. A. Boas, M. A. Franceschini, and J. Selb, "Assessment of the frequency-domain multi-distance method to evaluate the brain optical properties: Monte Carlo simulations from neonate to adult," *Biomedical optics express*, vol. 2, no. 3, pp. 552–567, 2011.

[14] P.-Y. Lin, K. Hagan, A. Fenoglio, P. E. Grant, and M. A. Franceschini, "Reduced cerebral blood flow and oxygen metabolism in extremely preterm neonates with low-grade germinal matrix-intraventricular hemorrhage," *Scientific reports*, vol. 6, no. 1, p. 25903, 2016.

[15] A. Villringer and B. Chance, "Non-invasive optical spectroscopy and imaging of human brain function," *Trends in neurosciences*, vol. 20, no. 10, pp. 435–442, 1997.

[16] S. Fantini and A. Sassaroli, "Frequency-domain techniques for cerebral and functional near-infrared spectroscopy," *Frontiers in neuroscience*, vol. 14, p. 300, 2020.

[17] S. D. Power, A. Kushki, and T. Chau, "Automatic single-trial discrimination of mental arithmetic, mental singing and the no-control state from prefrontal activity: toward a three-state NIRS-BCI," *BMC research notes*, vol. 5, no. 1, p. 141, 2012.

[18] F. Scholkmann, S. Kleiser, A. J. Metz, R. Zimmermann, J. Mata Pavia, U. Wolf, and M. Wolf, "A review on continuous wave functional near-infrared spectroscopy and imaging instrumentation and methodology. NeuroImage, 85 (Part 1), 6–27," 2014.

[19] Y. Yamada, H. Suzuki, and Y. Yamashita, "Time-domain near-infrared spectroscopy and imaging: a review," *Applied Sciences*, vol. 9, no. 6, p. 1127, 2019.

[20] S. Fantini, M.-A. Franceschini, J. S. Maier, S. A. Walker, B. B. Barbieri, and E. Gratton, "Frequency-domain multichannel optical detector for noninvasive tissue spectroscopy and oximetry," *Optical engineering*, vol. 34, no. 1, pp. 32–42, 1995.

[21] S. A. Carp, P. Farzam, N. Redes, D. M. Hueber, and M. A. Franceschini, "Combined multi-distance frequency domain and diffuse correlation spectroscopy system with simultaneous data acquisition and real-time analysis," *Biomedical optics express*, vol. 8, no. 9, pp. 3993–4006, 2017.

[22] B. J. Tromberg, N. Shah, R. Lanning, A. Cerussi, J. Espinoza, T. Pham, L. Svaasand, and J. Butler, "Non-invasive in vivo characterization of breast tumors using photon migration spectroscopy," *Neoplasia*, vol. 2, no. 1-2, pp. 26–40, 2000.

[23] A. Orlova, I. Turchin, V. Plehanov, N. Shakhova, I. Fiks, M. Kleshnin, N. Y. Konuchenko, and V. Kamensky, "Frequency-domain diffuse optical tomography with single source-detector pair for breast cancer detection," *Laser Physics Letters*, vol. 5, no. 4, pp. 321–327, 2008.

[24] T. D. O'Sullivan, A. E. Cerussi, D. J. Cuccia, and B. J. Tromberg, "Diffuse optical imaging using spatially and temporally modulated light," *Journal of biomedical optics*, vol. 17, no. 7, pp. 071 311–071 311, 2012.

[25] T. H. Pham, O. Coquoz, J. B. Fishkin, E. Anderson, and B. J. Tromberg, "Broad bandwidth frequency domain instrument for quantitative tissue optical spectroscopy," *Review of scientific instruments*, vol. 71, no. 6, pp. 2500–2513, 2000.

[26] D. Roblyer, T. D O'Sullivan, R. V. Warren, and B. J. Tromberg, "Feasibility of direct digital sampling for diffuse optical frequency domain spectroscopy in tissue," *Measurement Science and Technology*, vol. 24, no. 4, p. 045501, 2013.

[27] A. Torjesen, R. Istfan, and D. Roblyer, "Ultrafast wavelength multiplexed broad bandwidth digital diffuse optical spectroscopy for in vivo extraction of tissue optical properties," *Journal of biomedical optics*, vol. 22, no. 3, pp. 036 009–036 009, 2017.

[28] B. B. Zimmermann, Q. Fang, D. A. Boas, and S. A. Carp, "Frequency domain near-infrared multiwavelength imager design using high-speed, direct analog-to-digital conversion," *Journal of biomedical optics*, vol. 21, no. 1, pp. 016 010–016 010, 2016.

[29] R. A. Stillwell, V. J. Kitsmiller, A. Y. Wei, A. Chong, L. Senn, and T. D. O'Sullivan, "A scalable, multi-wavelength, broad bandwidth frequency-domain near-infrared spectroscopy platform for real-time quantitative tissue optical imaging," *Biomedical optics express*, vol. 12, no. 11, pp. 7261–7279, 2021.

[30] G. Yu, T. Durduran, D. Furuya, J. H. Greenberg, and A. G. Yodh, "Frequency-domain multiplexing system for in vivo diffuse light measurements of rapid cerebral hemodynamics," *Applied optics*, vol. 42, no. 16, pp. 2931–2939, 2003.

[31] T. O. McBride, B. W. Pogue, S. Jiang, U. L. Österberg, and K. D. Paulsen, "A parallel-detection frequency-domain near-infrared tomography system for hemoglobin imaging of the breast in vivo," *Review of Scientific Instruments*, vol. 72, no. 3, pp. 1817–1824, 2001.

[32] Y. Yang, H. Liu, X. Li, and B. Chance, "Low-cost frequency-domain photon migration instrument for tissue spectroscopy, oximetry, and imaging," *Optical Engineering*, vol. 36, no. 5, pp. 1562–1569, 1997.

[33] Q. Zhang, T. J. Brukilacchio, A. Li, J. J. Stott, T. Chaves, E. Hillman, T. Wu, M. Chorlton, E. Rafferty, R. H. Moore *et al.*, "Coregistered tomographic x-ray and optical breast imaging: initial results," *Journal of biomedical optics*, vol. 10, no. 2, pp. 024 033–024 033, 2005.

[34] J. Culver, R. Choe, M. Holboke, L. Zubkov, T. Durduran, A. Slemp, V. Ntziachristos, B. Chance, and A. Yodh, "Three-dimensional diffuse optical tomography in the parallel plane transmission geometry: Evaluation of a hybrid frequency domain/continuous wave clinical system for breast imaging," *Medical physics*, vol. 30, no. 2, pp. 235–247, 2003.

[35] Y. Yu, N. Liu, A. Sassaroli, and S. Fantini, "Near-infrared spectral imaging of the female breast for quantitative oximetry in optical mammography," *Applied optics*, vol. 48, no. 10, pp. D225–D235, 2009.

[36] N. G. Chen, M. Huang, H. Xia, D. Piao, E. Cronin, and Q. Zhu, "Portable near-infrared diffusive light imager for breast cancer detection," *Journal of biomedical optics*, vol. 9, no. 3, pp. 504–510, 2004.

[37] K.-S. No, R. Kwong, P. H. Chou, and A. Cerussi, "Design and testing of a miniature broadband frequency domain photon migration instrument," *Journal of biomedical optics*, vol. 13, no. 5, pp. 050 509–050 509, 2008.

[38] B. W. Pogue, M. Testorf, T. McBride, U. Osterberg, and K. Paulsen, "Instrumentation and design of a frequency-domain diffuse optical tomography imager for breast cancer detection," *Optics express*, vol. 1, no. 13, pp. 391–403, 1997.

[39] J. R. Mackey, R. T. Powis, J. C. Walton, K. M. Hauser, C. S. Hall, D. J. Gotti, and A. R. Harrivel, "Frequency domain functional near-infrared spectrometer (fnirs) for crew state monitoring," NASA, Tech. Rep., 2020.

[40] J. J. Wathen, M. J. Fitch, V. R. Pagán, G. W. Milsap, E. G. McDowell, L. Spietz, Z. E. Markow, J. W. Trobaugh, E. J. Richter, A. T. Eggebrecht *et al.*, "A 32-channel frequency-domain fNIRS system based on silicon photomultiplier receivers," in *Optical Techniques in Neurosurgery, Neurophotonics, and Optogenetics*, vol. 11629. SPIE, 2021, pp. 62–79.

[41] M. C. Thompson, B. S. Robinson, G. W. Milsap, J. J. Wathen, M. J. Fitch, C. A. Scholl, and S. M. Hendrickson, "Phase component of frequency-domain functional

near-infrared imaging improves decoding of motor-evoked neural activity," in *2021 10th International IEEE/EMBS Conference on Neural Engineering (NER)*. IEEE, 2021, pp. 365–369.

[42] P.-T. Lee, H.-C. Chang, Y.-F. Hsu, H. Jiang, and M.-C. Pan, "Simultaneous multiple frequency and flexible optical channels based DOI system," in *Multimodal Biomedical Imaging XVII*, vol. 11952. SPIE, 2022, pp. 63–67.

[43] S. Yazdi, S. Mohammadi, S. Lahade, A. Beck, T. Quang, J. H. Lam, T. D. O'Sullivan, and M. M. Green, "Broad-bandwidth frequency-domain near-infrared spectroscopy system on a chip," in *Biophotonics in Exercise Science, Sports Medicine, Health Monitoring Technologies, and Wearables III*, vol. 11956. SPIE, 2022, pp. 8–17.

[44] S. Yazdi, S. Mohammadi, S. Lahade, T. Quang, J. H. Lam, T. D. O'Sullivan, and M. M. Green, "Broad-Bandwidth Frequency-Domain Near-Infrared Spectroscopy System on a Chip," *IEEE Sensors Journal*, 2025.

[45] B. J. Koh and H. M. Bae, "Multimodal portable functional brain imaging chip," *IDEC Journal of Integrated Circuits and Systems*, vol. 8, no. 4, pp. 49–56, 2022.

[46] C. Chen, Z. Ma, Y. Liu, Z. Liu, L. Zhou, Y. Wu, L. Qi, Y. Li, M. Sawan, G. Wang *et al.*, "A sub-0.01 phase resolution 6.8-mw fnirs readout circuit employing a mixer-first frequency-domain architecture," in *ESSCIRC 2022-IEEE 48th European Solid State Circuits Conference (ESSCIRC)*. IEEE, 2022, pp. 229–232.

[47] Y. Miao, "A Silicon Integrated fdNIRS System for Absolute Oximetry and Multi-modal Applications," Ph.D. dissertation, Tufts University, Medford, MA, February 2019.

[48] S. Fantini and A. Sassaroli, *Frequency-Domain Techniques for Tissue Spectroscopy and Imaging*. Bellingham, USA: SPIE, 2016, ch. 7, pp. 477–532.

[49] S. Jacques and P. Scott. (1998, March) Tabulated Molar Extinction Coefficient for Hemoglobin in Water. [Online]. Available: https://omlc.org/spectra/hemoglobin/summary.html

[50] S. Fantini, M. A. Franceschini, J. B. Fishkin, B. Barbieri, and E. Gratton, "Quantitative determination of the absorption spectra of chromophores in strongly scattering media: a light-emitting-diode based technique," *Applied optics*, vol. 33, no. 22, pp. 5204–5213, 1994.

[51] M. B. Applegate, C. A. Gómez, and D. Roblyer, "Modulation frequency selection and efficient look-up table inversion for frequency domain diffuse optical spectroscopy," *Journal of Biomedical Optics*, vol. 26, no. 3, pp. 036 007–036 007, 2021.

[52] D. M. Hueber, S. Fantini, A. E. Cerussi, and B. B. Barbieri, "New optical probe designs for absolute (self-calibrating) NIR tissue hemoglobin measurements," in *Optical tomography and spectroscopy of tissue III*, vol. 3597. SPIE, 1999, pp. 618–631.

[53] G. Blaney, A. Sassaroli, and S. Fantini, "Design of a source–detector array for dual-slope diffuse optical imaging," *Review of Scientific Instruments*, vol. 91, no. 9, 2020.

[54] S. Fantini, D. Hueber, M. A. Franceschini, E. Gratton, W. Rosenfeld, P. G. Stubblefield, D. Maulik, and M. R. Stankovic, "Non-invasive optical monitoring of the newborn piglet brain usingcontinuous-wave and frequency-domain spectroscopy," *Physics in Medicine & Biology*, vol. 44, no. 6, p. 1543, 1999.

[55] G. Blaney, R. Donaldson, S. Mushtak, H. Nguyen, L. Vignale, C. Fernandez, T. Pham, A. Sassaroli, and S. Fantini, "Dual-slope diffuse reflectance instrument for calibration-free broadband spectroscopy," *Applied Sciences*, vol. 11, no. 4, p. 1757, 2021.

[56] G. Blaney, A. Sassaroli, C. Fernandez, M. Bottoni, and S. Fantini, "Functional brain mapping with dual-slope frequency-domain near-infrared spectroscopy," in *Neural Imaging and Sensing 2022*, vol. 11946. SPIE, 2022, p. 1194602.

[57] G. Blaney, A. Sassaroli, and S. Fantini, "Spatial sensitivity to absorption changes for various near-infrared spectroscopy methods: A compendium review," *Journal of innovative optical health sciences*, vol. 17, no. 04, p. 2430001, 2024.

[58] G. Blaney, A. Sassaroli, T. Pham, C. Fernandez, and S. Fantini, "Phase dual-slopes in frequency-domain near-infrared spectroscopy for enhanced sensitivity to brain tissue: First applications to human subjects," *Journal of biophotonics*, vol. 13, no. 1, p. e201960018, 2020.

[59] A. Sassaroli, G. Blaney, and S. Fantini, "Dual-slope method for enhanced depth sensitivity in diffuse optical spectroscopy," *Journal of the Optical Society of America A*, vol. 36, no. 10, pp. 1743–1761, 2019.

[60] Y. Miao and V. J. Koomson, "A CMOS Integrated fdNIRS and tDCS System for Simultaneous Brain Stimulation and Monitoring," in *2017 IEEE 60th International Midwest Symposium on Circuits and Systems (MWSCAS)*. IEEE, 2017, pp. 499–502.

[61] Thorlabs. (2013, October) TTN006155-S01. Revision A. [Online]. Available: https://www.thorlabs.com/drawings/5d2e0138c3a826e6-0B04A295-AF69-A696-F432D452EB7B48C7/HL6750MG-SpecSheet.pdf

[62] ——. (2018, June) 21207-S01. Revision A. [Online]. Available: https://www.thorlabs.com/drawings/ffa53aa59d222f6f-A62B188A-E2CE-8AF6-FEE0E300DA5265EE/HL8338MG-SpecSheet.pdf

[63] Hamamatsu. (2017, March) S9251/S12092 series. [Online]. Available: https://www.hamamatsu.com/content/dam/hamamatsu-photonics/sites/documents/99_SALES_LIBRARY/ssd/s9251_etc_kapd1013e.pdf

[64] Matsusada Precision. (2024, November) TR Series. Revision 11. [Online]. Available: https://www.matsusada.com/product/high-voltage-modules/board-mount/tr/

[65] Texas Instruments. (2003, December) OPA695. Revision J. [Online]. Available: https://www.ti.com/lit/ds/symlink/opa695.pdf

[66] Infineon. (2018, September) BFP780. Revision 4.0. [Online]. Available: https://www.infineon.com/assets/row/public/documents/24/49/infineon-bfp780-ds-en.pdf?fileId=5546d46265f064ff01663896b2fe4eb3

[67] Analog Devices. (2020, January) ADG1411/ADG1412/ADG1413. Revision D. [Online]. Available: https://www.analog.com/media/en/technical-documentation/data-sheets/ADG1411_1412_1413.pdf

[68] ——. (2016, October) AD9959. Revision C. [Online]. Available: https://www.analog.com/media/en/technical-documentation/data-sheets/ad9959.pdf

[69] Minicircuits. ADTT1-1+. Revision F. [Online]. Available: https://www.minicircuits.com/pdfs/ADTT1-1+.pdf

[70] S. Fantini, M. A. Franceschini, and E. Gratton, "Semi-infinite-geometry boundary problem for light migration in highly scattering media: a frequency-domain study in the diffusion approximation," *Journal of the Optical Society of America B*, vol. 11, no. 10, pp. 2128–2138, 1994.

[71] K. S. No and P. H. Chou, "Mini-FDPM and heterodyne mini-FDPM: handheld non-invasive breast cancer detectors based on frequency-domain photon migration," *IEEE Transactions on Circuits and Systems I: Regular Papers*, vol. 52, no. 12, pp. 2672–2685, 2005.

[72] C. C. Sthalekar and V. J. Koomson, "A CMOS sensor for measurement of cerebral optical coefficients using non-invasive frequency domain near infrared spectroscopy," *IEEE Sensors Journal*, vol. 13, no. 9, pp. 3166–3174, 2013.

[73] T. Van Vo, P. E. Hammer, M. L. Hoimes, S. Nadgir, and S. Fantini, "Mathematical model for the hemodynamic response to venous occlusion measured with near-infrared spectroscopy in the human forearm," *IEEE transactions on biomedical engineering*, vol. 54, no. 4, pp. 573–584, 2007.

[74] Texas Instruments. (2015, August) How to Generate Current Sources and Sinks of Arbitrary Magnitude. [Online]. Available: https://www.ti.com/document-viewer/lit/html/SSZTCA8

[75] ——. (2022, August) ADS8685. Revision E. [Online]. Available: https://www.ti.com/lit/ds/symlink/ads8685.pdf?ts=1758454153419

[76] Analog Devices. (2016, December) AD630. Revision G. [Online]. Available: https://www.analog.com/media/en/technical-documentation/data-sheets/AD630.pdf

[77] R. A. De Blasi, M. Ferrari, A. Natali, G. Conti, A. Mega, and A. Gasparetto, "Noninvasive measurement of forearm blood flow and oxygen consumption by near-infrared spectroscopy," *Journal of Applied Physiology*, vol. 76, no. 3, pp. 1388–1393, 1994.

[78] G. Blaney, P. Curtsmith, A. Sassaroli, C. Fernandez, and S. Fantini, "Broadband absorption spectroscopy of heterogeneous biological tissue," *Applied optics*, vol. 60, no. 25, pp. 7552–7562, 2021.

[79] C. Fernandez, G. Blaney, J. Frias, F. Tavakoli, A. Sassaroli, and S. Fantini, "Single-distance and dual-slope frequency-domain near-infrared spectroscopy to assess skeletal muscle hemodynamics," *Journal of Biomedical Optics*, vol. 28, no. 12, pp. 125 004–125 004, 2023.

[80] L. Yang, H. Wabnitz, T. Gladytz, R. Macdonald, and D. Grosenick, "Spatially-enhanced time-domain NIRS for accurate determination of tissue optical properties," *Optics Express*, vol. 27, no. 19, pp. 26 415–26 431, 2019.

[81] J. R. Lakowicz and K. Berndt, "Frequency-domain measurements of photon migration in tissues," *Chemical physics letters*, vol. 166, no. 3, pp. 246–252, 1990.

[82] A. Romanova and V. Barzdenas, "Programmable-Gain Capacitive Feedback TIA for Low-Noise Applications in CMOS," in *2020 IEEE Open Conference of Electrical, Electronic and Information Sciences (eStream)*, 2020, pp. 1–6.

[83] Analog Devices. (2005, September) Integrated dc logarithmic amplifiers. [Online]. Available: https://www.analog.com/en/resources/technical-articles/integrated-dc-logarithmic-amplifiers.html

[84] C. C. Sthalekar, "Silicon Integrated Circuits and Systems for Frequency Domain Near Infrared Spectroscopy," Ph.D. dissertation, Tufts University, Medford, MA, March 2015.

[85] V. H. Bui, S. Beak, S. Choi, J. Seon, and T. T. Jeong, "Thermometer-to-binary encoder with bubble error correction (BEC) circuit for Flash Analog-to-Digital Converter (FADC)," in *International Conference on Communications and Electronics 2010*, 2010, pp. 102–106.

[86] S. Padoan, A. Boni, C. Morandi, and F. Venturi, "A novel coding scheme for the ROM of parallel ADCs, featuring reduced conversion noise in the case of single bubbles in the thermometer code," in *1998 IEEE International Conference on Electronics, Circuits and Systems. Surfing the Waves of Science and Technology (Cat. No.98EX196)*, vol. 2, 1998, pp. 271–274 vol.2.

[87] V. Hiremath and S. Ren, "A novel ultra high speed reconfigurable switching encoder for Flash ADC," in *Proceedings of the 2011 IEEE National Aerospace and Electronics Conference (NAECON)*, 2011, pp. 320–323.

[88] D. Lee, J. Yoo, K. Choi, and J. Ghaznavi, "Fat tree encoder design for ultra-high speed flash A/D converters," in *The 2002 45th Midwest Symposium on Circuits and Systems, 2002. MWSCAS-2002.*, vol. 2, 2002, pp. II–II.

[89] T. Pardhu, S. Manusha, and K. Sirisha, "A low power flash ADC with Wallace tree encoder," in *2014 Eleventh International Conference on Wireless and Optical Communications Networks (WOCN)*, 2014, pp. 1–4.

[90] M. Ajanya and G. T. Varghese, "Thermometer code to Binary code Converter for Flash ADC - A Review," in *2018 International Conference on Control, Power, Communication and Computing Technologies (ICCPCCT)*, 2018, pp. 502–505.

[91] Texas Instruments. (2019, May) Fundamentals to automotive led driver circuits. [Online]. Available: https://www.ti.com/lit/wp/slyy163/slyy163.pdf?ts=1754947744145

[92] Ushio. HL6750MG-A. [Online]. Available: https://www.ushio.co.jp/en/products/product_file/file/UIE_DS_HL6750MG.pdf